

ETH Zürich Series in Electromagnetic Fields, Vol. 33

Raphael Schwanninger

**Advancements in Mid-Infrared
Colloidal Quantum Dot Photodetectors:
Optimization, Metamaterials, and Fabrication**



Diss.-No.ETH 30625

ETH zürich

Diss. ETH NO. 30625

***ADVANCEMENTS IN MID-INFRARED COLLOIDAL
QUANTUM DOT PHOTODETECTORS: OPTIMIZATION,
METAMATERIALS, AND FABRICATION***

A thesis submitted to attain the degree of

DOCTOR OF SCIENCES

(Dr. sc. ETH Zurich)

presented by

RAPHAEL SEBASTIAN SCHWANNINGER

M. Sc. Electrical Engineering and Information Technology ETH Zurich

born on 13.01.1991

accepted on the recommendation of

Prof. Dr. Juerg Leuthold, examiner

Prof. Dr. Maksym Yarema, co-examiner

Dr. Ivan Shorubalko, co-examiner

2024

Acknowledgements

Pursuing a PhD and a career in research often involves frustration, setbacks, and long working hours, so why even consider it? This question was the topic of a conversation I had at the beginning of my PhD with my supervising **Prof. Dr. Juerg Leuthold**. "Look, we are not normal people," I was told, and to some extent, I have to agree. Embarking on such a journey takes determination, boundless curiosity, and stubbornness to keep moving forward. But that's not enough. Most importantly, it requires people who encourage you, help you, lend an ear, and support you. Without the people I encountered, I would never have overcome these hardships or experienced the joy of researching, creating, and understanding something unique and novel, which makes the encountered struggles pale in comparison. Thus, I want to thank the countless people who have helped me reach this achievement. You have my deepest and most sincere gratitude!

I want to thank **Prof. Dr. Juerg Leuthold**, for giving me the opportunity to pursue a PhD in the exceptional environment of the IEF. With his support, I was able to freely explore my research and ideas. I especially appreciate his availability whenever needed and his support, which allowed me to benefit from his extensive knowledge and experience, from selling one's work to conducting research. Due to his support and our discussions, I have significantly enhanced my research capabilities and overall skill set, for which I am very grateful.

Furthermore, I want to thank **Prof. Dr. Vanessa Wood**, who facilitated the collaboration between her research group, the Materials and Devices Engineering group (MaDe), and the IEF, making this thesis possible. I appreciate her support and valuable advice throughout the years and for providing access to her facilities. Most importantly, I am grateful for the great people I had the pleasure to get to know and work with due to this collaboration. One of them is **Prof. Dr. Maksym Yarema**. My first experience with cQDs during my Master thesis involved using materials he prepared and with his advice. Maksym always provided excellent advice and was incredibly supportive and helpful. I am grateful that he is now also part of the final steps at ETH as a co-examiner.

I want to extend a special thanks to **Dr. Olesya Yarema**, who always provided me with cQD materials whenever I needed them. Her skills, knowledge and advice were essential in achieving success in my research. Furthermore, I would like to thank **Jasper Clarysse**, **Dr. Annina Moser**,

Florian Schenk, Mario Mücklich and Dhananjeya Kumar for all the discussions, help, and joyful times in the cQD laboratory. It has been a pleasure!

Additionally, I would like to thank **Dr. Ivan Shorubalko** for being a co-referee for this dissertation, and for taking the time to review my work.

I would like to thank the IEF for the great time I had at the institute, excursions, events, and especially all the help I received. A special thanks goes to **Dr. Stefan Koepfli** for all the discussions and help, as well as for building the measurement setup, which greatly helped improve my research. Furthermore, I would like to thank all the “detector people”: **Shadi Nashashibi, Dominik Bisang, Michael Baumann, Dr. Michael Doderer, Daniel Rieben, Marina Homs, and Dr. Alexander Dorodnyy** for the valuable discussions and their continuous help. I also want to express my gratitude to everyone who helped and gave advice concerning fabrication, especially **Dr. Yuriy Fedoryshyn**. A special thanks also to my former and current office mates which have not yet been mentioned, **Elias Passerini, Raphael Gisler, Arnaud Schneuwly, Dr. Marco Eppenberger, Dr. Ian Bitachon, Stefano Valente, and Patrick Habegger**, for creating a relaxing and welcoming atmosphere. Additionally, I would like to thank all the other great people of the IEF **Dr. Alexander Lochbaum, Dr. David Moor, Yannik Horst, Dr. George Christidis, Dr. Arif Güngör, Dr. Mila Lewerenz, Dr. Andreas Messner, Dr. Bojun Cheng, Dr. Yannick Salamin, Dr. Joel Winiger, Dr. Ueli Koch, Dr. Daniel Chelladurai, Dr. Miklos Csontos, Dr. Yannik Horst, Tobias Blatter, Loic Cherix, Dober Marco, Filice Davide, Fischer Davide, Fischer Markus, Hande Ibili, Nadia Jimenez, Killian Keller, Manuel Kohli, Laurenz Kulmer, Kiran Menachery, Boris Vulkovic, Guillaume Zajac and Xinzhi Zhang**. Thanks for all the joyful encounters and support.

Finally, I would like to express my deepest gratitude to my **family, partner and friends**. My late **mother** instilled in me a lifelong curiosity and open-mindedness. My **father’s** support and encouragement to maintain perspective and reminders to keep things in balance and my **sister** for her unwavering moral support. I also want to thank my **friends** for always having my back and lending an ear to my complaints. Lastly, I want to thank my **partner** for her patience, encouragement, and all the wonderful distractions.

Table of Contents

Acknowledgements.....	Fehler! Textmarke nicht definiert.
Table of Contents.....	iii
Abstract.....	ix
Zusammenfassung	11
Achievements of this Work	13
1 Introduction.....	15
1.1 The Challenge: Cheap, Sensitive MIR Detection	18
1.2 The State-of-the-Art and Detector Technologies	20
1.2.1 Theoretical Detection Limitations	20
1.2.2 Colloidal Quantum Dots.....	21
1.2.3 2D Materials	22
1.2.4 Bulk Semiconductors	23
1.2.5 Multi Quantum Well Infrared Photodetection	24
1.2.6 Thermal and Schottky Barrier Detectors	24
1.3 The Vision	26
1.4 Organization of this Thesis.....	27
2 Fundamentals	29
2.1 Basic Semiconductor Physics for Photoconductors	30
2.1.1 Photoconductors	31
2.1.2 Photon Absorption in Semiconductors.....	35
2.1.3 Recombination.....	40
2.1.4 Noise.....	44
2.1.5 Figures of Merit & Metrics.....	48
2.1.6 Photoconductive Gain	49
2.2 Colloidal Quantum Dots.....	52
2.2.1 Introduction.....	52
2.2.2 cQD Synthesis	52
2.2.3 cQD Deposition and Ligand Exchange	54
2.2.4 Quantum Confinement and Optical Characteristics of cQDs.....	55
2.2.5 Charge Transport in cQD Assemblies.....	60
2.3 Optical Metamaterials	63
2.3.1 Basic EM Wave Propagation Theory.....	63
2.3.2 Metamaterials	64
3 Sintered PbSe/PbS Photodetector	69

3.1	Introduction	71
3.2	Device Structure and Fabrication	74
3.2.1	Optimizing the Deposition and Crystallization of cQD Lead Chalcogenide Absorber Layers	75
3.2.2	PbSe/PbS Heterojunction Photoconductors	78
3.2.3	Passive Characterization of PbSe/PbS Metamaterial Photodetectors	81
3.3	Results	84
3.4	Conclusion	88
3.5	Experimental Methods	89
3.5.1	cQD Synthesis	89
3.5.2	cQD Deposition and Annealing	89
3.5.3	XRD Characterization	89
3.5.4	UV-Vis Extinction Measurements	89
3.5.5	FTIR Characterization	90
3.5.6	Device Fabrication	90
3.5.7	E/O Characterization	90
3.5.8	Thickness Characterization of Annealed QD Layers	91
3.6	Supporting Information	92
3.6.1	cQD Synthesis	92
3.6.2	Time Dependent XRD Measurements	94
3.6.3	AFM Characterization	95
3.6.4	Optical Setup	95
3.6.5	Discussion on the Origin of the Photoconductivity in the Annealed PbSe cQD Layers	96
3.6.6	Discussion on the Presences of a Heterojunction	96
3.6.7	Time Dependent Photoresponse	98
3.6.8	Polarization Dependent Passive Absorption	99
3.6.9	Characterization Metamaterial Photodetectors	100
3.6.10	Comparison of Photodetectors	101
4	Metamaterial Optimization	105
4.1	Introduction	107
4.2	Results and Discussion	110
4.2.1	Device Architecture	110
4.2.2	Device Simulation	111
4.2.3	Passive Characterization	117
4.2.4	Metamaterial cQD Photodetector Performance Characterization	119
4.3	Conclusion	122
4.4	Experimental Section	124

4.4.1	Simulations	124
4.4.2	cQD Synthesis	124
4.4.3	Device Fabrication	124
4.4.4	Metamaterial and HgTe cQDs Absorption Measurements	124
4.4.5	O-E Characterization	125
4.4.6	XRD Characterization	125
4.5	Supporting Information	126
4.5.1	HgTe Colloidal Quantum Dots: Synthesis, Ligand Exchange and Material Characterization	126
4.5.2	Simulations	128
4.5.3	Characterization Setups	133
4.5.4	Photodetector Characterization	134
4.5.1	Power Distribution	137
4.5.2	Applicability to Other Wavelengths	138
4.5.3	HgTe Absorber Thickness	138
5	Summary & Outlook	139
	Appendix A Electronic Band Structure	141
	Appendix B Metal-Semiconductor Contacts	145
	Appendix C Semiconductor Heterojunction	149
	Appendix D Defect Centers in Semiconductors	151
	References	155
	List of Acronyms	191
	List of Symbols	195
	List of Supervised Theses	201
	List of Publications	203
	Curriculum Vitae	205

Abstract

Photodetectors operating in the mid-infrared spectral wavelength regime are crucial for numerous technologies and scientific advancements. They are integral to a wide array of applications, including biomedical imaging, environmental monitoring, thermal imaging, spectroscopy, and defense systems. However, developing photodetectors that are both highly sensitive and cost-effective remains a significant challenge. Therefore, this doctoral thesis explores the use of low-cost absorber materials in combination with performance enhancement schemes to overcome these limitations.

The cost-efficient material used in this thesis are colloidal quantum dots. These zero-dimensional nanometer-sized crystalline materials can be synthesized in solution and then deposited on various substrates using simple methods. Furthermore, their tunable absorption spectrum, achieved by altering their size, makes them ideal for a wide range of applications. This makes them an ideal candidate to reduce cost. However, photodetectors employing these materials often exhibit poor responsivities and detectivities. Thus, narrow-band resonant metamaterials were used to overcome these performance shortcomings. They were designed to increase the light absorption while simultaneously improving charge extraction properties and reducing noise.

The first photodetectors presented in this work were fabricated using lead selenide and lead sulfide colloidal quantum dots. A method was developed to sinter these quantum dots into a solid layer, resulting in improved charge transport properties and an extended absorption spectra to longer wavelengths. This sintered lead selenide layer was then covered by an additional, also sintered, lead sulfide layer to form a heterostructure. By stacking these layers, it was possible to enhance the photo-gain in the lead selenide layer and double the photoresponse. In the final step, this layer stack was combined with a metallic metamaterial perfect absorber. This enabled narrow-band tunable absorption enhancement with peak absorptivity's reaching 98%. As a result, the responsivity was increased up to twenty-fold, reaching 375 A/W and 4 A/W at wavelengths of 2710 nm and 4250 nm, respectively.

The second type of photodetector presented in this thesis utilizes mercury telluride colloidal quantum dots as an absorber layer. These colloidal quantum dots were also combined with metamaterials, which were

systematically improved using electro-optical simulations. This enabled the optimization of the metamaterial to increase the responsivity while simultaneously decreasing the noise spectral current density. Specifically, this was achieved by enhancing the photogenerated charge carrier collection efficiency and reducing the active material volume without compromising near-unity absorption.

The metamaterial optimization process started with a common disc resonator design. In a first step straight contacts were placed in between the disc resonators and then wrapped around them. Finally, the disc resonators and contacts were merged forming a narrow slot metamaterial. This design optimization process resulted in an approximate 13-fold increase in responsivity and a 345-fold increase in detectivity. The final metamaterial design achieves a responsivity of 16.2 A/W and a detectivity of 6×10^8 Jones at a wavelength of 2710 nm. This analysis provides a pathway to significantly improve the responsivity and noise characteristics of photodetectors based on cost-efficient cQDs.

Zusammenfassung

Photodetektoren, die im mittleren Infrarotspektralbereich arbeiten, sind von großer Bedeutung für zahlreiche technologische und wissenschaftliche Fortschritte. Sie sind unverzichtbar für ein breites Spektrum an Anwendungen, darunter biomedizinische Bildgebung, Umweltüberwachung, Wärmebildgebung, Spektroskopie und Verteidigungssysteme. Die Entwicklung von kostengünstigen und sensitiven Photodetektoren in diesem Spektrum stellt eine erhebliche Herausforderung dar. Daher untersucht diese Doktorarbeit die Verwendung von kostengünstigen Absorbermaterialien in Kombination mit Leistungsverbesserndenmassnahmen, um diese Einschränkungen zu überwinden.

Das Kosten sparende Material, das hier verwendet wird, sind kolloidale Quantenpunkte. Diese null-dimensionalen, nanometergroßen kristallinen Materialien können in Grosser Anzahl in Lösung synthetisiert und dann mit einfachen Methoden auf verschiedene Substrate aufgetragen werden. Darüber hinaus macht ihr anpassbares Absorptionsspektrum, das durch Ändern ihrer Größe erreicht wird, sie ideal für eine Vielzahl von Anwendungen. Dies macht sie zu einem idealen Kandidaten zur Kostenreduktion. Photodetektoren, die diese Materialien verwenden, weisen jedoch oft eine niedrige Licht Sensitivität auf. Um diese Defizite zu überwinden, wurden Metamaterialien verwendet. Sie wurden so konzipiert, dass sie die Lichtabsorption erhöhen und gleichzeitig die Ladungsträgerextraktion verbessern und das elektrische Rauschen reduzieren.

Die ersten in dieser Arbeit vorgestellten Photodetektoren wurden mit Bleiselenid und Bleisulfid kolloidalen Quantenpunkten fabriziert. Es wurde eine Methode entwickelt, um diese Quantenpunkten zu einer soliden Schicht zu sintern. Dadurch konnten die Ladungstransporteigenschaften verbessert werden und das Absorptionsspektrum auf längere Wellenlängen erweitert werden. Die gesinterte Bleiselenid Schicht wurde dann mit einer zusätzlichen, ebenfalls gesinterten, Bleisulfid- Schicht zu einer Heterostruktur kombiniert. Durch das Stapeln dieser Schichten war es möglich, den Foto Multiplikationsfaktor zu erhöhen und die Lichtempfindlichkeit zu verdoppeln. Im letzten Schritt wurde die Schichtkonfiguration mit einem metallischen Metamaterial kombiniert. Dies ermöglichte die schmalbandige Lichtabsorption zu erhöhen und spektral zu

1 Introduction

variieren. Dadurch wurde die Lichtempfindlichkeit um das Zwanzigfache erhöht und erreichte 375 A/W und 4 A/W bei Wellenlängen von 2710 nm bzw. 4250 nm.

Der zweite Typ von Photodetektoren, der in dieser Arbeit vorgestellt wird, wurde mit kolloidale Quantenpunkte aus Quecksilbertellurid als Absorptionsmaterial realisiert. Weiters wurden diese kolloidalen Quantenpunkte ebenfalls mit Metamaterialien kombiniert, welche systematisch durch elektro-optische Simulationen verbessert wurden. Dies ermöglichte die Optimierung des Metamaterials, um die Empfindlichkeit zu erhöhen und gleichzeitig das elektrische Rauschen zu verringern. Dies wurde erreicht durch die Verbesserung der fotogenerierten Ladungsträger Sammeleffizienz und die Reduzierung des Volumens des licht absorbierenden Materials erreicht, ohne die licht Absorption zu beeinträchtigen.

Der Metamaterial Optimierung Prozess begann mit einer häufig verwendeten und bekannten Architektur, die auf Scheibenresonatoren basiert. In dem ersten Schritt wurden gerade Kontakte zwischen den Scheibenresonatoren platziert und anschließend um sie herumgeführt. Schließlich wurden die Scheibenresonatoren und Kontakte zu einem Metamaterial verschmolzen, das nur aus Kontakten mit schmalen spalten besteht. Dieser Designoptimierungsprozess führte zu einer ungefähren 13-fachen Steigerung der Empfindlichkeit und einer 345-fachen Erhöhung der Detektivität. Das finale Metamaterial-Design erreichte eine Empfindlichkeit von 16.2 A/W und eine Detektivität von 6×10^8 Jones bei einer Wellenlänge von 2710 nm. Dieser Analyse und Optimierungsprozess beschreibt einen Weg, um die Empfindlichkeit und die Rauscheigenschaften von Fotodetektoren, die auf kosteneffizienten kolloidalen Quantenpunkten basieren, erheblich zu verbessern.

Achievements of this Work

In this thesis, colloidal quantum dots were processed and combined with plasmonic metamaterials, effectively overcoming material shortcomings and enabling cost-efficient and sensitive photodetection in the mid-infrared spectral wavelength range. In summary, the following main achievements have been made:

Sintering and Stacking of Colloidal Quantum Dots

A method was developed enabling the sintering of solution-deposited colloidal quantum dots into solid polycrystalline layers. This method involved a chemical treatment and low temperature annealing to remove contaminants and solvent residue followed by high-temperature annealing inducing sintering. As a result of this treatment, the quantum confinement was lost, enabling mid-infrared photoconductivity, improved carrier transport, and large gain. Additionally, this approach allowed for the stacking of two dissimilar materials to form a heterostructure doubling the photoresponse.

Demonstration of Metamaterial Enhanced Sintered PbSe/PbS Heterostructure Photodetector

The sintered colloidal quantum dot layers were integrated with a narrow-band resonant plasmonic perfect absorber metamaterial to create a highly responsive mid-infrared photodetector. This combination enabled near-unity absorption, which could be tuned over a wide spectral range. The integration of the metamaterial with the sintered colloidal quantum dot heterostructure significantly enhanced the device's performance, resulting in up to a 20-fold increase in responsivity. Specifically, the photodetector achieved responsivity values of 375 A/W at a wavelength of 2710 nm and 4 A/W at 4250 nm.

Electro-Optical Simulation-Based Optimization of Metamaterials

Electrical and optical simulations of metamaterials were employed to identify novel designs enhancing the performance of metamaterial enhanced mercury telluride quantum dot photodetectors. These simulations focused on improving the photogenerated carrier collection efficiency by reducing the carrier transition time and optimizing the overlap of the externally applied electric field with regions of strongest

1 Introduction

absorption within the colloidal quantum dot layer. Additionally, the active volume of the photo active material was reduced leading to a decrease of the noise current spectral density while maintaining near-unity absorption. The designs also offered absorption tunability over a wide spectral range, ensuring versatile application capabilities.

Demonstration and Verification of Metamaterial Design Optimization Schemes

The simulated and optimized metamaterial designs were fabricated and characterized, validating the effectiveness of the optimization strategies. By implementing these improvements, the responsivity at a wavelength of 2710 nm was increased 13-fold with a final value of 16 A/W. Additionally, due to a reduction in noise, the detectivity was improved by a factor of 345 reaching 6×10^8 Jones. These optimization strategies are versatile and can be adapted for various photodetector materials operating across different wavelength regimes. This result highlights the broad applicability and relevance of the strategies for designing metamaterial-enhanced photodetectors, ensuring their effectiveness for a wide range of applications in different spectral regions.

1 Introduction

In 1800, an experiment performed by William Herschel revealed that the sun's spectrum extends beyond visible light.[1, 2] He further discovered that the spectral wavelengths beyond visible red contain a significant amount of the sun's total energy, even exceeding the total energy contained in the visible spectrum. While the existence of infrared radiation was discovered in 1800, it wasn't until 1917 that photoconductors were identified, which allowed for the conversion of this energy into an electrical signal.[3] In the following decades, mainly driven by military interests, infrared photodetector technology experienced significant advancements, leading to the production of the first lead salt (PbS, PbSe), indium antimonide (InSb), and mercury cadmium telluride ($\text{Hg}_{1-x}\text{Cd}_x\text{Te}$)[4] photodetectors which are to date still often used materials to realize photodetectors.[2, 5]

Over time, the infrared spectrum has been divided into subcategories based on the wavelength which corresponds to the photon energy. This aids in classifying devices operating in the infrared spectral range. The spectra are usually split into the near infrared (NIR, 0.75-1.4 μm , 1.65-0.89 eV), the short-wave infrared (SWIR, 1.4-2.5 μm , 0.89-0.5 eV), the mid-infrared (MIR, 2.5-8 μm , 0.5-0.155 eV), and the long wave infrared (LWIR, 8-15 μm , 0.155-0.083 eV) spectral range. It should be noted that the wavelength ranges of these subcategories are not fixed and can vary depending on the source.

The initial military-driven development of infrared photodetectors paved the way for new applications and research topics, increasing the demand for more sensitive and cost-effective detectors. The MIR spectral range, for example, is especially relevant for the fields of astronomy[6, 7], spectroscopy[8, 9], biomedical applications[10] and bioimaging[11–13], thermal imaging[14, 15] and more. Although there are many uses for this spectral range there are limiting factors for devices such as photodetectors. Materials enabling the detection in this spectral range area scarce which lead to research of new devices concepts and material classes such as multi quantum well infrared detectors (MQWIPs)[16–18] and zero, one and two dimensional (0D, 1D, and 2D) materials[19]. Especially the low dimensional materials have shown extraordinary properties and have raised significant interest for infrared detection capabilities.[20]

Colloidal quantum dots (cQDs) are 0D materials holding great promise for photodetection in the MIR spectral range due to their unique size-tunable optoelectronic properties and large absorption coefficients.[21, 22]

1 Introduction

By precisely controlling their size, it is possible to tune their absorption and emission characteristics, enabling the development of highly selective MIR detectors.[23–25] In Figure 1.1 the spectral emission range of several cQD materials is shown.

cQDs not only provide tunability in absorption and emission properties but also offer significant advantages over traditional bulk materials. Their low-cost, solution-based fabrication allows for large-area, substrate independent deposition, while their high absorption coefficients translate to efficient absorption of MIR light.[26] However, challenges remain. The charge carrier mobility is often much lower than bulk semiconductors, limiting device performance due ineffective carrier extraction. Additionally, surface traps and environmental instability can affect their long-term operation and increase noise and carrier recombination. [27–29]

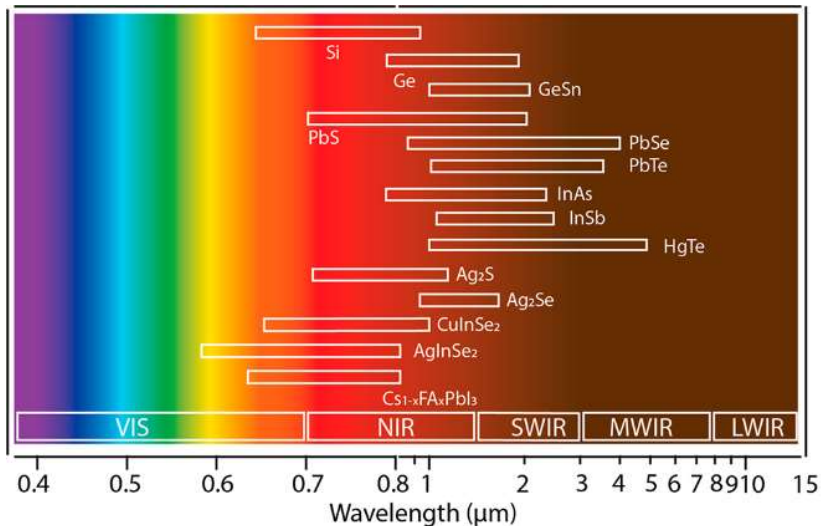


Figure 1.1. Spectral emission wavelength range for cQDs relevant to the infrared spectrum. Reprinted with permission from [28]. Copyright 2019 American Chemical Society.

To address the performance limitations of cQD based photodetectors, various strategies can be employed. One effective approach is integrating cQDs with metamaterials. This combination enhances light absorption by leveraging metamaterial resonances, which can significantly improve the absorption and as a result the photoresponse.[30–34] Additionally, creating heterostructures and utilizing transport layers materials can promote carrier

separation, increase gain, and reduce recombination, further boosting device performance. [35–40]Optimizing the charge carrier collection efficiency is also crucial, this can be achieved by designing devices with short carrier travel paths and efficient charge extraction methods or improving the transport properties in the cQD layers.[41–44] These strategies can maximize responsivity, minimize noise, and enhance the overall performance of cQD-based MIR photodetectors as presented in this dissertation. Furthermore, the strategies presented hold great promise for future devices, potentially rivaling the state of the art.

1 Introduction

1.1 The Challenge: Cheap, Sensitive MIR Detection

The demand for cost-effective and sensitive MIR photodetectors operating at room temperature is increasing.[45–47] High sensitivities are especially relevant for detectors employed in fields such as astronomy and material characterization, where it is often necessary to detect extremely faint signals.[6, 7]

Despite the ongoing research efforts to attain highly sensitive and low cost detector, achieving these requirements remains elusive. This can be partially attributed to the limited number of low band gap materials suitable for fabricating detectors that operate in the MIR wavelength regime. Additionally, the fabrication of sensitive detectors often necessitates high crystallinity of these materials, which can significantly complicate the deposition process. As a result, advanced and expensive equipment is usually required, often limiting production throughput. Furthermore, these materials often cannot be grown on all substrates. This substrate dependence can result in challenging bonding processes where the active material is bonded onto a different substrate. [46, 48, 49]

cQDs emerge as a promising candidate to overcome the limitations of current technologies in infrared detection. Although they show great potential in this area, further improvements of these materials are necessary.[27–29] The ability of cQDs to address the challenges of MIR detection is underscored by significant research efforts dedicated to enhancing their capabilities. This high demand, coupled with their considerable potential, has spurred ongoing research in this field, which is evidenced by the increasing volume of research output in recent years, as is shown in Figure 1.2. [21]

In summary, advancements in developing affordable and high-performance MIR detectors using inexpensive absorber materials will be essential in unlocking the full potential of this technology. Such breakthroughs will enable more innovation in diverse applications, ranging from astronomy and material characterization to medical diagnostics and industrial process control.

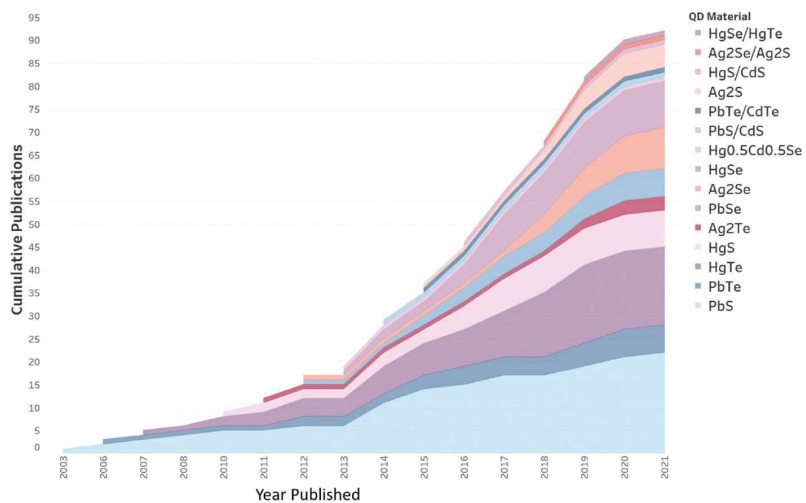


Figure 1.2. Number of published research articles focused on the topic of IR-detection utilizing cQDs vs the year of publishing. The different colors correspond to different cQD materials. Reprinted with permission from [21]. Copyright 2022 The Royal Society of Chemistry.

1 Introduction

1.2 The State-of-the-Art and Detector Technologies

In this section, an overview of the current state of the art is provided. The section will be divided into the following sections, cQDs, 2D materials, bulk materials, MQW-based detectors, and finally thermal and Schottky barrier detectors. Additionally, before discussing the state of the art, the fundamental detection limit of photodetectors is introduced and an overview of existing commercial detector performance is given as a baseline.

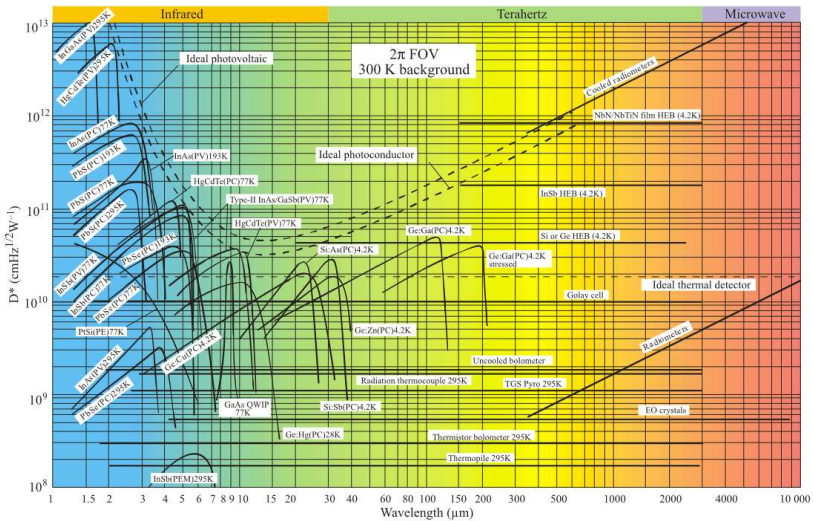


Figure 1.3. Comparison of the wavelength dependent detectivity D^* of different types of photodetectors made from various materials. Theoretical curves for the background-limited detectivity (dashed lines) are shown for ideal photovoltaic and photoconductive detectors, as well as thermal detectors. The used abbreviations include: PC (photoconductive detector), PV (photovoltaic detector), PEM (photoelectromagnetic detector), and HEB (hot electron bolometer). Reprinted with permission from [2].

1.2.1 Theoretical Detection Limitations

Theoretically, there is a fundamental limit of charge carrier-based detection, which is determined by the background radiation, referred to as the background-limited infrared photodetection (BLIP). [2, 50, 51] This limit arises from the shot noise resulting from the photocurrent generated by the background radiation. This background radiation is emitted by all objects at

a given temperature. Consequently, the sensitivity of infrared detectors is ultimately constrained by this inherent background noise. Similarly, there is a detection limit for thermal detectors resulting from this background radiation.[52]

In Figure 1.3 the mentioned detection limits and the detectivity of selected commercial detectors made from various materials are shown. It can be seen that the detectivity limit of carrier-based detectors is higher than that of thermal detectors, making the former relevant for highly sensitive applications. Moreover, various detector technologies are already approaching the detection limit, raising the question about the necessity of further research in this area. Although these detection limits have nearly been reached, the detectors achieving them require cooling and are costly. Therefore, the main objective is to achieve detectivities close to the BLIP while being cost-effective and capable of operating at room temperature.

1.2.2 Colloidal Quantum Dots

cQDs are, as already discussed, excellent candidates for photodetector applications in the MIR spectral range. This is also evident by viewing the increase of research output focusing on this topic over the last years, see Figure 1.2. In this section, the progress and state of the art of detectors based on these the cQD materials are discussed.

One of the first cQD materials employed for detection in the SWIR and MIR ranges were PbS and PbSe. This can be attributed to their stability and matured synthesis recipes.[53, 54] With these materials it was possible to demonstrate high responsivities in the MIR spectrum, achieving values of 11 A/W and 8 A/W at wavelengths of 3.5 and 4 μ m.[55, 56] Such large responsivities or even greater are often observed for these materials and mostly attributed to gain resulting from carrier trapping.[57, 58] Although this effect can lead to large responsivities it also increases noise, which limits the detectivity. Recent efforts to passivate lead-based cQDs during synthesis, utilizing iodide, have shown promise for improvements regarding device performance.[59] Nevertheless, due to the limited absorption spectra of these dots, which extend up to only 4 μ m, their use is restricted in various applications.

A different cQD material system used for MIR photodetection are mercury chalcogenides, especially HgTe and HgSe. Among this material system HgTe is the most widely used and established.[60–62] Initially, devices using HgTe performed poorly and required cooling to achieve

1 Introduction

detectivities of $\sim 1 \times 10^9$ Jones at 100K. Uncooled devices reached only values of approximately 3×10^7 Jones, at a wavelength of 5 μm , making them initially irrelevant for detection applications.[63]

Advancements in device performance have been driven by several material improvements leading to improved device performances. Refined synthesis methods have yielded better control over particle size, while ligand exchange techniques have enabled higher carrier mobilities and controlled doping.[40, 64–68] Advanced ligand exchange methods have even lead state resolved band like transport.[69–72] Furthermore, controlling the doping of cQDs has proven especially crucial in enhancing device performance, since it allows for the fabrication of p-n junctions. These improvements have led to a demonstration of a homojunction photodetector that achieved a detectivity of 7.6×10^9 Jones at room temperature and 2.7×10^{11} Jones at 80K, at a wavelength of 4.4 μm . [73] These improvements indicate a promising trend for future detectors.

Material advancements are not the only factors contributing to improved device performance of cQD based photodetectors. Various methods have been explored to enhance the performance, with two particularly promising approaches. The first involves integrating plasmonic metasurfaces with cQDs as a versatile and tunable method that significantly enhances absorption.[74–80] The second approach combines cQDs with 2D materials used as charge extraction layers. This introduction of a transport layer can help to extract photogenerated carriers more efficiently, leading to substantial increases in responsivity, with figures reaching hundreds of A/W.[81–85]

Although, cQDs hold great potential for MIR detection, they also face limitations. The primary challenges include their charge carrier transport properties and electronic noise. While recent works have made great progress, this remains an ongoing area of research. [40, 64–67, 86, 87]

1.2.3 2D Materials

While cQDs have shown great promise for detection in the MIR spectrum, there is also various research focusing on 2D materials.[88] Graphene, the most prominent among these, is extensively studied alongside others like transition metal dichalcogenides (TMDCs) and black phosphorus (bP). The key advantages of 2D materials for photodetectors include high carrier mobility resulting in efficient photocurrent generation. Additionally, materials like graphene and bP, which have no or narrow band

gaps, can absorb light across a broad wavelength range, including the MIR spectrum.[89]

Their suitability for MIR photodetection has been demonstrated in recent years with detectivities rivaling, and in some cases surpassing, well-established technologies.[81, 90–94] Although numerous reports highlight exceptionally good performance, these claims must be critically evaluated. Concerns have been raised regarding the potential overestimation of these performance metrics.[50, 95, 96]

Despite their potential, 2D materials face challenges that limit their widespread utilization. Large-scale deposition remains challenging, hindering their integration into industrial processes. Additionally, their atomic thinness inherently limits light absorption. This necessitates the use of absorption enhancement strategies such as metasurfaces. However, even with these enhancements, their limited thickness can lead to rapid absorption saturation. Nevertheless, 2D materials hold great promise for future applications once these obstacles are overcome.[39, 47, 89, 97–99]

1.2.4 Bulk Semiconductors

Bulk semiconductors represent the oldest and most widely used material class for MIR photodetectors. They continue to dominate the market due to their proven performance and reliability. Commercial detectors based on these materials can achieve detectivities near the BLIP limit. However, they also show significant limitations, most notably their high cost and the requirement for cooling, which increases both complexity and cost.[2, 100] In the following paragraphs the two most used material systems will be shortly discussed.

Lead chalcogenides, PbS and PbSe, are favored for MIR detection due to their high detectivity up to wavelengths of $\sim 4 \mu\text{m}$ for PbSe and $\sim 3 \mu\text{m}$ for PbS, combined with cost efficiency. [19, 101] However, their photoresponse is poor unless they undergo sensitization, thermal treatment in an oxygen and iodine atmosphere, which leads to high resistance sheet necessitating large driving voltages. [57, 102, 103] Furthermore, achieving uniform, highly sensitive thin layers remains a challenge.

Mercury cadmium telluride (MCT), known for its exceptional performance across a wavelength range of $\sim 2.5\text{-}12 \mu\text{m}$, allows spectral tuning of absorption by adjusting the mercury to cadmium ratio. Commercial detectors have been reported to reach detectivities of 4×10^{10} and 2×10^9 Jones for cooled and uncooled operation at a wavelength of $5 \mu\text{m}$,

1 Introduction

respectively.[95] Nonetheless, MCT fabrication is complex and costly, requiring sophisticated equipment, and the detectors often need cooling, adding to the costs and complexity.[104]

Similarly, InSb is a well-established material for infrared detection with a narrower absorption range up to 6 μm . Its fabrication is expensive, involves complex equipment, and its performance is highly temperature-dependent, restricting its broader application.[105]

1.2.5 Multi Quantum Well Infrared Photodetection

MQWIP is another technology employed to achieve MIR photodetection, resulting in high detectivities. These detector structures consist of alternating layers of materials with different band gap widths, creating quantum wells with distinct energy levels. This configuration allows for the tuning of absorption properties based on the stoichiometry and thickness of the layers used. In recent years type-II superlattice devices have reached detectivities in the range of 1×10^9 Jones at room temperature, comparable to MCT detectors.[106, 107]

The fabrication of such layer stacks requires precision and stringent control over the deposition process, which is typically accomplished through molecular beam epitaxy (MBE). This method renders the fabrication of these detectors expensive. Additionally, to prevent strain, the materials used must have compatible lattice constants, limiting the choice of suitable materials. As a result, these demanding requirements significantly restrict the widespread adoption of MQWIPs.[108, 109]

1.2.6 Thermal and Schottky Barrier Detectors

Thermal detectors sense light through light-induced temperature changes. The temperature change can cause various effects, such as resistance changes in bolometers or charge separation in pyroelectric detectors. A significant advantage of these detectors is their ability to detect light up to the submillimeter wavelength regime (terahertz radiation). However, their major drawback is their fundamentally limited detectivity, which is below that of photonic detectors, see Figure 1.3. [2, 110–112]

Finally, Schottky barrier detectors, also referred to as hot carrier photodetectors, are discussed. They are a type of photodetector that utilizes a metal-semiconductor Schottky type junction to convert light into electrical current. When light strikes the device, it can excite electrons in the metal creating hot carriers. If the energy of the carriers is sufficiently large, they

can overcome the barrier formed between the metal and semiconductor and generate current. The advantage of these detectors lies in their simple fabrication and tunable absorption spectra, as the barrier height can be adjusted by applying a voltage. However, they have a significant drawback: these devices exhibit very low photoresponse and are severely limited in their detectivity, making them less suitable for many applications.[113, 114]

1 Introduction

1.3 The Vision

cQDs hold significant promise across various fields, including pharmaceuticals[115, 116] and biomedicine[10, 13], catalysis[117–120], optoelectronics[121, 122] the focus of this work. By developing innovative methods for processing and integrating cQDs with metamaterials, this research aims to overcome existing photodetection limitations and enable the fabrication of cost-efficient, highly sensitive, and room-temperature-operable MIR photodetectors.

Furthermore, it is envisioned that the processing and enhancement strategies presented are applied to other devices, advancing the use of cQDs and opening new possibilities across diverse fields, ultimately driving technological innovation and benefiting scientific and commercial applications.

1.4 Organization of this Thesis

The thesis is structured in the following way to guide the reader through the topic of MIR photodetection enabled by cQDs and metamaterials:

- Chapter 1, provides an introduction to the thesis topic and outlines its significance. It reviews the current state-of-the-art materials and technologies for MIR photodetectors.
- Chapter 2, introduces the reader to the fundamental physics, key concepts, and relevant metrics essential for understanding the topics and observed effects discussed in later chapters.
- Chapter 3, details the work on sintering colloidal quantum dots to form polycrystalline layers, which were combined into heterostructure photoconductor devices. Furthermore, it explains the processes and techniques used to combine these heterostructures with a metamaterial perfect absorber.
- Chapter 4, explains how photodetection improvement strategies were employed through simulations to identify optimized device designs. These designs were subsequently fabricated and experimentally verified.
- Chapter 5 summarizes the key findings and discussions presented throughout the thesis. Finally, it offers an outlook for future research and potential endeavors.

1 Introduction

2 Fundamentals

This section provides an introduction to semiconductor physics and key concepts fundamental to understanding photodetectors. It begins with an overview of the principles governing photodetector behavior, including photoconductivity and the relevant figures of merit. Next, the section introduces colloidal quantum dots, explaining their unique attributes and relevance to the field of photodetection. Finally, an introduction to metamaterials is presented, offering a foundational understanding necessary for the subsequent work discussed in the dissertation.

2 Fundamentals

2.1 Basic Semiconductor Physics for Photoconductors

The capacity to absorb light and convert it into a measurable signal has been of immense interest across a variety of disciplines. A device that facilitates the conversion of light into a measurable quantity is the photodetector. Light can be transformed into various measurable quantities, with one of the most important being the conversion into an electrical signal.

This conversion is typically achieved through the utilization of photoactive materials, wherein incident photons can create electron-hole pairs, resulting in a measurable electrical quantity. Several architectures are available for designing photodetectors. One of the simplest designs is illustrated in Figure 2.1, which shows a photodetector consisting of contacts connected to a light-absorbing photoconductor.

The subsequent chapters will focus on this type of detector. Initially, an introduction to the physics of photoconduction will be provided. This will be followed by an analysis of photon induced carrier generation. The discussion will then extend to recombination mechanisms of photogenerated carriers. Lastly, the issue of noise in signal detection will be addressed, and figures of merit will be introduced to facilitate the comparison of different photodetectors, including a discussion on gain mechanism.

In addition to this discussion, readers will find an introduction to electronic band structures (Appendix A), metal-semiconductor interfaces (Appendix B), semiconductor-semiconductor interfaces (Appendix C), and defect states (Appendix D) in the appendix.

The theory presented in this section and the appendix is described using standard nomenclature and commonly accepted definitions. It closely adheres to the definitions and theoretical frameworks established in literature[123–128].

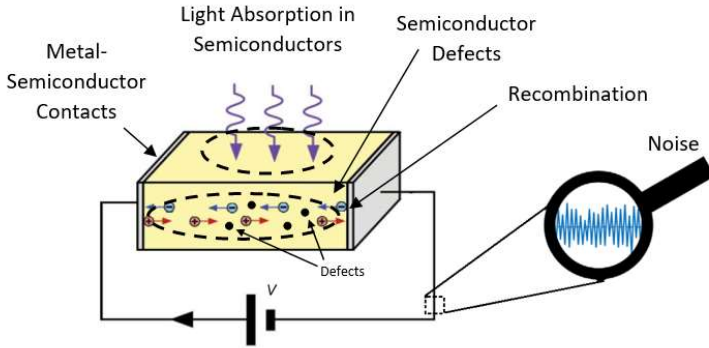


Figure 2.1 Depiction of a photodetector featuring metal contacts and an external voltage source. The illustration highlights light absorption, photogenerated carriers, and defect centers. Additionally, it includes an indication of noise affecting the external signal. Reprinted with permission from [123]. Copyright 2022 John Wiley & Sons Ltd.

2.1.1 Photoconductors

Photodetectors utilizing the photoconductive effect are highly favored, primarily due to their inherent simplicity and cost-effectiveness. The photoconductive effect describes the property of a material to change its conductivity upon illumination. This effect can be classified into intrinsic and extrinsic photoconductivity. The distinction between these two mechanisms arises from the type of transitions of the charge carriers resulting from optical excitations. In case of intrinsic photoconductivity, carriers are excited from the valence to the conduction band, while extrinsic photoconductivity involves transitions including energy states located within the band gap. In this work, the primary emphasis will be on intrinsic photoconductivity, which will be simply referred to as photoconductivity unless stated otherwise.

When photons with energies greater than the band gap energy E_G of the photoconductive material are absorbed, they generate electron-hole pairs. These additional electron (Δn) and hole (Δp) densities upon illumination result in an overall increased electron and hole carrier density n_{ph} and p_{ph} compared to the electron and hole densities in dark n_d and p_d , expressed as

$$n_{ph} = n_d + \Delta n \quad (2.1)$$

2 Fundamentals

and

$$p_{ph} = p_d + \Delta p \quad (2.2)$$

The change in carrier density ultimately leads to a change of the conductivity. The conductivity σ can therefore be expressed as the sum of the conductivity in the dark σ_d and the change induced by illumination $\Delta\sigma_{ph}$

$$\begin{aligned} \sigma_{ph} &= \sigma_d + \Delta\sigma_{ph} \\ &= e(\mu_n n_d + \mu_p p_d) + e(\mu_n \Delta n + \mu_p \Delta p) \end{aligned} \quad (2.3)$$

This change in local conductivity can ultimately result in a change in the externally measured current (photocurrent) when a constant electric bias is applied to the material.

The additional carrier densities Δp and Δn can be further expressed as a time dependent change which is the difference of the optical induced carrier generation rate and the recombination rate and is expressed as

$$\frac{d \Delta n}{dt} = g_n - r_n \quad (2.4)$$

and

$$\frac{d \Delta p}{dt} = g_p - r_p \quad (2.5)$$

In the case of intrinsic photoconductivity, it is anticipated that the photon induced rates of electron g_n and hole g_p generation are equal. Furthermore, the recombination rates r_n and r_p are equal to each other and in case of steady state conditions equal to the generation rate. However, this does not imply that the resulting change in carrier density contributes equally to the change of the conductivity e.g., charge carrier trapping can influence the number of carriers being transported.

With Eq (2.4) and (2.5) being equal and the introduction of a carrier capture rate $c_{c,v}$ it is possible to express the time dependent carrier rates as

$$\frac{d \Delta p}{dt} = \frac{d \Delta n}{dt} = g_{ph} - c_{c,v} n_{ph} p_{ph} \quad (2.6)$$

with the optical induced generation rate $g_{ph} = g_n = g_p$. The capture coefficient, which incorporates all carrier transitions from the conduction to the valence band, is introduced and discussed in detail in Appendix D. The resulting Eq. (2.6) is a first order differential equation which can be solved to acquire the time dependent behavior of a photoconductor. The solution

for the time dependent electron density $\Delta n(t)$, under the condition where light is switched on at time t_0 , leading to a constant carrier generation rate g_{ph} across the entire photoconductor, is

$$\Delta n(t) = n_{max} \cdot \tanh\left(g_{ph} c_{c,v} (t - t_0)\right), \quad (2.7)$$

With n_{max} the maximum electron density reachable under illumination, given by the ratio of the carrier generation and capture coefficient.

$$n_{max} = \sqrt{\frac{g_{ph}}{c_{c,v}}}, \quad (2.8)$$

Furthermore, it is possible to derive the decay time of the carrier concentration when the light is switched off at a time t_1 in the following form,

$$\frac{d \Delta n}{dt} = c_{c,v} n^2 \xrightarrow{\text{yields}} \Delta n(t) = n_{max} \frac{\tau_1}{(t - t_1)} \quad (2.9)$$

Figure 2.2 depicts the transient behavior of the carrier density for three different generation rates, g_1, g_2 and g_3 according to Eq. (2.7) and (2.9). In this plot the rise time τ_0 and fall time τ_1 are depicted as well, which can be expressed as

$$\tau_0 = \frac{1}{\sqrt{g_{ph} c_{c,v}}} \quad (2.10)$$

and

$$\tau_1 = \frac{1}{n_{max} c_{c,v}}. \quad (2.11)$$

2 Fundamentals

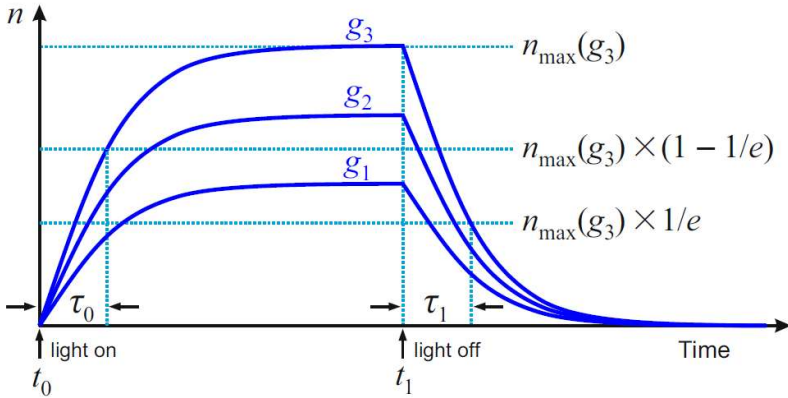


Figure 2.2 Plot of the transient behavior of the electron concentration upon on turning light on and off. The plots shown for 3 different generation rates with $g_3 > g_2 > g_1$. Further for the generation rate g_3 the time constants τ_0 and τ_1 are shown. Reprinted with permission from [126]. Copyright Springer International Publishing AG 2018.

Eq. (2.8) and the time constants Eq. (2.10) and (2.11) expresses a tradeoff that should be considered in the design of photodetectors. The capture coefficient, which is closely linked to the carrier lifetime plays an important role in determining both the maximum achievable responsivity and the dynamic behavior of photodetectors. Small capture coefficients result in larger carrier density, leading to high responsivities. However, they also impose limitations on the dynamic range of the photodetector by prolonging the rise and fall times. Therefore, it should be considered what is more desirable for an application for which a detector is designed. The presented relationship is simplified, but it holds true for most detectors. In other works, there are more detailed derivations of the dynamic behavior of photodetectors. [129]

The change in conductivity of photoconductive materials depends on the optical generation rate and the recombination rate. Therefore, the following sections will provide a detailed discussion on photon absorption leading to carrier generation, as well as the recombination mechanisms in semiconductors.

2.1.2 Photon Absorption in Semiconductors

The band gap magnitude of a semiconductors defines various attributes of the material. It also influences the absorption of photons in a semiconductor material. Photons with an energy E_{ph} , expressed as

$$E_{ph} = h \frac{c}{\lambda}, \quad (2.12)$$

with the wavelength λ , the speed of light c and h the Planck constant, which is larger than the band gap can be absorbed by the semiconductor and create an electron hole pair. The generation of the new carriers can be expressed as a wavelength dependent optical-induced generation rate, defined as

$$g_{ph} = \eta \phi_{in}(1 - R)\alpha e^{-\alpha z}. \quad (2.13)$$

In this equation R is the reflectance and represents the reflection of light on the surface of the optically absorbing material, ϕ_{in} the incoming light intensity, with α and η the wavelength dependent absorption coefficient and internal quantum efficiency. Furthermore, z describes the position within the illuminated sample.

For photodetectors it is ideal when the generation rate is as large as possible. Therefore, the individual parameters defining this rate are going to be analyzed. Namely the quantum efficiency, the reflectance, and the absorption coefficient.

Quantum efficiency

The quantum efficiency describes the ratio of absorbed photons to generated electron hole pairs. It approaches unity for photon energies that are in the range of the band gap energy. The efficiency can increase and even exceed unity for photon energies drastically larger than the band gap energy. Such an increase can occur if effects such as impact ionization or multiexciton generation take place.

Reflectance

The reflectance is an optical property that quantifies the amount of light or electromagnetic radiation that is reflected off the surface of a material, as opposed to being absorbed or transmitted through it. Figure 2.3. shows an incident wave at the interface of two different materials being reflected and transmitted.

2 Fundamentals

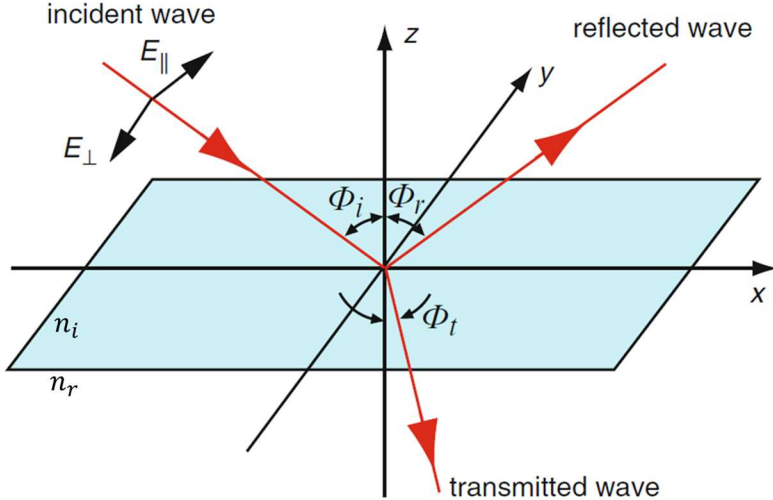


Figure 2.3. Illustration of incident light wave being reflected and transmitted at the interface of two materials. This illustration highlights the normal (E_{\perp}) and in plane (E_{\parallel}) component of the electric field vector. Furthermore, the angles of the incoming light Φ_i , the reflected Φ_r and transmitted wave Φ_t are shown. Reprinted with permission from [126]. Copyright Springer International Publishing AG 2018.

The reflectance is usually defined as the ratio of the power flux of the reflected wave to the power flux of the incoming wave and is split into the in plane and normal component R_{\parallel} and R_{\perp} of the wave. These components can be expressed as,

$$R_{\perp} = \left| \frac{n_i \cos \Phi_i - \sqrt{n_r^2 - \kappa^2 - 2in_r\kappa - n_i^2 \sin^2 \Phi_i}}{n_i \cos \Phi_i + \sqrt{n_r^2 - \kappa^2 - 2in_r\kappa - n_i^2 \sin^2 \Phi_i}} \right|^2 \quad (2.14)$$

and (2.15)

$$R_{\parallel} = \left| \frac{n_r \cos \Phi_i - n_i \sqrt{1 - (n_r + i\kappa)^2 \sin^2 \Phi_i}}{n_r \cos \Phi_i + n_i \sqrt{1 - (n_r + i\kappa)^2 \sin^2 \Phi_i}} \right|^2.$$

In this equation n_r and κ are the refractive index and extinction coefficient of an absorbing semiconductor material and n_i is the refractive index of a non-absorbing material in which the incoming wave travels to the

interface. In vacuum ($n_i = 1$) these equations can be simplified and expressed as

$$R_{\perp} \cong \frac{n_r - \cos^2(\Phi_i) + k^2}{n_r + \cos^2(\Phi_i) + k^2} \quad (2.16)$$

and

$$R_{\parallel} \cong R_{\perp} \frac{(n_r + \sin(\Phi_i) \tan(\Phi_i))^2 + k}{(n_r - \sin(\Phi_i) \tan(\Phi_i))^2 + k} \quad (2.17)$$

These equations are plotted for a fictive semiconductor in Figure 2.4. The plots shows that the reflectance never reaches zero, which highlights the critical role of material selection. Choosing an unsuitable material can result in a significant portion of light being reflected before it has a chance to be absorbed. In such cases, it is crucial to apply anti-reflection coatings or implement other schemes on the surface to enhance light absorption.

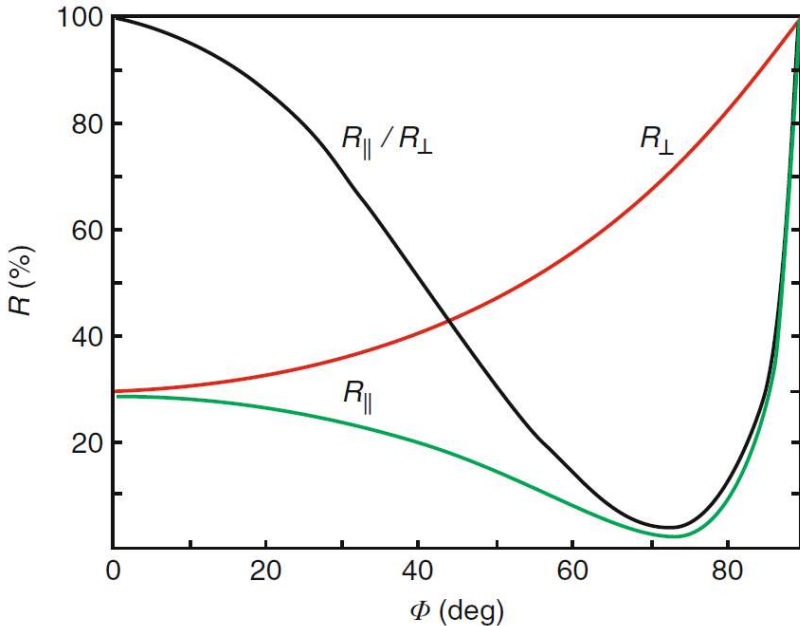


Figure 2.4. Plot of the reflectance as a function of the incident angel for $n_r=3$ and $k=1$. Adapted with permission from [126]. Copyright Springer International Publishing AG 2018.

2 Fundamentals

Absorption Coefficient

Another factor influencing the photo induced generation rate is the absorption coefficient, which characterizes a material's ability to absorb light.

The absorption of photons with energy greater than the band gap in direct band gap semiconductors is for most semiconductors large, allowing thin absorber layers to effectively absorb incoming light. Typically, the majority of the incoming photons are absorbed within the first hundreds of nanometers.

To illustrate the impact of the absorption coefficient on the intensity profile within a material, a homogeneous material without scattering, exposed to light with an initial intensity I_0 after surface reflections is considered. It is assumed that photogenerated electrons and holes rapidly redistribute within the absorbing material, avoiding local changes in absorption properties. Additionally, it is expected that photoexcited electrons and holes will quickly relax towards the band edges of the conduction and valence bands, respectively. Under these conditions, the Beer-Lambert Law can be used to describe the intensity profile within the material.

$$I_{ph} = I_0^{-\alpha x} \quad (2.18)$$

Utilizing this equation, it is possible to plot the intensity profile for different materials and their absorption coefficient, see Figure 2.5. In this plot the intensity trends for various materials are plotted. It's evident that for materials with a direct band gap (such as InP, Ge, and GaAs), the absorption is significantly stronger compared to a material with an indirect band gap (Si) and the intensity decreases very fast.

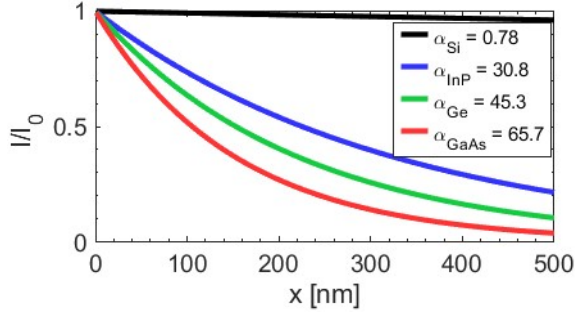


Figure 2.5. This plot shows the to the maximum intensity normalized Intensity plot within a material. The plot shows the intensity profile for materials with different absorption coefficients and for photons with an energy of 1.5eV (~827 nm). The plotted materials are silicon (Si), indium phosphide (InP), germanium (Ge) and gallium arsenide (GaAs). The absorption coefficients are given in units of [10^3 cm^{-1}].

The absorption coefficient can be modeled in different frameworks, in this work both a classical and quantum mechanical approach are presented.

In a classical and general approach, it is possible to relate α to other material properties such as the complex refractive index \tilde{n} expressed as

$$\tilde{n} = \mathbf{n} + k \quad (2.19)$$

This is done via the Poynting vector formalism, with $\langle S_z \rangle$ the pointing vector in z direction the angular frequency ω and the electric and magnetic fields E_x and H_y respectively. These fields are further described by their respective amplitudes E_0 and H_0 . With these fields the Poynting vector can then be defined as follows:

$$\begin{aligned} \langle S_z \rangle &= \frac{1}{2} \text{Re} [E_x \times H_y^*] \\ \langle S_z \rangle &= \frac{1}{2} \text{Re} \left[E_0 e^{\frac{i\tilde{n}}{c}z} * \frac{E_0^* H_0^*}{\mu_0 c} e^{\frac{-i\omega\tilde{n}^*}{c}z} \right] \\ \langle S_z \rangle &= \frac{1}{2} \frac{|E_0|^2}{\mu_0 c} \mathbf{n} e^{\frac{-4\pi k}{\lambda}z} \end{aligned} \quad (2.20)$$

The final expression in Eq (2.20) contains an exponential with a single exponent. This exponent defines the dampening of the Poynting vector and thus the absorption in the material. This classical approach allows to define the absorption coefficient as

2 Fundamentals

$$\alpha = \frac{4\pi k}{\lambda}. \quad (2.21)$$

The absorption coefficient can be further derived using a quantum mechanical approach. In this chapter, a general equation is given with a short discussion on its components without its derivation. The derivation can be found in more detailed literature.

The absorption coefficient between two bands, ν and μ , is given by

$$\alpha(f) = \frac{-2}{(2\pi)^3} \frac{q^2}{2\varepsilon_0 n m_0^2 c \nu f} \sum_{\mu, \nu} \int_{BZ} |q M_{\mu\nu}(\mathbf{k})|^2 \delta(E_{\mu}(\mathbf{k}) - E_{\nu}(\mathbf{k}) - hf) d\mathbf{k}. \quad (2.22)$$

This equation incorporates the square of the momentum elements matrix $|q M_{\mu\nu}(\mathbf{k})|^2$, which is proportional to the number of optically induced transitions. Essentially, it represents the squared expectation value that depends on the overlap of the wavefunctions corresponding to states in the ν and μ bands. This overlap reflects the degree of similarity or correlation between the quantum states represented by the wavefunctions in the two bands.

Additionally, the equation incorporates a proportionality factor describing the probability of a transition due to the interaction of light with an electron. This factor introduces the Dirac delta function, ensuring that the contribution is valid only for transitions occurring from one energy state to another when the energy of the photon is equivalent to the gap energy $E_{\mu}(\mathbf{k}) - E_{\nu}(\mathbf{k})$ of the two bands.

This formalism allows for the introduction of various band structures independent of the underlying band models. Finally, by integrating this over the first Brillouin zone and a summation of the discrete transition, it is possible to describe the absorption coefficient.

2.1.3 Recombination

After discussing the optical generation rate and the parameters influencing it, this section presents an examination of the recombination mechanism in semiconductors.

Recombination effects can be categorized into two major categories: radiative recombination and non-radiative recombination. In the case of non-radiative recombination processes, the energy of the carriers is transferred to either other carriers or to the lattice in form of phonons. On

the other hand, in the case of radiative recombination, the energy of the recombining carrier is released in the form of a photon. In this section the focus is on non-radiative recombination which is usually an unwanted process.

Various non-radiative recombination processes involve energy states within the band gap that result from defects in the semiconductor. These defect states may interact with only one energy band (either valence or conduction), capturing and releasing carriers within that band. Such defect states are referred to as carrier traps, which do not contribute to carrier recombination. In contrast, recombination centers are defect states which interact with both bands and drastically influence carrier recombination dynamics. Defect centers and the including carrier dynamics and rates are discussed in detail in Appendix D.

In general electron and hole recombination rates r_n and r_p of a recombination process can be expressed as

$$r_n = \frac{n}{\tau_n} \quad \text{and} \quad r_p = \frac{p}{\tau_p} . \quad (2.23)$$

In this equation n and p are the electron and hole densities and τ_n and τ_p the respective carrier lifetimes. This equation further entails the assumption that the recombination probability of the free carriers per unit time and in a unit volume is approximated by $1/\tau_{n,p}$.

The non-radiative recombination processes can usually be viewed as individual processes. Their contributions can be superimposed to a total recombination rate resulting in a total carrier lifetime τ_{tot} which is defined as

$$\tau_{tot} = \left(\frac{1}{\tau_1} + \frac{1}{\tau_2} + \frac{1}{\tau_3} \dots \right)^{-1} , \quad (2.24)$$

where τ_i ($i = 1,2,3, \dots$) corresponds to the lifetime of an individual recombination process. The individual recombination mechanisms corresponding to these lifetimes will be discussed in the following sections.

Shockley-Read-Hall Recombination

The SRH (Shockley-Read-Hall) recombination is a mechanism involving deep-level defect centers and is of great importance in semiconductors with large defect densities. This recombination mechanism describes the process of a charge carrier being captured and then either being transferred to a

2 Fundamentals

different band where it can recombine with a carrier of the opposite charge or being emitted back to the band form which it originated.

For this model it is possible to derive the net recombination rate U with help of the intrinsic carrier concentration n_i , the fermi level energy E_F , the trap state energy E_t , the Boltzmann constant and temperature T as

$$U = \frac{(np - n_i^2)}{\tau_{p0} \cdot \left(n + n_i e^{\frac{E_t - E_F}{k_B T}} \right) + \tau_{n0} \cdot \left(p + n_i e^{\frac{E_F - E_t}{k_B T}} \right)}. \quad (2.25)$$

With Eq (5.8) and (5.10) , in Appendix D, the electron and hole lifetime τ_{p0} and τ_{n0} can then be expressed as:

$$\tau_{p0} = \frac{1}{c_{trap,v} N_t}, \quad \tau_{n0} = \frac{1}{c_{c,trap} N_t}. \quad (2.26),(2.27)$$

These equations describe how the trap state densities influence the carrier lifetime and thus the SRH recombination rate. Lower trap densities lead to longer carrier lifetimes, which in turn enhance the photodetector performance. Therefore, reducing trap densities is a key strategy in optimizing semiconductor photodetectors and advancing their capabilities.

Non-Radiative Recombination and Multi Phonon Emission

A recombination process similar to SRH recombination is the multi-phonon emission process. The key distinction from SRH recombination is that in this process, multiple phonons are emitted during capturing a charge carrier, altering the energetic position within the band gap of the defect states involved in the recombination process.

An intuitive description of this process is as follows: When lattice vibrations are sufficiently strong, the energy state of a defect level can approach the conduction band, making it more likely to capture an electron. Upon capturing an electron, the excess energy is dissipated in the form of intense lattice oscillations, causing an energy shift closer to the valence band. In this position, the defect can act as a trap for holes, facilitating band-to-band recombination. [130]

Auger Recombination

The Auger recombination process differs from previously mentioned recombination processes in how the energy released due to recombination

is dissipated and that it does not involve defect states. Considering SRH recombination, the energy released when an electron and hole recombine is typically transmitted to the lattice in the form of phonons. However, for Auger recombination processes the energy resulting from electron and hole recombination is transferred to a third carrier, which can be either an electron or a hole.

In most semiconductors, it is generally preferred to transfer the energy of the recombination process to an electron, primarily due to its lower effective mass compared to holes. However, this preference can vary depending on the specific band structure and characteristics of the semiconductor material. When an electron and hole recombine and the energy is transferred to a second electron in the conduction band it will be elevated to a higher energy state. The excited carrier then returns to its ground state within the conduction or valence band by a relaxation process emitting phonons. The Auger recombination rate for low excitation regime can be expressed as

$$\tau_A = B n^2 p \quad (2.28)$$

with the Auger lifetime for an electron $\tau_{A,n}$

$$\tau_{A,n} = \frac{1}{B n^2}, \quad (2.29)$$

for holes the lifetime can be calculated in identical fashion using the hole concentration. The coefficient B is the Auger coefficient and typically in the range of $10^{-30} \dots 10^{-22} \text{ cm}^6 \text{ s}^{-1}$.

The Auger lifetime can also be derived in quantum mechanical framework which leads to the expression,

$$\tau_A \approx \frac{\pi \hbar (4\pi q \epsilon_0 \hbar^2)^2}{24 q^4 m_n} \frac{\Delta E}{kT} \frac{\sqrt{2}}{0.01} e^{\frac{\Delta E}{k_B T}}, \quad (2.30)$$

for the Auger lifetime τ_A , with

$$\Delta E = \left[\frac{2m_n + m_p}{m_n + m_p} \right] E_G, \quad (2.31)$$

and m_n and m_p the electron and hole mass. This equation expresses the influence of the band gap energy on Auger recombination. As the band gap decreases, Auger recombination becomes more dominant. Additionally, it can be seen that the Auger recombination exhibits a strong dependence on carrier concentration. Therefore, in semiconductors with small band gaps and heavy doping, Auger recombination can become particularly significant.

2 Fundamentals

The Auger recombination is also the dominant recombination mechanism in quantum dots. This is attributed to momentum conservation processes differing in quantum dots compared to bulk semiconductors.

The challenge in bulk semiconductors is finding three carriers whose momenta exactly balance. This is particularly true in indirect band gap semiconductors, where momentum conservation can be a more significant limiting factor due to the need for phonon involvement to balance momentum discrepancies.

In quantum dots, the situation differs due to quantum confinement effects. Quantum confinement leads to discrete energy levels similar to atoms, and the wavefunctions of carriers are spatially confined. This confinement results in broadened momentum states, effectively relaxing the strict requirements for momentum conservation. In quantum dots, momentum conservation does not need to be as precise as in bulk materials because the wavefunctions spatial confinement allows for greater flexibility in momentum matching.

Consequently, Auger recombination becomes more probable in quantum dots. The overlap of electron and hole wavefunctions within the confined space increases the likelihood that all conservation laws (both energy and momentum) will be satisfied during the recombination process.

2.1.4 Noise

In every electronic system, fluctuations of the electronic current occur over time. The origin of the fluctuations can have various reasons such as statistical variations in mobility, electric field, carrier density, and others. These fluctuations are typically not desired and termed as electrical noise.

The noise current $i_n(t)$ in an electrical system can be defined as the difference of the fluctuating signal $I(t)$ and a time averaged current $\langle I(t) \rangle$,

$$i_n(t) = I(t) - \langle I(t) \rangle \quad (2.32)$$

An additional, often-used, quantity to describe the noise of a signal is the noise spectral current density S . In contrast to the definition in Eq. (2.32), which describes the fluctuations in time-domain, this metric is used to describe the noise in the frequency domain. It can be described as the variance of the signal in a window of the width Δf around a center frequency f_0 and can be expressed for a current as

$$S_I(f_0) = \frac{1}{\Delta f} \int_{f_0 - \Delta f/2}^{f_0 + \Delta f/2} |i_n(f)|^2 df, \quad (2.33)$$

with $i_n(f)$ the Fourier transformed signal $i_n(t)$. In analogy it is possible to define a noise spectral voltage density utilizing a voltage signal S_v . If the observed system exhibits Ohmic behavior, the two noise spectral densities are related through the resistance R_{noise} via

$$S_v = R_{noise}^2 S_I \quad (2.34)$$

2.1.4.1 Shot Noise

Shot noise arises from the discrete nature of electrons and their motion within a conductor. Due to this discrete nature the number of electrons moving through a conductor and arriving at an electrode will vary over time. Such fluctuations, even under constant applied voltages, result in measurable external current fluctuations. These fluctuations are known as shot noise. This noise scales with the magnitude of the current $\langle I(t) \rangle$ and its variance or spectral power density can be expressed as a current noise or voltage noise,

$$S_{I,shot} = 2 q \langle I(t) \rangle \quad (2.35)$$

$$S_{v,shot} = 2 q \langle I(t) \rangle R_{noise}^2 \quad (2.36)$$

It should be mentioned that the shot noise is frequency independent. This can be attributed to the randomness of the carrier movement which does not exhibit any frequency dependence.

2.1.4.2 Thermal Noise

Thermal noise (Johnson-Nyquist noise) is present in every conductor and originates from motion fluctuations resulting from thermal energy fluctuations. Thus, if the temperature of a conductor increases the thermal energy increases leading to larger carrier movements and finally in larger noise. The thermal noise spectral power density can again be expressed in terms of a voltage and a current

$$S_{v,thermal} = 4 k_B T R_{noise}, \quad (2.37)$$

$$S_{I,thermal} = \frac{4 k_B T}{R_{noise}}, \quad (2.38)$$

with R_{noise} the resistance of the conductor. An important observation can be made when analyzing these equations. The thermal noise is independent from the applied voltage and current. Its magnitude is solely

2 Fundamentals

determined by the resistance of the conductor and therefore fundamental and can limit device operation. Furthermore, it is frequency independent.

2.1.4.3 Generation-Recombination Noise

In semiconductor devices, generation and recombination noise arises from stochastic processes that affect the carrier concentration. These processes include trapping and de-trapping, carrier injection into the semiconductor, and various recombination mechanisms. Such fluctuations manifest as noise in externally measured signals. The intensity of this noise depends on factors including the carrier lifetime, trap density, and the rates of carrier generation and recombination. This type of noise can be expressed as

$$S_{I,G-R} = 4 \left(\frac{I}{N} \right)^2 \frac{\tau}{(1 + 4\pi^2 f^2 \tau^2)}, \quad (2.39)$$

with the frequency f and N the total number of carriers. This noise shows a characteristic spectral behavior. Up to the corner frequency $f_{G-R} = 1 / (2 \pi \tau)$ the noise power remains constant, beyond which it decreases with $1/f^2$. The time constant τ represents the carrier lifetime of a charge carrier with respect to a specific process influencing the concentration. In semiconductors, several of these generation recombination processes simultaneously contribute to noise, allowing the overall noise to be viewed as a superposition of these individual power densities. This will be further discussed in the next section.

2.1.4.4 1/f Noise

1/f noise, also known as flicker noise or pink noise, is a type of electrical noise with a characteristic power spectral density that decreases inversely with frequency. While its exact origins remain debated, various factors can influence its magnitude, often differing between materials. These factors include defects and impurities within the material, the total number of charge carriers involved in current flow, temperature gradients, mechanical stress, and statistical variations in carrier density. Defects and impurities are particularly relevant, as the observed scaling of noise with material volume suggests more defects lead to higher noise levels.

Furthermore, the noise originating from defects and impurities is often generation-recombination noise, which typically exhibits a Lorentzian shape, Eq. (2.39). When several such individual spectra are superimposed, a $\sim 1/f$ spectral dependency can often be observed. Consequently, generation-

recombination noise is frequently considered as a major component of the broader $1/f$ noise spectrum. However, while it is seen as significant contributor, other sources of noise may also influence the overall noise characteristics. In general the power spectral density of the $1/f$ noise can be expressed as

$$S_{I,1/f} = \frac{1}{f} \frac{\alpha_H \langle I(t) \rangle^2}{nV} \quad (2.40)$$

In this equation, α_H represents the Hooge's constant, which is an empirical material dependent value. This constant can vary widely, from 10^{-9} to 10^{-3} , depending on the specific material. This large range of possible values underscores the fact that different materials exhibit different levels of noise magnitude, indicating that various effects contribute to noise generation in varying strengths across different materials.

A potential noise spectrum showing the noise spectra of two distinct traps in the low-frequency regime, alongside $1/f$ noise and thermal noise is shown in Figure 2.7.

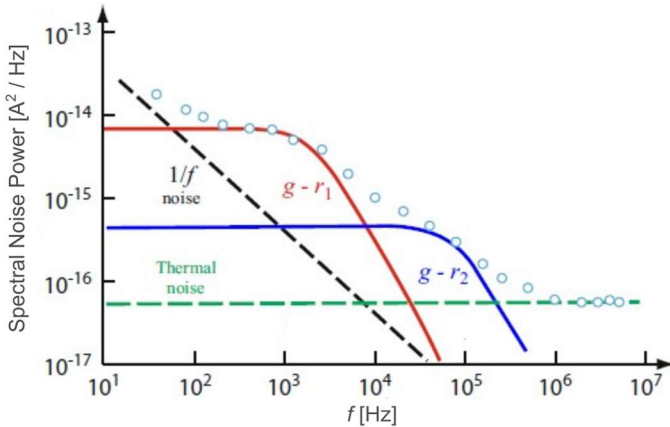


Figure 2.6. Spectral noise Power vs frequency. The solid red and blue line indicate the noise spectral power density corresponding to two distinct generation and recombination noise sources of two different trap states with their differing lifetimes. The green dashed line shows the thermal spectral noise power density resulting from the resistance of the observed device. The black line shows spectral characteristic of the $1/f$ noise. The blue and white dotted line shows the superposition of the individual noise components, illustrating the noise which would be measured in a device with these noise sources. Reprinted with permission from [126]. Copyright Springer International Publishing AG 2018.

2 Fundamentals

2.1.5 Figures of Merit & Metrics

To effectively quantify, characterize, and compare the properties of a photodetector, it is essential to define metrics and figures of merit. Here, the necessary metrics for this study using commonly accepted terminology are introduced.

- Active device area A is the physical area which is able to convert incoming light.
- Channel length l_{ch} defines the distance between the source and drain electrode.
- Channel width w_{ch} is the width of the active area between the source drain electrodes.
- Incident Power P_{in} , describes the incoming power on the active detector area.
- Incoming photon flux ϕ_{in} is defined as the number of photons per second incident on the active detector area and can be expressed with the incident power and the photon energy E_{ph}

$$\phi_{in} = \frac{P_{in}}{E_{ph}} \quad (2.41)$$

- Photocurrent I_{ph} is the externally measured change of the electric current as a result of illumination and can be defined with the electric current under illumination and in dark I_{dark} and I_{light}

$$I_{ph} = I_{light} - I_{dark} \quad (2.42)$$

- Responsivity R , is the ratio of the photocurrent I_{ph} and the incident light power P_{in}

$$R = \frac{I_{ph}}{P_{in}} \quad (2.43)$$

- External quantum efficiency EQE expresses the ratio of externally collected photogenerated carriers to the number of incident photons

$$EQE = \frac{I_{ph}}{q \phi_{in}} \quad (2.44)$$

- Specific detectivity D^* is a figure of merit that provides a measure of the signal-to-noise performance of a photodetector, taking into account both its responsivity and noise characteristics relative to the device's active area. It quantifies the detector's ability to detect weak optical signals in the presence of electrical noise.

$$D^* = \frac{R \sqrt{A}}{S_n} \quad (2.45)$$

2.1.6 Photoconductive Gain

Lastly, photoconductive gain, which can also be considered as a metric of photodetectors, is introduced and discussed.

The magnitude of the photoresponse is not only defined by the generation and recombination rates but can also be influenced by the transport and trapping of charge carriers which can lead to photoconductive gain.

Photoconductive gain can be described as the relationship between absorbed photons and externally detected electrons/holes. This can be understood by considering the scenario depicted in Figure 2.7. This illustration shows the absorption of a photon and subsequent generation of an electron-hole pair which is then transported to electrodes due to an externally applied bias.

Under an externally applied bias, the photogenerated electron and hole migrate in opposite directions toward the electrodes. If, for instance, the electron mobility is larger than the hole mobility and the electron thus reaches the contact faster than the hole and exits the photoconductor, a new charge carrier must be injected at the opposite electrode to maintain charge neutrality. This process may occur multiple times. Although only one photon has been absorbed externally, several electrons can be detected. For this to be possible, the hole carrier lifetime needs to exceed the electron transit time, which will be discussed in more detail.

2 Fundamentals

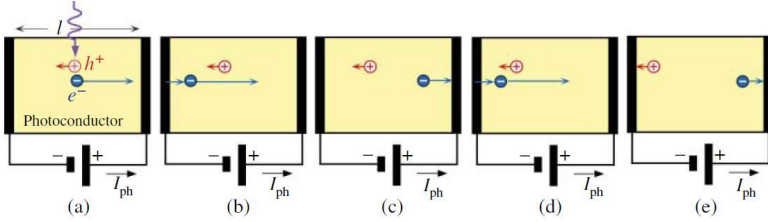


Figure 2.7. Illustration of the motion of a photo-generated electron hole pair in a photoconductor due to an external applied E-field, with the electron mobility being greater than the hole mobility. a) Generation of electron hole pair at t_0 and indication of movement of individual carriers by red and blue arrows. b) Electron hole pair at time $t_1 > t_0$ after which the electron has been collected at the right contact and new electron is injected from the left, whereas the hole has not reached the left contact yet. c) $t_3 > t_2$ both charge carriers have moved closer to individual contacts. d) $t_4 > t_3$ repetition of situation described in b). e) Both carriers reaching the contact allowing for carrier extraction while maintaining charge neutrality. Adapted with permission from [123]. Copyright 2022 John Wiley & Sons Ltd.

For the case that the photogenerated carrier density is larger than the intrinsic carrier concentration ($\Delta n \Delta p \gg n_d p_d$), the carrier concentration change upon illumination can be expressed as $\Delta n = g_0 \tau_n$. Under this assumption it is possible to express the gain as

$$\Gamma = \frac{\text{Rate of external electron flow}}{\text{Rate of light induced electron generation}} = \frac{(\mu_n \tau_n + \mu_p \tau_p) E}{l_{ch}}, \quad (2.46)$$

with l_{ch} the channel length. By introducing the transition time of carriers as $t_{tr,n} = l_{ch} / (\mu_n E)$ this equation can be expressed as

$$\Gamma = \frac{\tau_n}{t_{tr,n}} + \frac{\tau_p}{t_{tr,p}} \quad (2.47)$$

This equation is valid for the case that electrons and holes both contribute to the transport. The transition time is dependent on both the mobility and the electric field. By increasing the E-field the gain will increase accordingly until the space charge limits the injection of carriers.

The space charge limit can be calculated by viewing the photoconductor as dielectric with the capacitance $C = QV_{lim} = \epsilon_0 \epsilon_r V_{lim} / d$ with V the applied voltage over a device with the length d . The transition time through the device can be expressed as $t_r = d^2 / \mu V$. With this it is possible to

express the maximum current density limit after which the injection is limited as

$$J_{scl} = \frac{Q}{t_r} = \frac{\epsilon_0 \epsilon_r \mu V^2}{d^3} \quad (2.48)$$

This voltage limit after which the gain will be limited can now be expressed as $V_{lim} = \sigma d^2 / \epsilon_0 \epsilon_r \mu$.

Carrier traps can have a significant influence on the gain in photoconductors. While deep level traps can lead to an increased carrier recombination rate, shallow traps with long lifetime t_{trap} where carriers become immobile can increase the gain. This increase occurs when e.g., a photoexcited hole is trapped for a time t_{trap} and a corresponding electron cycle for the same duration through the device with a transition time shorter than the trapping time. Such traps are often referred to as sensitizing centers. In case the trap density is large and the lifetime thereof long the gain can be expressed as

$$\Gamma = \frac{t_{trap}}{t_{tr,n/p}}, \quad (2.49)$$

with the trap lifetime of

$$t_{trap} = \frac{1}{v_{thermal} S_{nonrad} e^{-\Delta E / k_B T}} \quad (2.50)$$

and a thermal carrier velocity $v_{thermal} = \sqrt{3k_b T / m_n^*}$. and the capture cross section S_{nonrad} .

The lifetime, trapping, and transit time for charge carrier can be tuned in various ways utilizing different schemes and device architectures, thus engineering the gain.

2 Fundamentals

2.2 Colloidal Quantum Dots

This section introduces the fundamental theory and definitions related to cQDs and is mostly based on literature[123, 128, 131, 132] if not cited differently.

2.2.1 Introduction

Quantum dots (QDs) are crystalline semiconductors composed of a few to hundreds of thousands of atoms, typically ranging in size from a few nanometers to several tens of nanometers. Due to their nanometer size QDs can exhibit extraordinary properties which can greatly vary compared to their bulk material counterpart. One important size-dependent effect is the influence of particle size on the band gap of materials. This tunability allows to vary the photon absorption and emission over large wavelength regimes. QDs can be employed from the UV to LWIR spectral range, depending on the material system.

These versatile nanomaterials can be fabricated utilizing various methods, including lithography processes, molecular beam epitaxy, electrochemical synthesis, gas-phase processes, colloidal synthesis, and others. When the quantum dots are dispersed in a solution after their synthesis they are referred to as colloidal QDs (cQDs). These types of QDs are usually synthesized in solution. The colloidal synthesis is a cost-efficient production method which allows large batch fabrication with narrow size distribution. A further advantage of cQDs is that the in solutions dispersed cQDs can be deposited utilizing cost efficient and simple methods.

Generally, cQDs exhibit several advantages over conventional bulk materials such as, optical tunability, solution processability, high quantum yield and more. These advantages can make them ideal candidates for various applications and devices. In this section, an introduction to the fabrication, processing, and physics relevant for photodetectors utilizing cQDs is presented.

2.2.2 cQD Synthesis

The challenge in fabricating cQDs lies in finding methods which enable precise control over their size, size distribution, chemical composition, and monodispersity in solution, while ensuring long term stability. A method found ensuring these factors for a variety of material compositions is the

synthesis of cQDs in solution typically utilizing the heating up or hot injection method.[133]

La Mer's model[134] provides a basic framework for understanding the synthesis of QDs in solution. The model divides the synthesis process into three stages, as illustrated in Figure 2.8. Initially, chemical precursors are mixed in a suitable solution which undergo reactions forming monomers until reaching a critical supersaturation threshold. This leads to the destabilization of the solution, forcing monomers to aggregate and formation of nuclei. Subsequently, in the third stage, nucleation stops, and a constant influx of monomers to the nuclei facilitates the growth of QDs. This growth continues until the depletion of monomers is reached or the reaction is stopped by external means, e.g. cooling of the reaction mixture. If not stopped the cQDs can still grow even after depletion of the monomers. This growth is possible via Ostwald ripening, wherein small QDs dissolve, providing monomers for the growth of larger QDs.

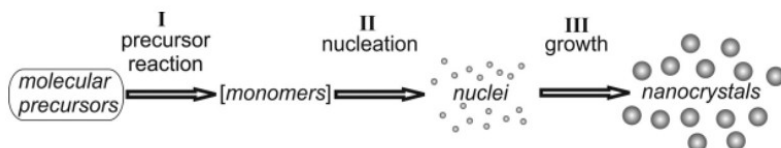


Figure 2.8. Schematic of the basic synthesis process of nanocrystals according in accordance with La Mer's model. Reprinted with permission from [128]. Copyright 2010 Cambridge University Press.

Throughout the nucleation and growth phases, molecules in the solution will adhere to the surface of the nuclei and cQDs. These molecules, referred to as surfactants or ligands, serve to stabilize them chemically and physically, ensuring monodispersity. They also play a critical role in the reaction kinetics, thereby influencing the composition, shape, size, and other properties of the cQDs.

After the cQDs have reached the desired size and further growth has been stopped, the solution containing the cQDs must be purified. This crucial step is commonly referred to as washing. The washing process involves multiple solvent exchanges and centrifugation steps, which aim to remove unreacted precursors, excess reagents, reaction by-products, and other impurities. This purification ensures the purity and stability of the final product.[41]

2 Fundamentals

2.2.3 cQD Deposition and Ligand Exchange

One of the greatest advantages of cQDs is the possibility to use cost-effective and simple deposition methods to deposit layers on various materials. Moreover, depositing cQDs from solution enables the deposition of uniform layers over large areas with very good thickness control, using conventional methods such as spin coating, spray coating and ink jet printing. These deposition methods not only enable the possibility of streamlining the manufacturing process but also enhances the scalability of production, making cQDs an attractive choice for industry. [26]

During the synthesis of cQDs the number of available ligands which can be used are quite limited. The ligands chosen for synthesis are mostly long carbon chain molecules that are thermally and chemically stable. Although they are suitable for synthesis they also impose several limitations. Most importantly, they are often insufficient in passivating the surface of the cQDs after deposition. Furthermore, due to their length they spatially separate the cQDs after deposition, which results in poor electric conductivity. Hence, ligand exchange methods have been developed to address these limitations and exchange the long organic ligands for shorter ones or an ionic shell. [135]

The Ligand exchange can be accomplished through two methods: ligand exchange in solution and solid-state ligand exchange. In the solution-based approach, the cQD solution is mixed with a solution of different polarity containing the desired new ligands. As the new ligands attach to the cQDs, replacing the initial ligands, they become soluble in the new solution resulting in a transfer of the cQDs into the solvent with the different polarity. The resulting cQD solution is often referred to as ink and can be deposited after purification.

In a solid-state ligand exchange, a layer-by-layer approach is used to exchange the surface ligands of cQDs. Initially, a layer of cQDs with long insulating ligands is deposited onto a substrate. Subsequently, the deposited layer is immersed in a solution containing the desired new ligands, resulting in the ligand exchange. After sufficient time for exchange, the substrate is rinsed to remove any residual long-chain ligands and excess new ligands. This process of deposition, ligand treatment, and rinsing can be repeated multiple times until the desired layer thickness is achieved.

The ligand exchange process plays a crucial role in the fabrication of photodetector devices, as it enables better electrical properties, the reduction of noise, enhancement of responsivity, and improvement of long-term device operation stability.

2.2.4 Quantum Confinement and Optical Characteristics of cQDs

In bulk semiconductor materials, the band gap is a fundamental characteristic that defines various properties of the material. Among these properties are the optical absorption and emission, since the band gap determines the energy required for electronic transitions within the material.

While the band gap is a fundamental characteristic for bulk materials it is not for cQDs. When a bulk material is significantly reduced in size reaching the nanometer regime, the quasi-continuous bands split up and the band gap changes. Therefore, the optical properties undergo substantial changes as well. This effect is of a quantum mechanical nature and often referred to as quantum confinement effect.

An electron-hole pair in a semiconductor can form a bound state due to their electrostatic attraction which is referred to as exciton. This bound state exhibits a characteristic radius similar to that of a hydrogen atom. This is the exciton radius r_{ex} and can be expressed as

$$r_{ex} = \frac{\epsilon_r \epsilon_0 \hbar^2}{\left(\frac{1}{m_n} + \frac{1}{m_p}\right) \cdot q^2} \quad (2.51)$$

This radius is typically used as an indicator when the quantum confinement effect is relevant. If the cQD radius is smaller than the exciton radius it is expected to observe confinement effects. Due to the confinement the quasi-continuous band splits into discrete energy states. Furthermore, the gap between the filled and unfilled energy states widens. This splitting is illustrated in Figure 2.9.

2 Fundamentals

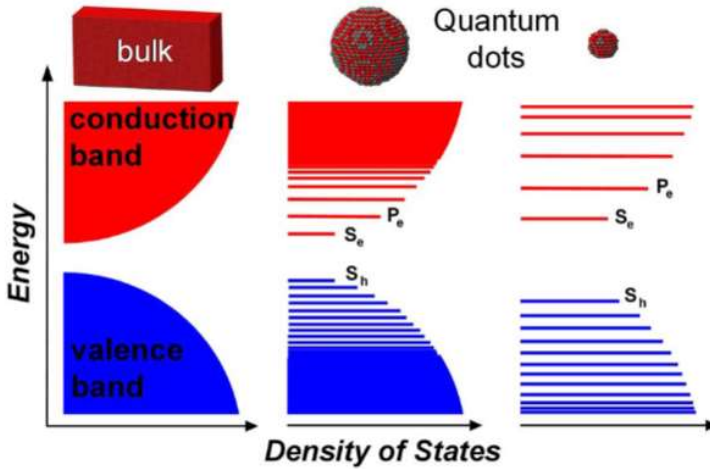


Figure 2.9. Density of states vs. energy of a semiconductor bulk material and QDs with two different sizes. It is shown that for cQDs the quasi-continuous bands split up into discrete energy levels. Furthermore, it is shown that for smaller cQDs the energy band splitting becomes greater. Reprinted with permission from [132]. Copyright 2020 Springer Nature Switzerland AG.

Due to the splitting of energy states, only specific photon induced energetic transitions are permitted this results in local absorption maxima in the absorption spectra. These local maxima can be used to gain information regarding the physical size distribution of the cQDs. A narrow size distribution results in a narrow and strong absorption peak. Furthermore, the absorption onset in cQDs exhibit a blue shift compared to the corresponding bulk material and can be controlled by varying the size of the cQDs. Figure 2.10 displays the absorption spectra of cQDs with different sizes and local absorption maxima due to discretization.

The quantum confinement effect in cQDs can be understood with the help of a simple “particle in a sphere model” which is very similar to the “particle in a box” model. This model describes a particle in a spherical quantum well (radius a) with the potential $V = 0$ inside the well ($r < a$) and outside a potential of $V = \infty$ of the well ($r \geq a$).

This problem can be solved with the help of the time independent Schrödinger equation. The wave function used to describe the carriers is

$$\Psi(r, \theta, \phi) = C j_l(\mathbf{k}r) Y_l^m(\theta, \phi), \quad (2.52)$$

with r, θ, ϕ being the radius azimuth and elevation of a spherical coordinate system, $j_l(kr)$ the spherical Bessel function of l -th order and $Y_l^m(\theta, \phi)$ a spherical harmonic. With the boundary conditions forcing the wavefunction to zero at the boundary the solution to the energy states within the spherical dot yields

$$E_{n,l} = \frac{\hbar^2 k^2}{2m} = \frac{\hbar^2 \beta_{n,l}^2}{2m_{n,h} a^2}, \quad (2.53)$$

with $\beta_{n,l}$ being the n^{th} zero of the Bessel function and $m_{n,h}$ the electron or hole mass. This equation yields a solution similar to the particle in the box, showing a scaling of the dominant confinement energy with $1/a^2$. Furthermore, the energy states are dependent on the quantum number n , and l which are similar to s, p and d which are used to describe the orbitals in hydrogen atoms. In Figure 2.10 the allowed transitions for three cQDs are shown.

2 Fundamentals

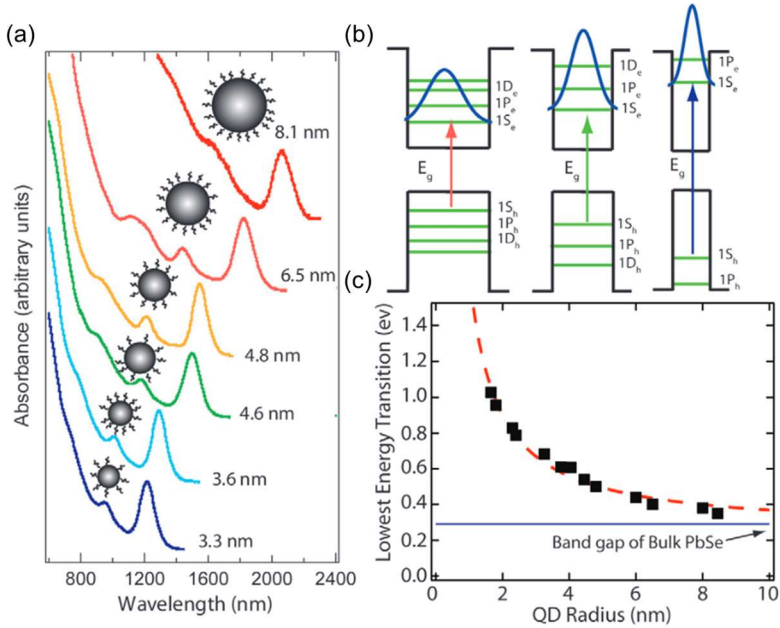


Figure 2.10. Different illustrations and effects resulting from the size dependent bandgap of cQDs. (a) Wavelength dependent absorbance for cQDs with different radii, the exciton peak is red shifted with increasing cQD diameter. (b) Illustration of the potential well and energy levels in a cQD. By decreasing the size an increase of the energy level splitting is observed. (c) Lowest energy transition within a cQD dependent on the QD radius. Adapted with permission from [136]. Copyright 2012 Elsevier Ltd.

The concepts derived from the spherical model hold true for experiments and coincide with more advanced models, but the exact values of the energy levels do not. Thus, more advanced models are needed to make accurate quantitative predictions. Such more advanced models can e.g. include the lattice potential utilizing Bloch's theorem, account for electrons and holes in an excited cQD and account for Coulomb interactions.

One of the first models to include these effects was the Brus model.[137, 138] This model yields an expression of the energy states of the form

$$E_{n,l} = E_{g,Bulk} + \frac{\hbar^2 \beta_{e,n,l}^2}{2m_n a^2} + \frac{\hbar^2 \beta_{h,n,l}^2}{2m_h a^2} - E_c \quad (2.54)$$

This equation contains three energetic contributions: (1) as a lower energy limit, the bulk band gap energy $E_{g,Bulk}$, (2) the quantum confinement energies for electrons and holes with their corresponding Bessel functions and (3) a contribution from the Coulomb attraction of the carriers E_c which is given by $1.8/(4\epsilon\pi a)$.

These analytical solutions are able to describe the basic concepts and tendencies of the energetic states in cQDs with their different contributions, but when compared to experimental results still differ. If the exact energy states including band splitting are needed DFT (density function theory) simulations or more advanced models are needed.

The electronic properties of cQDs are determined not only by the lattice constituent atoms and size, but also by the ligands attached to their surface. The significance of the cQD surface becomes apparent when considering their large surface-to-volume ratio. One of the primary effects of the ligands bound to the surface is the alteration of the energetic position of energy levels relative to the vacuum energy. This shift is typically attributed to a dipole moment induced by the binding and structure of the molecules attached to the surface.

Furthermore, the ligands do not only change band edges relative to the vacuum level energies but can also introduce doping. Doping in bulk materials is realized by the implantation of donor or acceptor atoms into the lattice, for cQDs it is already sufficient to add such atoms to the cQD surface. By exposing cQDs to an excessive amount or certain ligands it is also possible to dope them by inward diffusion. The influence of the surface ligands on the energy states and Fermi level of PbS has been extensively studied, in Figure 2.11 the energy states of PbS can be seen for a variety of ligands.

One of the most important influences of ligands on the electronic properties of cQDs is their impact on the electron and hole mobility of a cQD layer. Ligands can significantly influence the electronic coupling of cQDs, affecting their ability to transport charge carriers. This will be discussed in more detail in the next section.

2 Fundamentals

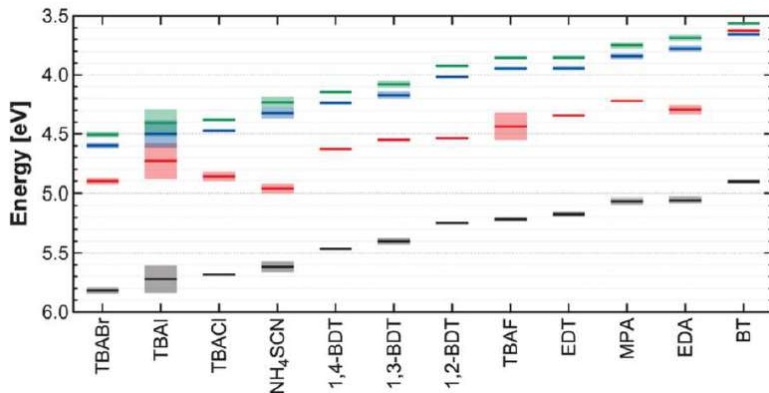


Figure 2.11. Illustration of the energy levels of PbS cQDs with respect to the vacuum energy for different ligands. Reprinted with permission from [139]. Copyright 2014 American Chemical Society.

2.2.5 Charge Transport in cQD Assemblies

The transport of charge carriers in cQDs is a complex and still extensively researched topic. This discussion will provide an overview of the relevant concepts and models, for a more detailed analysis, readers are referred to literature.[140–142]

Enhancing the conductivity through increased mobility in cQDs can significantly improve the performance of devices that use these materials, particularly in photodetectors. Since, higher mobilities lead to shorter carrier transit times and increased diffusion lengths, it is expected that more photogenerated carriers can be collected at the contacts before they recombine leading to a larger photoresponse.

The carrier transport in cQDs solids is often referred to as carrier hopping, because the transport can be pictured as carriers hopping from one cQDs to another, see Figure 2.12.[143] This hopping process can, in its essence, be compared to a quantum mechanical tunneling process with the rate of transition being strongly influenced by both the distance over which the tunneling occurs and the alignment of the energy states from which a charge carrier tunnels to another. With this picture in mind, it should become clear that achieving large mobilities in cQDs necessitates a narrow size distribution, which results in minimal variations in energy states and thus more frequent hopping. Additionally, close packing achievable by

ligand exchange is crucial for large mobilities. Models describing such a hopping transport in cQD solids have already been proposed in the 1980s by Shkolovskii and Efros[144] and it was later found that they are in good agreement with disordered cQD assemblies.[145]

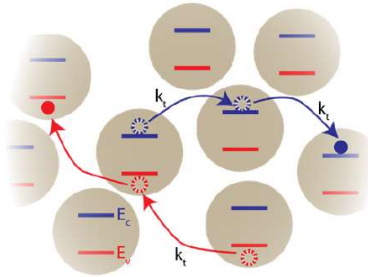


Figure 2.12. Charge transport in disordered cQD cluster. Red and blue arrows and dots indicate the movement of electrons and holes defined by a hopping rate k_t . Adapted from [146].

Other models describing the transport properties of cQDs are adapted from theories established in the field of chemistry and biochemistry. Applying such theories and models to cQDs is obvious when comparing the electronic energy states in molecules, such as the lowest unoccupied molecular orbital (LUMO) and highest occupied molecular orbital (HOMO), and the electronic states in cQDs.

Marcus theory is such a model which originates from the field of theoretical chemistry but is frequently applied to cQDs. The models derived have shown good agreement with experimental results for electron hopping transport in cQDs. Other models originating from the field of chemistry have also been applied to transport modeling in cQDs, including combinations with DFT simulations.[147]

Further models concerned themselves with ordered cQDs solids. Such models consider transport within superlattice structures composed of periodically arranged, closely packed cQDs. These models have shown that mini bands can form and predicted the possibility of band-like transport.

Andrew Shabaev and Alexei L. Efros[148] developed an analytical model that describes the transport of electrons in cQDs, both in dark conditions and under illumination. This model assumes that the artificial atom-like cQD

2 Fundamentals

creates with its surroundings a periodic potential, enabling a treatment of the superlattice similar to the treatment of electrons in a crystal lattice.

Although the possibility of band like transport in cQDs has been proposed for several decades, it has only been recently achieved.[69, 70, 86, 87] This can be attributed to advancements in synthesis and passivation through ligand exchange methods. Although various models have predicted band like transport, measurements have shown that none of them are ideal to describe the transport properties in such a cQD assembly. It was found that a model used to describe the transport in heterogeneous conductors consisting of weakly coupled metallic islands was best suited to describe the transport in such a strongly coupled cQD system.[70]

In general, experimentally validating models is essential to confirm their accuracy and reliability. In the case of cQD transport models this is often done utilizing temperature-dependent mobility measurements. This method can be used since the underlying physical principles embedded in each model typically show unique temperature dependencies.

From this brief discussion, it is evident that charge transport in cQDs remains a field with many unknowns, necessitating further research. The complexities of cQD behavior under varying conditions underscore the need for comprehensive studies to better understand and predict their properties in practical applications.

2.3 Optical Metamaterials

In this section, an overview of electromagnetic (EM) wave propagation theory with an emphasis on the influence of the material properties is provided. Subsequently, an introduction to optical metamaterials, focusing on perfect absorbers and their interaction with light is given. This section is based on literature [149–152].

2.3.1 Basic EM Wave Propagation Theory

To describe the interactions of light with matter it is essential to adopt a framework that captures the wave-like nature of light and can describe the interactions with matter depending on their material properties. The framework used for this purpose consists of Maxwell's equations. These equations provide a description of how electric and magnetic fields propagate and interact with various media. By coupling these equations, it is possible to derive the Helmholtz equation, which is essential for understanding wave phenomena such as diffraction and interference. The Helmholtz equation for the E-field takes the form

$$\Delta E - k^2 E = 0, \quad (2.55)$$

with Δ the Laplace operator and k the material dependent wavenumber. The solutions to this equation typically take the form of plane waves,

$$E = E_0 e^{i(kz - \omega t)}, \quad (2.56)$$

The material dependence on the propagating wave is included in the wavenumber. This wavenumber at the frequency ω can be expressed using the vacuum and relative permeability and permittivity, ϵ_0 , ϵ_r and μ_0 , μ_r as

$$k = \omega \sqrt{\mu_0 \mu_r \epsilon_0 \epsilon_r} = \frac{\omega}{c_0} \sqrt{\mu_r \epsilon_r} = k_0 \sqrt{\mu_r \epsilon_r} \quad (2.57)$$

In this equation, k_0 represents the vacuum wavenumber, which is the wavenumber observed in a vacuum and is modified by the square root of the material properties. These material properties are collectively termed the refractive index. Thus, the refractive index encapsulates how the vacuum wavenumber is altered when light travels through different materials.

$$\mathbf{n} = \sqrt{\mu_r \epsilon_r} \quad (2.58)$$

For most materials in the optical frequency range the refractive index can be reduced to

2 Fundamentals

$n = \sqrt{\epsilon_r}$ since $\mu_r=1$. As already mentioned in section 2.1.2, the refractive index can be a complex value $\tilde{n} = \mathbf{n} + i\mathbf{k}$, thus can the permittivity also be a complex value.

$$\epsilon_r = \epsilon' + i \epsilon'' \quad (2.59)$$

with

$$\epsilon' = \mathbf{n}^2 - \mathbf{k}^2 \quad (2.60)$$

$$\epsilon'' = 2\mathbf{n}\mathbf{k} \quad (2.61)$$

2.3.2 Metamaterials

Metamaterials are a class of engineered materials composed of elements, often referred to as meta-atoms. These are subwavelength structures that can interact with electromagnetic waves creating a response not present in nature. In contrast to traditional materials, whose properties are dictated by their chemical composition and constituent atoms, metamaterials derive their unique characteristics primarily from their physical shape and arrangement of the sub-wavelength structures. For observations made at length scales larger than the constituent structures of the material, metamaterials behave as a homogeneous effective medium. This allows metamaterials to be described by macroscopic parameters, such as effective refractive index, permittivity and permeability. This effective medium approach is crucial for designing and engineering applications where the material's bulk properties, including its wave-manipulating capabilities, are exploited to achieve functionalities beyond the reach of natural materials.

Further, these macroscopic material properties enable the classification of metamaterials, as depicted in Figure 2.13. The design freedom by metamaterial technology allows for the creation of materials with effective optical properties in every quadrant of the figure. This flexibility includes the design of materials that exhibit a negative refractive index (3rd quadrant Figure 2.13).

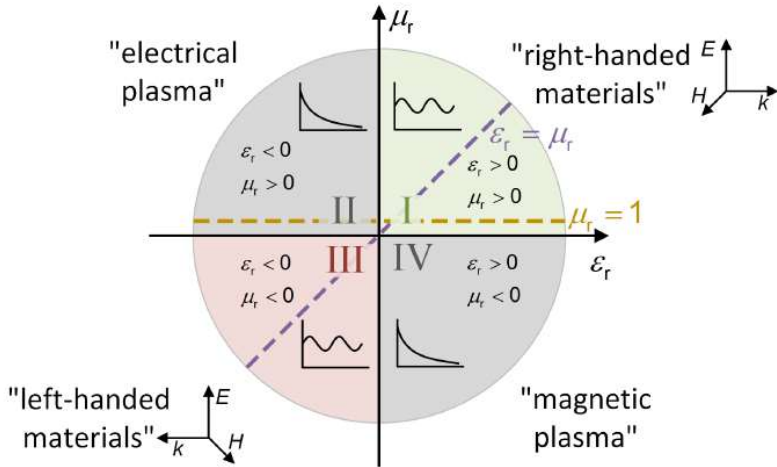


Figure 2.13. Classification of optical materials depending on their permittivity and permeability. The different materials are classified into 4 quadrants accordingly. Furthermore, each quadrant exhibits a graph indicating if waves can propagate or are of an evanescent nature. Taken from [153].

The unique attributes of metamaterials make them suitable for a variety of applications across multiple disciplines. These materials are useful for the development of lenses that operate beyond the sub-diffraction limit, also known as super lenses. Another interesting application of metamaterials is in the area of cloaking. Metamaterials also find applications as highly efficient absorbers in photodetectors as presented in this work.

Metamaterial Perfect Absorbers

In this section, perfect metallic absorbers and their characteristics are discussed. The perfect absorbers which are presented throughout this work are metallic metamaterials consisting of a metal backplane, a dielectric spacer layer, and a top metallic layer comprising of resonating elements. The top layer of such a metamaterial structure can be designed in various ways resulting in different resonances at different wavelengths. In Figure 2.14 different metamaterial designs are shown.

2 Fundamentals

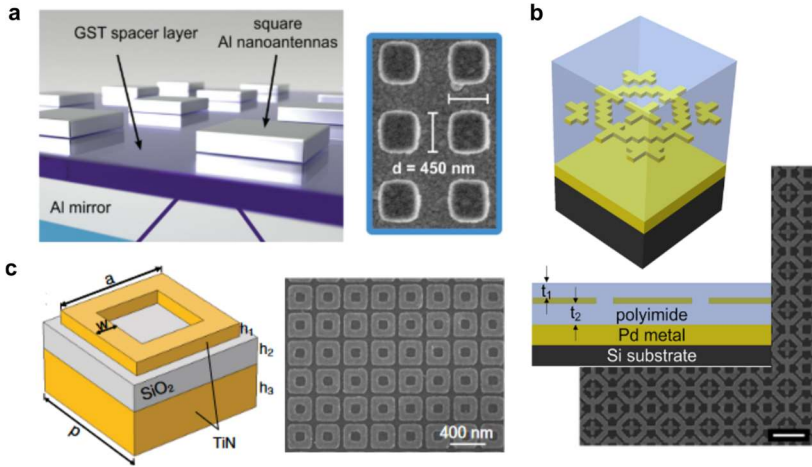


Figure 2.14. Illustration of different metasurface designs. (a) Illustration of a metamaterial consisting of an aluminum backplane/mirror, germanium-antimony-telluride spacer and aluminum square resonators. Including a SEM image of the top element resonators. Reprinted with permission from [154]. Copyright 2015 WILEY-VCH Verlag GmbH & Co. KGaA, Weinheim (b) Shows a schematic depiction and SEM image of a broadband metamaterial perfect absorber created using a genetic algorithm. Reprinted with permission from [155]. Copyright 2014 American Chemical Society. (c) A Schematic representation and SEM image of a titanium nitride metamaterial perfect absorber with a SiO₂ spacer layer. Reprinted with permission from [156]. Copyright 2014 WILEY-VCH Verlag GmbH & Co. KGaA, Weinheim.

An intuitive, high-level way to describe the characteristics of a metamaterial perfect absorber is by analyzing its reflection R , absorption A , and transmission T , with their sum being equal to unity.

$$R + A + T = 1 \quad (2.62)$$

In case of a metamaterials design with a solid metal backplane, as depicted in Figure 2.14, the transmission in the optical regime can be expected to be 0, reducing Eq (2.61) to

$$A = 1 - R \quad (2.63)$$

Reflection of a transverse electromagnetic (TEM) wave at a material interface (e.g. free-space and metamaterial) can be understood through an abstracted fashion by using the concept of wave impedance, similar to reflections in a transmission line.

The wave impedance Z of an electrically non-conducting medium is defined as the ratio of the electric field E_0 amplitude to the magnetic field H_0 amplitude in the direction of wave propagation.

$$Z = \frac{E_0}{H_0} = \sqrt{\frac{\mu}{\epsilon}} \quad (2.64)$$

By using Fresnel's equations and the definition of the wave impedance the reflection at an air metamaterial interface can be expressed as

$$R = \left| \frac{Z_0 - Z_{MM}}{Z_0 + Z_{MM}} \right|^2, \quad (2.65)$$

with Z_0 the free space impedance ($Z_0 \approx 377 \Omega$) and Z_{MM} the wave impedance of the metamaterial, whereas the metamaterial's permittivity and permeability are the effective media values.

In order to maximize the absorption of a metamaterial Eq (2.63) and (2.65) have to be analyzed. From these equations it becomes evident that the free space wave impedance must be equal to the metamaterial impedance in order to reach the maximum absorption. Since the metamaterial impedance can be expressed as

$$Z_{MM} = Z_0 \sqrt{\frac{\mu_r}{\epsilon_r}} = Z_0 \sqrt{\frac{\mu'_r + i \mu''_r}{\epsilon'_r + i \epsilon''_r}} \quad (2.66)$$

it follows,

$$\mu'_r = \epsilon'_r, \quad (2.67)$$

and

$$\mu''_r = \epsilon''_r, \quad (2.68)$$

Since the effective optical parameters of metamaterials can be tuned by their geometric design, it is possible to adjust the absorption properties, enabling designs that operate at different wavelengths with specific characteristics. This highlights one of the biggest advantages of metamaterials, their absorption tunability over a broad wavelength range. The lower limit of absorption is mainly limited by the fabrication limits of the resonating elements feature sizes.

3 Sintered PbSe/PbS Photodetector

Highly Responsive Mid-Infrared Metamaterial Enhanced Heterostructure Photodetector Formed out of Sintered PbSe/PbS Colloidal Quantum Dots*

Raphael Schwanninger, Stefan M. Koepfli, Olesya Yarema, Alexander Dorodnyy, Maksym Yarema, Annina Moser, Shadi Nashashibi, Yuriy Fedoryshyn, Vanessa Wood, Juerg Leuthold

ACS Applied Materials and Interfaces, vol. 15, no. 8, pp. 10847–10857, 2023

Abstract

Efficient and simple-to-fabricate light detectors in the mid infrared (MIR) spectral range are of great importance for various applications in existing and emerging technologies. Here, we demonstrate compact and efficient photodetectors operating at room temperature in a wavelength range of 2710–4250 nm with responsivities as high as 375 and 4 A/W. Key to the high performance is the combination of a sintered colloidal quantum dot (cQD) lead selenide (PbSe) and lead sulfide (PbS) heterojunction photoconductor with a metallic metasurface perfect absorber. The combination of this photoconductor stack with the metallic metasurface perfect absorber provides an overall ~20-fold increase of the responsivity compared against reference sintered PbSe photoconductors. More precisely, the introduction of a PbSe/PbS heterojunction increases the responsivity by a factor of ~2 and the metallic metasurface enhances the responsivity by an order of magnitude. The metasurface not only enhances the light–matter interaction but also acts as an electrode to the detector. Furthermore, fabrication of our devices relies on simple and inexpensive methods. This is in contrast to most of the currently available (state-of-the-art) MIR photodetectors that rely on

*This chapter has been published in [J 2]. Copyright The Authors. Published by American Chemical Society. Figures, tables and notation were adapted for consistency throughout the thesis.

3 Sintered PbSe/PbS Photodetector

rather expensive as well as nontrivial fabrication technologies that often require cooling for efficient operation.

Keywords

Photodetectors, metamaterial, mid-infrared, quantum dots, heterostructure, PbS, PbSe

3.1 Introduction

The mid infrared (MIR) electromagnetic spectrum is a wavelength range which is of great importance for various applications and technologies. These applications include gas sensing[157, 158], thermal imaging[159], biosensing[160], medical imaging[161], spectroscopy, and environmental monitoring[162]. A key component to make such technologies practical are photodetectors. Thus, the demand for cost-efficient highly responsive detectors operating at room temperature increases steadily. Most of the currently available detectors are based on quantum well structures, III-V compound semiconductors, or mercury-cadmium-telluride alloys such as InSb, $\text{In}_{1-x}\text{Ga}_x\text{As}$ and $\text{Hg}_{1-x}\text{Cd}_x\text{Te}$ [19, 100]. However, detectors fabricated from these materials are quite expensive, require complex fabrication processes, and often need cooling, thus limiting their use for various applications.

Alternatively, lead chalcogenides have been used since the 1950s for MIR photodetection and have recently re-emerged due to their high MIR sensitivity and low cost. [19, 101] PbSe is particularly promising and is one of the most used materials for photodetection in the MIR spectrum due to its low cost and high detectivity at room temperature.[101] Although PbSe has been used for photodetection for several decades, a full understanding of the photoconduction mechanism is still lacking. Pristine PbSe shows no significant photoresponse in the MIR. However, with a thermal treatment in an oxygen and iodine atmosphere – referred to as sensitization – MIR detection becomes possible. [57, 102, 103] Furthermore, the performance of PbSe detectors depends on which deposition method is used, with the primarily used methods being chemical bath deposition (CBD) and chemical vapor deposition (CVD), which have both their benefits and drawbacks. [101] CBD is a cheap process where PbSe is grown on a substrate in solution. This deposition technique has the disadvantage that it is challenging to reproduce, it is difficult to achieve thin uniform layers over a large area, and it is limited in that it is substrate dependent.[101] Contrary to CBD, CVD enables the deposition over large areas, but the material typically exhibits worse photoconduction than CBD-grown PbSe.[101] An attractive alternative to polycrystalline PbSe are colloidal quantum dots (cQDs). They are substrate independent, absorption tunable, and can be deposited from solution, which makes them a promising candidate for cost-efficient photodetectors; [28, 122, 163, 164] however, so far, they display low quantum efficiency in the MIR.

3 Sintered PbSe/PbS Photodetector

In recent years, considerable effort has been put into researching strategies to enhance the photoresponse of detectors based on bulk, two-dimensional (2D), and cQD materials. One way to enhance the absorption and therefore the photoresponse are metamaterials. Such artificial materials consist of periodically-arranged, subwavelength structures, which can resonantly couple to incoming electromagnetic (EM) fields. These resonating elements can scatter the EM field into photoactive materials and enhance the photoresponse.[165, 166] Metamaterials can be designed with numerous different material stacks and geometries depending on the desired characteristics such as a narrow or broad band absorption and on the wavelength regime for which they are intended. [165] And indeed, metamaterials have been repeatedly used to enhance the absorption of photodetectors, but most designs do not take the charge extraction into account. Photogenerated carriers often must travel large distances to the electrodes and charges recombine before they can be collected, which reduces the photoresponse.

An additional way of increasing the photoresponse is by combining different materials in a heterojunction configuration. Such stacks have been realized by combining 2D, bulk, or cQD materials in a planar or vertical fashion. [167, 168] In planar heterojunction configurations, the layers can be arranged to provide photogain. In heterojunctions, electrons and holes are spatially separated at the interface of different materials due to a built-in electric field and one type of charge carrier is transported to electrodes whereas the other is trapped. The trapping of one type of carrier and the transport of the other to the electrodes can result in gain if the trapping lifetime is longer than the transient time.[167] Such schemes have also been used in photodetectors based on organic materials where the gain resulting from charge trapping is often referred to as photomultiplication.[169, 170] Further, the spatial separation of carriers can result in reduced charge recombination.[167] Although heterojunctions can enhance the detector performance, they also have drawbacks. Most heterojunction photodetectors are implemented in a vertical configuration, thus transparent electrodes are required, which can be challenging and restricting due to the small number of suited materials. Additionally bulk heterojunctions are often deposited via molecular beam epitaxy, which makes them expensive. Whereas heterojunctions employing 2D materials seem promising, the large area deposition of these materials is still difficult.[171]

In this work, we overcame low photoresponse, expensive and complicated absorber material deposition, and the necessity for low-temperature operation by combining a metamaterial perfect absorber, a heterojunction, and a sintered cQD absorbing layer into one device to demonstrate a highly responsive, simple to fabricate, and compact MIR photoconductor operating at room temperature. We found responsivities as high as 375 A/W at 2712 nm and 4.8 A/W at 4250 nm. The absorber material was fabricated out of NIR absorbing PbSe cQDs, which were surface modified and thermally treated to form a MIR absorbing polycrystalline layer, without the need of sensitization. This deposition method has the possibility of being cost efficient and allows [28, 122, 163, 164] for large area deposition of thin uniform layers with good thickness controllability due to solution processability. In addition, the developed recipe allows for stacking of different materials. This way we can deposit and crystallize a thin PbS layer on top of the crystallized PbSe layer, forming a beneficial heterojunction. The PbSe/PbS layers were finally combined with a metasurface to selectively enhance the absorption in a wavelength range from 2.7 to 4.2 μm . This metasurface was designed in such a way that it allows both absorption enhancement and charge extraction.

3 Sintered PbSe/PbS Photodetector

3.2 Device Structure and Fabrication

We developed efficient MIR photoconductors by combining a metasurface with a heterostructure PbSe/PbS absorber stack (Figure 3.1). The metasurface consists of a metal–insulator–metal stack designed to integrate dipole resonators with an interdigitated electrode structure, which contacts the photoconducting lead chalcogenide layers. Consequently, the generated in-plane dipole field can be efficiently absorbed by the PbSe and only a very thin absorber layer is needed to fabricate highly responsive photodetectors.

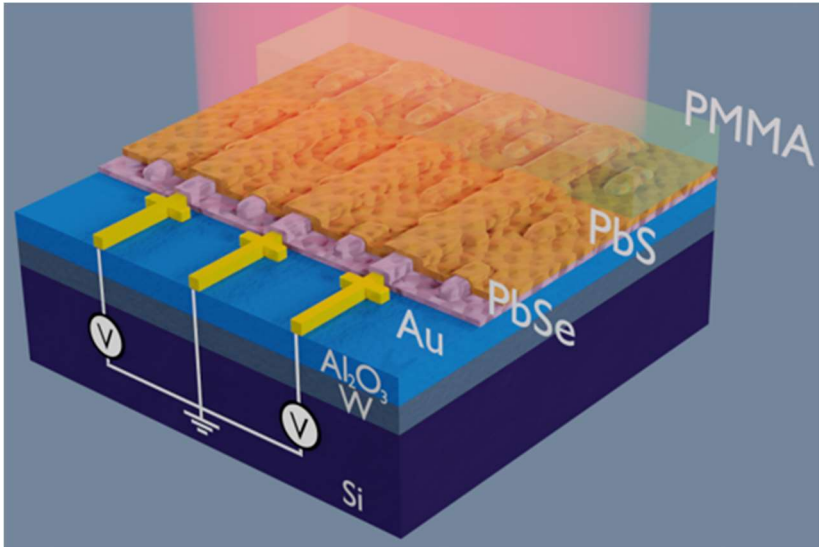


Figure 3.1. Schematic illustration of metamaterial enhanced heterojunction photodetector with top illumination. The 100 nm tungsten (W), 100 nm alumina (Al_2O_3) and 70 nm thick gold (Au) layer form the metasurface which is used to enhance the absorption and contact the photoconducting heterojunction layer (30 nm PbSe/25nm PbS). The width of the contact lines and the dipole resonators was 80 nm. The 120 nm PMMA layer is used for passivation.

To fabricate the envisioned heterojunction metamaterial enhanced photodetectors, we first optimized the sintered colloidal cQDs layers. We then fabricated MIR photodetectors, built from these optimized sintered cQDs layers, and demonstrate their excellent characteristics stemming from the planar PbS/PbSe heterojunction; finally, this layer stack was combined with a metamaterials stack and characterized.

3.2.1 Optimizing the Deposition and Crystallization of cQD Lead Chalcogenide Absorber Layers

The developed deposition recipe offers various advantages compared to conventional lead chalcogenide deposition methods. It is simple, can be applied to various substrates, it is CMOS, low cost, and results in uniform layers with a surface roughness as low as 3–4 nm. The deposition method is CMOS compatible in the sense that the deposition technique of the cQDs, the used chemicals, and applied annealing temperatures are compatible with standard materials and fabrication processes used for CMOS technology.[166, 172] Furthermore, the low costs arise from the fact that there is no need for expensive and sophisticated deposition infrastructure compared to CVD, making this deposition method attractive for low-cost fabrication and high throughput.[28, 122, 163, 164]

PbSe and PbS cQDs were selected as absorber materials. The synthesis of these colloids is well-studied and yields high-quality monodisperse cQDs. Lead chalcogenide cQDs have been successfully employed in the visible and NIR spectral ranges, but devices operating in the MIR have been scarcely reported and often perform worse than their bulk counterparts.[56, 173–176] In order to combine the deposition advantages of cQDs and the performance of bulk materials, we have developed a liquid-phase spin-coating fabrication recipe, followed by a solid-state surface modification of cQDs (i.e., ligand exchange) and thin-film annealing step. The latter triggers microscale sintering of cQDs layers, enabling bulk-like transport and extended absorption to the MIR.

More precisely, the PbSe cQDs in octane were spin-coated on Si substrate with a native oxide on top. After the deposition, the nonvolatile oleic acid ligands were exchanged for short and more volatile ethanedithiol (EDT) molecules. Afterward, the substrate with the cQD thin film was placed on a hot plate at 130 °C for 1 min to evaporate the excess solvents and EDT ligands. This deposition cycle was repeated until the desired thickness of the cQD layer was reached. Finally, the whole stack was annealed at 310 °C to sinter the cQDs and form a bulk-like polycrystalline layer. Then, PbS cQDs were either deposited onto Si substrates or on a previously annealed PbSe cQD layer, followed by the same spin-coating, ligand-exchange, and annealing procedure as for the PbSe cQDs. Figure 3.2a provides a schematic of the deposition and annealing process. A detailed description of the synthesis of the used PbSe and PbS cQDs with diameters of 4 and 8 nm is given in the Supporting Information Section 3.6.1.

3 Sintered PbSe/PbS Photodetector

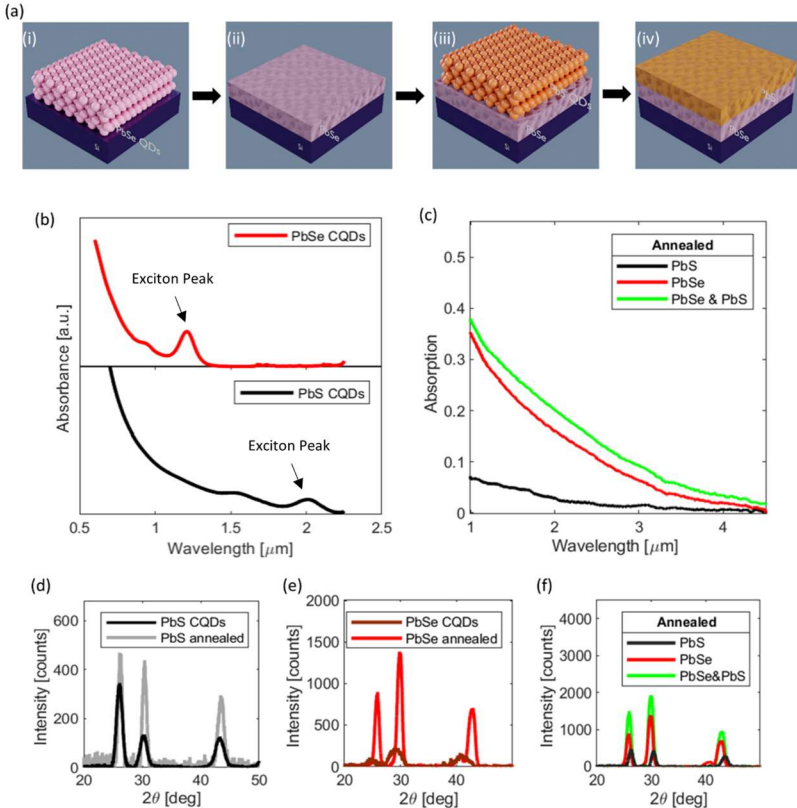


Figure 3.2. (a) Schematic of the fabrication of the annealed PbSe/PbS bilayer stack layers as used for the GIXRD characterization. (i) Solution deposited PbSe cQDs on Si substrate after annealing, at 130 °C for 1 min. (ii) Sintered PbSe layer after elevated temperature annealing at 310 °C for 1 min. (iii) Solution deposited PbS cQDs on the sintered PbSe cQD layer. (iv) Sintered PbSe/PbS bilayer stack after second elevated temperature annealing, 310 °C for 1 min. (b) UV-vis absorbance spectra, in arbitrary units, of cQDs in solution, showing absorbance peaks resulting from the quantum confinement and no absorbance for wavelengths larger than 2 μm . This plot shows the general shape of the absorption curve of the cQDs in solution and is not an absolute measure. (c) FTIR absorption spectra of the annealed PbSe and PbS cQD and of the stacked and annealed PbSe/PbS layers on sapphire substrates. The annealing results in the sintering of the individual cQDs into larger crystal domains, which results in the loss of excitonic peaks. The spectrum now approaches a bulk spectrum with absorption up to the MIR. (d and e) XRD patterns of cQDs and annealed layers. (f) XRD pattern of annealed PbSe, PbS, and stacked PbSe/PbS layer.

The absorption spectra of the pristine cQDs in solution have a distinct exciton peak at a wavelength of 1200 nm for PbSe and 2010 nm for PbS and no absorption beyond these wavelengths (Figure 3.2b). The local exciton absorption peak and the lack of an absorption beyond 1200 and 2010 nm, compared to the bulk materials, which absorb further in the MIR, are clear indicators that electron and hole confinement is present before the annealing. The excitonic peaks and the blue-shifted absorption spectra occur when bound electron–hole pairs (exciton) are confined to a space smaller than their exciton radius. The confinement leads to discretization of the quasi-continuous valence and conduction bands. Thus, the absorption spectra can be used to verify if the colloidal quantum dots sinter into larger crystal domains and lose their confinement.[138, 177, 178]

When the cQD layers are annealed, they sinter into larger crystal domains and the absorption becomes more bulk like. The electron and hole pairs are now located in a space larger than their exciton radius; as a result, no discrete energy states larger than the bulk band gap of PbS and PbSe are present. As a consequence, the absorption extends after the annealing and sintering to the MIR. Figure 3.2c shows the absorption spectra of the annealed thin films, it can be seen that the exciton peaks due to the quantum confined have disappeared and the sintered layers absorb in the MIR. Furthermore, the measurements show the PbSe layers to be stronger absorbing than the PbS layers. This is similar to what can also be seen from bulk PbSe and PbS.[179] The deposited PbSe layer was ~30 nm, and the PbS layer was ~25 nm thick. The thickness of these layer was acquired with atomic force microscopy (AFM) measurements; details can be found in the Experimental Methods section.

We additionally did grazing incidence X-ray diffraction (GIXRD) characterizations to observe the changes of the crystallinity upon annealing. Parts d and e of Figure 3.2 show the GIXRD plots of the PbS and PbSe cQDs before and after the annealing step. It is clearly visible that the peaks become narrower and more pronounced after annealing at 310 °C, which indicates the sintering of cQDs into larger crystal domains. GIXRD characterizations at various annealing times revealed interesting trends: While the crystallinity of PbSe cQD thin film decreases with increasing annealing time, the PbS layer shows the opposite trend (Figure 3.8a,b. These trends were determined since the intensity of the characteristic peaks of PbS in the XRD pattern increased with the annealing time and the intensity of the PbSe peak decreased. In addition to GIXRD, we characterized the cQD

3 Sintered PbSe/PbS Photodetector

thin films using AFM, which shows that the cQD layers crystallize upon annealing into grains of 30–50 nm (Figure 3.9).

We performed additional GIXRD measurements with single layer PbS and PbSe and with the annealed PbSe/PbS stack to show that the annealed PbSe/PbS bilayer remains a stack of two different materials and does not form a homogeneous ternary $\text{PbS}_x\text{Se}_{1-x}$ compound (see Figure 3.2f). The shape of the two single materials PbS (black) and PbSe (red) sum up to the pattern of the stacked PbSe and PbS material (green), indicating that the materials do not form a single compound. A more detailed plot showing this can be found in Figure 3.8c. In Figure 3.8c in the Supporting Information Section 3.6.2, it can be seen that the slight offset between the PbS and PbSe peak position translates to a minor asymmetry of the intensity peaks of the stacked PbSe/PbS XRD pattern.

3.2.2 PbSe/PbS Heterojunction Photoconductors

After the development of the deposition and annealing recipes, we carried out an electro-optical characterization of the sintered cQDs to investigate their MIR photoresponse and show the advantages of the heterojunction, which resulted in ~ 2 -fold increase of the photoresponse compared to pristine PbSe at a wavelength of 2710 nm. The increased photoresponse of the bilayer devices is a result of trap assisted gain, which is discussed in more detail below.

To characterize the sintered cQDs, we fabricated simple photoconductor structures consisting of an Au interdigitated finger structure on top of a Si substrate with a thermally grown SiO_2 layer. The characterized photoconductor materials are the annealed PbSe/PbS stack and for referencing the pristine PbSe and PbS. The PbSe photoconductor was furthermore annealed twice in order to guarantee that it undergoes the same number of annealing steps as the PbSe/PbS stack. After the deposition of the photoactive materials, a PMMA layer was deposited on top to prevent oxidation. Each of the deposited layers was 25–30 nm thick; consequently, the PbSe/PbS stack was 50–60 nm thick. A schematic cross section of such a device with a PbSe and PbS layer can be seen in Figure 3.3a, and detailed description of the device geometry can be found in the Experimental Methods section. The photoconductors were characterized at a wavelength of 2710 nm in a custom-built setup (Figure 3.10).

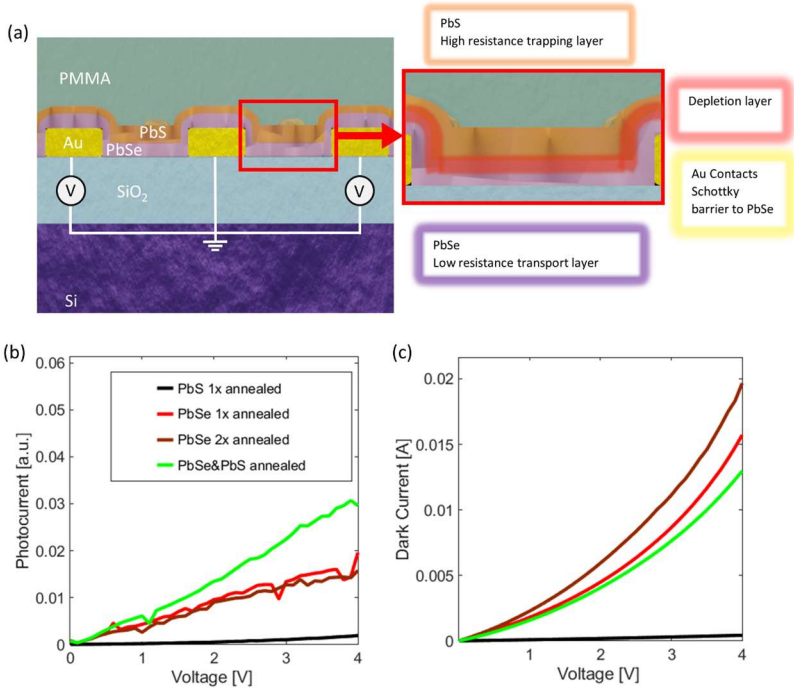


Figure 3.3. (a) Schematic cross-section of bilayer photodetector with zoom-in and function description. The photodetector consists of gold (Au) interdigitated electrodes on top of a silicon (Si) substrate with a thermally grown silicon oxide (SiO_2) and a PbSe/PbS heterojunction photoconducting layer which is passivated by a PMMA layer. The Zoom-in shows the PbSe layer, which forms a Schottky type contact to the Au electrodes and is responsible for the main absorption and current transport. The high resistance PbS layer forms a heterojunction with the crystal grains of the PbSe layer. A depletion layer is formed in-between (red layer). (b) Voltage dependent photocurrent of the photodetectors with annealed photoconducting layers under identical illumination conditions at a wavelength of 2710 nm. The PbSe layers (red, brown) show a ~ 10 times greater response than PbS (black). The implementation of the heterojunction leads to a further ~ 2 -fold increase of the response (green). (c) Dark current of the photodetectors with annealed photoconducting layers. Illustrating the larger conductivity of the PbSe layers (red, brown, green) compared to the PbS layer (black).

Figure 3.3b shows the resulting photocurrent (under identical illumination conditions) of the different photoconductor materials and their combination. PbS exhibits the lowest photoresponse, whereas the once and

3 Sintered PbSe/PbS Photodetector

twice annealed PbSe layers display a ~ 10 -fold increase in photocurrent. The difference of the photoresponse can be attributed to the properties of the materials, because PbS is absorbing less light than PbSe, as shown in Figure 3.2c. Furthermore, the conductivity of the PbS layer is lower than for the PbSe, which results in lower currents, as shown in Figure 3.3c. The lower conductivity of PbS may be partially the result of a lower electron and hole mobility μ_e and μ_h . A lower electron and hole mobility of PbS have been reported in the literature ($\mu_e \sim 600 \text{ cm}^2 \text{ V}^{-1} \text{ s}^{-1}$ and $\mu_h \sim 700 \text{ cm}^2 \text{ V}^{-1} \text{ s}^{-1}$) when compared to those of PbSe ($\mu_e \sim 1200 \text{ cm}^2 \text{ V}^{-1} \text{ s}^{-1}$ and $\mu_h \sim 1000 \text{ cm}^2 \text{ V}^{-1} \text{ s}^{-1}$). [180, 181] Also, due to the lower mobility, it is expected that less photogenerated carriers can be extracted before they recombine resulting in a lower photoresponse.

We want to point out that the deposited PbSe was not sensitized and is still photoconducting in the MIR wavelength regime. A discussion on the photoresponse of the annealed PbSe cQDs can be found in the Supporting Information Section 3.6.5.

The benefit of implementing a bilayer stack can be seen by the ~ 2 -fold increase of the photocurrent compared to single layer PbSe devices (see Figure 3.3b). Notably, the photocurrent is larger than the sum of contributions of the individual materials on their own. This increase of the photocurrent is attributed to photogain obtained by the PbSe/PbS heterojunction.

The origin of the observed photogain can be understood as follows: Photons are primarily absorbed in PbSe, creating free electrons and holes. These carriers are then separated by the built-in field of the PbSe/PbS heterostructure interface. We assume that photogenerated electrons in the PbSe layer are transported to the PbSe/PbS interface where they are trapped, whereas holes are transported to the Au electrodes as a result of the externally applied electric field between the gold electrodes. The assumption of the separation of the photogenerated carriers is based on the bulk conduction and valence band structure resulting from the electron affinities χ and band gaps E_g of PbSe and PbS ($\chi_{\text{PbSe, bulk}} \approx 4.7 \text{ eV}$, $E_{g, \text{PbSe}} \approx 0.27 \text{ eV}$, $\chi_{\text{PbS, bulk}} \approx 4.55 \text{ eV}$, $E_{g, \text{PbS}} \approx 0.4 \text{ eV}$). [181–184] Further, EDT treatment of PbSe and PbS is known to result in p-type cQD layers. [185, 186] It is therefore assumed that the annealed colloidal QDs still exhibit p-type behavior after the annealing.

Similar trapping schemes have been applied with various different photoactive materials and device structures. [185, 187–190] If the trapping

lifetime t_{lifetime} of the photogenerated electrons is larger than the transient time t_{transit} of the holes to the electrode, gain occurs since the charge neutrality condition must apply. The theoretical gain G_{th} of a photoconductor can thus be defined as $G_{\text{th}} = t_{\text{lifetime}}/t_{\text{transit}}$. It is desirable that the charge transport layer has a high mobility since the transit time can be expressed as $t_{\text{transit}} = L^2/\mu V$. Therefore, the mobility can directly influence the gain and with it the photoresponse.[167, 191–193] The absorber stack and the properties of each material can be seen in the zoom-in of Figure 3.3a.

The formation of a heterostructure is thus important for obtaining photogain. Various accounts on the increase of responsivities due to the presence of a heterojunction have already been given for such planar configurations.[185, 194–197] Indication for the presence of a heterojunction between the PbSe and PbS can be derived from Figure 3.3c. The figure shows the dark current between the Au electrodes for a PbSe layer stack (brown and red). When the dark current is measured for the combined layer stack of PbSe/PbS, one finds a lower dark current. This can be explained by the built-in field that is formed at the interface due to carrier depletion. This depletion layer reduces the cross-section through which the current is flowing along the lateral direction, therefore increasing the overall resistance, which leads to the lower current. A further discussion on the formation of the heterostructure can be found in the Supporting Information Section 3.6.6.

3.2.3 Passive Characterization of PbSe/PbS Metamaterial Photodetectors

Lastly, the MIR photosensitive bilayer stack was combined with a metallic metamaterial to selectively increase the absorption. The metamaterial consists out of a metal–insulator–metal stack and does not exhibit any photoresponse without the photoactive PbSe/PbS layer. With the addition of the metamaterial, near unity absorption has been achieved. A scanning electron micrograph and the schematic of the fabricated metamaterial are shown in Figure 3.4a,b. This structure was covered with the 30 nm PbSe and 25 nm thick PbS bilayer stack. Finally, a 120 nm thick PMMA layer was spin-coated as passivation (see Figure 3.1).

3 Sintered PbSe/PbS Photodetector

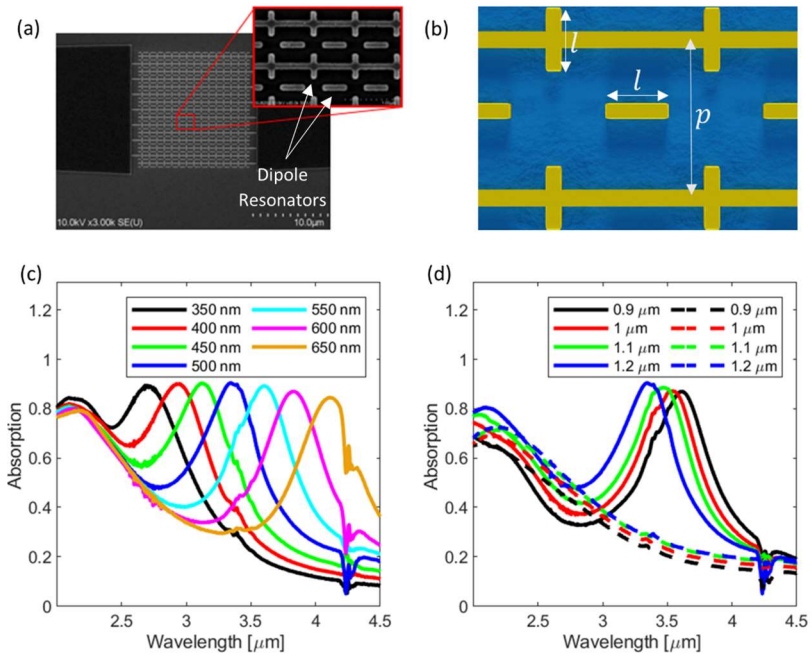


Figure 3.4. (a) SEM image of the metamaterial design showing the Au top layer with the freestanding and interconnected resonating elements. (b) Top view of the designed metamaterial with the contact lines and dipole resonators including the design parameters. (c) Passive absorption spectra of metamaterial detector. The resonator lengths l were varied and the period was kept constant at $p = 1.2 \mu\text{m}$. The absorption peaks shift toward larger wavelengths when increasing the dipole resonator length l . (d) Passive absorption spectra of metamaterial detectors. Here, the periods p was varied but the resonator length was kept at $l = 500 \text{ nm}$. A blue shift of the resonance peak with increasing period can be observed. The dashed lines show the absorption spectra of devices without any dipole resonators as a reference.

The metamaterial layer stack consists of a tungsten backplane, an alumina spacer layer, and the gold resonator layer. The resonators are constructed of dipole antennas that are partially interconnected with contact lines. These dipoles act like a deconstructed cross resonator metamaterial perfect absorber and couple to different polarization states of incoming light.[166, 198, 199]. A SEM image with indications of the dipole

resonators as well as a partial schematic of the metamaterial can be found in Figure 3.4a,b. The resonance is hardly perturbed by the connection line and the metamaterial generates an in-plane dipole field that can be efficiently absorbed by an absorbing layer placed on top. A detailed discussion on the shown metamaterial can be found in a previously published work.[J 6]

The narrow absorption peaks resulting from the metamaterial can be shifted across a wide wavelength range by changing the dimensions of the metasurface. The parameters used to tune the absorption peak position are the length l of the resonators and the period p of the square unit cell shown in Figure 3.4b. When the resonator length is increased the absorption peak is shifted to longer wavelengths, whereas the peaks are shifted to shorter wavelength by increasing the period between the contact lines, which is shown by the measured plots in Figure 3.4c,d. With the selected design parameters, an absorption for unpolarized light of approximately 90% could be reached. Further, the absorption is nearly polarization independent due to different orientation of the dipole antennas and does not drop below 75% while reaching 98% for an ideal polarization state (see Figure 3.13). This indicates that nearly perfect absorption could be achieved by slightly correcting the length of the dipoles.

This metamaterial design offers an additional feature since two parameters can be used to tune the absorption peak position. It is possible to tune the photocarrier extraction efficiency without changing the absorption spectra by reducing the period between the contacts and at the same time reducing the resonator length.

3 Sintered PbSe/PbS Photodetector

3.3 Results

Followed by the passive absorption characterization, metamaterial devices were selected with absorption peaks at wavelengths of 2730, 3250, 4000, and 4250 nm and electro-optically characterized at these wavelengths. The passive absorption spectra of the selected devices are shown in Figure 3.14. Furthermore, the geometry data of the metamaterial designs can be found in Table 3.1 of the Supporting Information. Subsequently, the electro-optical characterizations were carried out with either a laser source at 2710 nm or a blackbody light source, which was filtered by bandpass filters. The photoresponse and the noise characterizations were performed with a lock-in-amplifier. All of the results have been obtained for a device with an absorption peak at a wavelength 2730 nm— unless for Figure 3.6, where device with absorption peaks close to the used characterization wavelengths are compared. Additional measurements and an illustration of the measurement setup can be found in the Supporting Information Sections 3.6.4 and 3.6.9.

In Figure 3.5a, the voltage dependent responsivity of a metamaterial photoconductor and a photoconductor without any dipole resonator (see Figure 3.4a for indication of the dipole resonators), referred to as reference, is shown. Such reference devices were fabricated on the same chip as the metamaterial photoconductors. They consist of 70 nm thick and 80 nm wide Au contact lines spaced with the period p , which are covered by the photoactive PbSe/PbS heterojunction and a PMMA layer. The reference devices and the metamaterial devices had the same active area of $30 \times 30 \mu\text{m}^2$. The metamaterial detector exhibits a ~ 2 -fold increase in responsivity at a wavelength of 2710 nm compared to the reference detector. This comparison clearly demonstrates the absorption enhancement due to the metamaterial.

Frequency response measurements in the range from 4 Hz to 10 kHz have been performed (see Figure 3.5b). The frequency range was limited by the mechanical chopper used to modulate the light source. A maximum response of $\sim 250 \text{ A/W}$ was found at a frequency of 4 Hz. It can be seen from the trend of the responsivity that the responsivity could be higher if measured at frequencies lower than 4 Hz. The maximum responsivity was found by measuring the steady-state photoresponse, (Figure 3.5c) and scaling it with the measured responsivities from Figure 3.5b. A maximum responsivity of $\sim 375 \text{ A/W}$ was found (details on the measurement are given in the Supporting Information Section 3.6.7). Figure 3.5c was also used to

extract the rise and fall times of $\tau_{\text{rise}} = 4.27$ s and $\tau_{\text{fall}} = 5.25$ s. These long time constants can be often observed in cQD based devices and are attributed to long-lived traps. [58, 176, 200] A comparison of recently published works and this work with respect to the responsivity can be found in the Supporting Information Section 3.6.10.

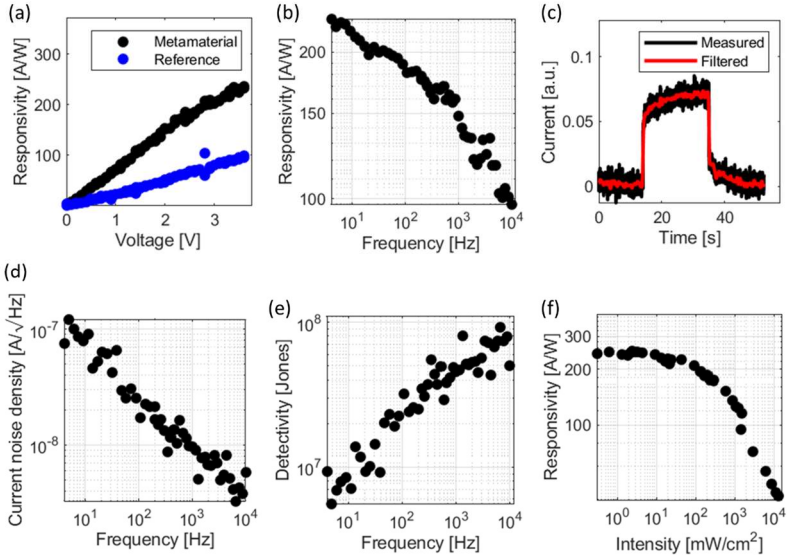


Figure 3.5. Electro-optical characterization of the detector. (a) Voltage dependent responsivity at 4 Hz modulation frequency of a metamaterial and comparison with an identical reference device without dipole resonators. The metamaterial device clearly outperforms the reference device. (b) Frequency dependent responsivity, 4 Hz–10 kHz. (c) Photoresponse measured over a long period of time. (d) Current noise spectral density. (e) Frequency dependent detectivity. (f) Intensity dependent responsivity (All measurements were performed on a metamaterial enhanced PbSe/PbS heterojunction photodetector with a resonator length of $l = 350$ nm and a contact spacing of $p = 1$ μm). The reference device had no resonating elements and a contact spacing of $p = 1$ μm . The measurements under illumination were carried out at a wavelength of 2710 nm.

While carrier traps can lead to increased responsivity, the trapping and detrapping process also leads to an increase of the current noise. [29, 201, 202] We expect this effect to be the origin of the large noise currents (see Figure 3.5d). Due to this large noise current, the specific detectivity is limited to $\sim 1 \times 10^8$ Jones, as shown in Figure 3.5e. The maximum detectivity is found for higher modulation frequencies despite of the responsivity decreasing

3 Sintered PbSe/PbS Photodetector

with frequency. This can be understood by the fact that the noise current decreases with frequency at a larger scale, a finding often observed for PbSe based detectors. [173]

The metamaterial detector was finally characterized with respect to the incoming light intensity. It can be seen in Figure 3.5f that the detector operates over a large intensity regime.

To show the benefits of the metamaterial, the fabricated detectors were compared to reference devices. The reference devices consist of an interdigitated finger structure spaced with the same pitch p as the metasurface but without any dipole resonators. The ratio between the responsivities of the metamaterial and the reference detectors was used as a figure of merit and is referred to as enhancement. The enhancement for different detectors at different wavelengths is shown in Figure 3.6a. From this plot, it can be seen that the enhancement increases with wavelength. This can be understood as follows. The absorption is already quite good for shorter wavelengths (see Figure 3.2c). And indeed, the responsivity is quite large for shorter wavelengths as can also be seen from Figure 3.6b. Therefore, there is little to be won from the metamaterial enhancement. Yet, the enhancement is more efficient at longer wavelength, where the absorption is smaller, and a resonant enhancement effectively provides a longer interaction with the absorber and therefore an enhancement for the overall absorption.

The enhancement increase for larger wavelengths can also be seen when comparing the absorption spectra of the metamaterials with the corresponding reference device absorption (Figure 3.4c,d).

In Figure 3.6b, the frequency dependent responsivity is shown for the different metamaterial devices and wavelengths. The overall decrease of the responsivity with increasing frequency is present for all devices and independent of the metamaterial geometry and can therefore be attributed to the material properties of the photoconductors. Furthermore, in Figure 3.6c, the detectivity is shown. As expected, it scales in the same manner as the responsivity. The responsivity could be additionally used to estimate the external quantum efficiency (EQE) according to the relation $EQE = R(\lambda) \frac{hc}{q\lambda}$.

[191]

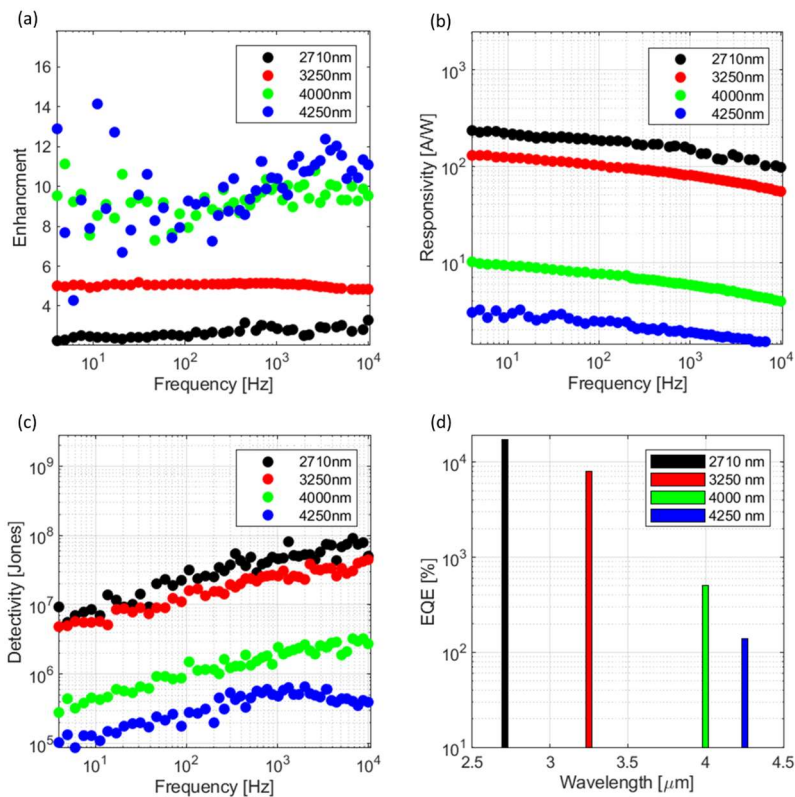


Figure 3.6. (a) Enhancement (ratio of responsivity of a metamaterial enhanced photodetector against a reference photodetector without resonating elements) vs frequency for different metamaterial photodetectors characterized at different wavelengths. An increase of the enhancement with the wavelength can be observed. (b) Responsivity vs frequency for different metamaterial detectors characterized at different wavelengths. (c) Detectivity of different metamaterial detectors measured characterized at different wavelengths. (d) EQE of four different metamaterial detectors characterized at four different wavelengths. The maximum responsivity was assumed.

3 Sintered PbSe/PbS Photodetector

3.4 Conclusion

In conclusion, we presented a metamaterial enhanced MIR photoconductor operating at room temperature with responsivities as high as 375 A/W at a wavelength of 2710 nm and 4.8 A/W at 4250 nm. These values have been reached by systematically enhancing the device performance by implementing a PbSe/PbS heterojunction absorber stack with a metasurface absorption enhancement scheme. The absorber stack has been fabricated out of NIR absorbing cQDs, which were deposited from solution and then annealed into a polycrystalline like layers. With this method, it is possible to combine the simple and cost-efficient deposition of cQDs, such as spin-coating, with superior bulk MIR absorption properties of lead chalcogenides.

We have shown that the developed deposition method can be used to fabricate MIR photoconducting PbSe layers without the need of sensitization, which is a necessary step for CBD or CVD PbSe to show a relevant MIR photoresponse. Furthermore, the dark current could be decreased and the photoresponse increased ~ 2 -fold by realizing a PbSe/PbS bilayer stack, which forms a heterojunction on a crystal grain basis, compared to a single layer PbSe device. This bilayer stack was last combined with a metallic metasurface perfect absorber. The chosen metamaterial design allowed to selectively enhance the spectral absorption of the detectors ranging from 2.7 to 4.2 μm . An overall responsivity increases by up to a factor ~ 20 has been achieved, demonstrating the benefit of the enhancement schemes. The combination of the developed deposition recipe and the metasurface has the potential to satisfy the growing demand for highly responsive MIR photodetectors fabricated by cheap and simple means.

3.5 Experimental Methods

3.5.1 cQD Synthesis

Information on the cQD synthesis and transmission electron microscopy can be found in the Supporting Information Section 3.6.1.

3.5.2 cQD Deposition and Annealing

All the following deposition and annealing steps were carried out in an N₂ atmosphere. The in hexane dispersed cQDs were purified by three cycles of precipitation and redispersion by using centrifugation and anhydrous acetone/hexane as nonsolvent/solvent. After the third purification cycle, the cQDs were dissolved in anhydrous octane, PbSe at a concentration of 12 mg/mL, and PbS at a concentration of 22 mg/mL. The cQDs were spin-coated in a layer-by-layer fashion. cQDs solution was dropped onto the substrate of choice and spun at 2000 rpm for 30 s; then, they were soaked in a 1 vol % EDT acetonitrile solution to achieve a ligand exchange, followed by three rinsing steps. The cQDs were annealed after each spin-coating cycle at 130 °C for 1 min. After the cQD deposition, the cQDs were annealed for 1 min at 310 °C. The bilayers were achieved by depositing the PbS on top of an annealed PbSe followed by the identical annealing procedure as described. This deposition resulted in 25–30 nm thick layers for both PbS and PbSe.

3.5.3 XRD Characterization

The absorber materials were deposited on Si substrates, after which they were placed in a Rigaku SmartLab 9KW XRD-diffractometer for characterization.

3.5.4 UV–Vis Extinction Measurements

The absorption measurements of the cQDs in solution were carried out with an Agilent Carry 5000. The PbSe and PbS cQDs were dispersed in trichloroethylene for these measurements.

3 Sintered PbSe/PbS Photodetector

3.5.5 FTIR Characterization

PbSe/PbS Absorption Measurements

The absorber materials were deposited on sapphire windows and characterized with a Bruker vertex 70 FT-IR spectrometer in a transmission measurement configuration.

Metamaterial Absorption Measurements

The metamaterial photoconductors were placed in a custom-built setup (Figure 3.10) and characterized with an Arc Optics FTIR-Rocket spectrometer in a reflection measurement configuration.

3.5.6 Device Fabrication

Interdigitated Finger Structure Photoconductor

The finger structures for the photoconductors were fabricated by a standard photolithography, e-beam evaporation, lift-off process on Si substrates with a thermal grown 200 nm thick SiO₂ layer. The evaporated Au layer was 70 nm thick and the contacts of the photoconductors were 2 μm wide and 2 μm spaced, resulting in an overall device size of 66 × 20 μm². These structures were covered with the different absorber materials, and finally, a 120 nm thick PMMA was spun on top as an oxidation protection.

Metamaterial Device Fabrication

For the metamaterial devices, a 100 nm thick tungsten (W) backplane was sputtered onto Si substrates, which was then covered by 100 nm ALD grown alumina (Al₂O₃). The 70 nm thick gold (Au) top resonator structure was fabricated by a standard e-beam lithography, e-beam evaporation, lift-off process. The PbSe layer deposited on to the metasurface was 30 nm, and the PbS layer was 25 nm thick. An oxidation protection of 120 nm of PMMA was spun on the cQDs. The fabricated devices were 30 × 30 μm² in size.

3.5.7 E/O Characterization

An illustration of the optical setup used can be seen in Figure 3.10. For the electrical characterization, a Keysight B2902A SMU was used as voltage source and the responsivity and noise measurements were carried out with a lock-in amplifier Zurich Instruments MFLI. A calibrated powermeter, Gentec-EO TH5B-BL-DZ-D0, was used to determine the incoming power on the device.

3.5.8 Thickness Characterization of Annealed QD Layers

The thickness of the annealed layers was characterized with an AFM. The QDs were deposited onto a Si substrate and partially removed before annealing. After the annealing, the substrate was characterized with an AFM, which allowed us to measure the height difference between the substrate with and without annealed QDs.

3 Sintered PbSe/PbS Photodetector

3.6 Supporting Information

3.6.1 cQD Synthesis

Synthesis of PbS Nanocrystals

In a typical synthesis of 8 nm PbS nanocrystals[203], we mix 1.8 g of PbO with 60 ml of oleic acid and 20 ml of 1-octadecene in the three-neck flask. The reactor is then connected to the Schlenk line set-up and heated to 150°C for 1 hour in vacuum. During this time, the mixture is purified from oxygen and water residues, while simultaneously PbO and oleic acid react forming Lead (II) oleate, a precursor of Pb. Afterwards, the reactor is put under a nitrogen stream (1 bar), while the temperature is kept at 150°C. At these conditions, a sulfur precursor mixture, consisting of 0.84 ml of hexamethyldisilthiane and 40 ml of 1-octadecene, is introduced to the reaction via fast injection. The mixture turns brown within a few seconds, indicating a formation of PbS nanocrystals.

To achieve a good size distribution of PbS nanocrystals, the reaction is taken through a optimized temperature profile, namely (i) a natural cooling to 120°C during the first minute of reaction; (ii) slower cooling to 100°C within the next 3 minutes; (iii) annealing at 100°C for 5 minutes; (iv) fast cooling to room temperature to terminate the reaction and mass transfer processes.

As synthesized nanocrystals are then transferred air free to the glovebox and purified by the addition of hexane and ethanol solvents. This step is followed by centrifugation, the overall purification cycle is repeated 3 times.

Synthesis of PbSe Nanocrystals

Synthesis of PbSe nanocrystals is derived from the PbS synthesis above, replacing the sulfur precursor with trioctylphosphine selenide and adding diphenylphosphine as nucleation promoter[186].

In a typical synthesis of 4 nm PbSe nanocrystals, we mix 2.2 g of PbO with 7.86 ml of oleic acid and 34.26 ml of 1-octadecene and heat this mixture at 150°C and vacuum to form Lead (II) oleate. Afterwards, the injection mixture of 30 ml of 1M trioctylphosphine selenide and 0.2 ml of diphenylphosphine is added, triggering the formation of PbSe nanocrystals. The reaction time is shortened to 30 seconds, after what the reaction is terminated by fast

cooling to the room temperature. Post-synthetic purification of PbSe nanocrystals is carried out in complete analogy to the PbS synthesis above.

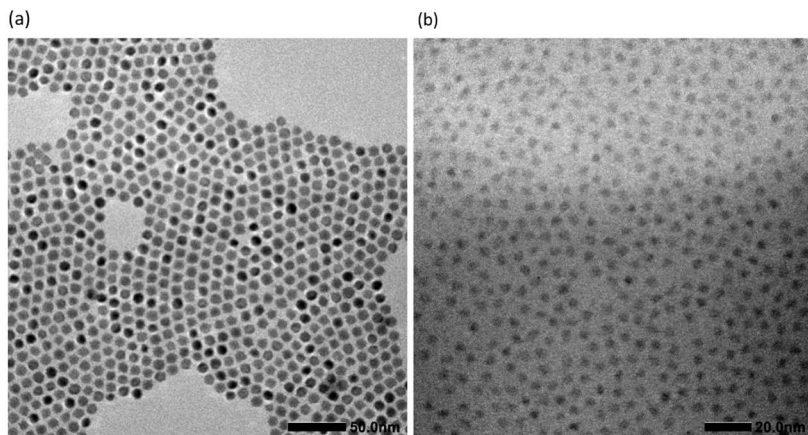


Figure 3.7. (a) TEM image of 4 nm PbSe cQDs. (b) TEM image of 8 nm PbS cQDs.

3 Sintered PbSe/PbS Photodetector

3.6.2 Time Dependent XRD Measurements

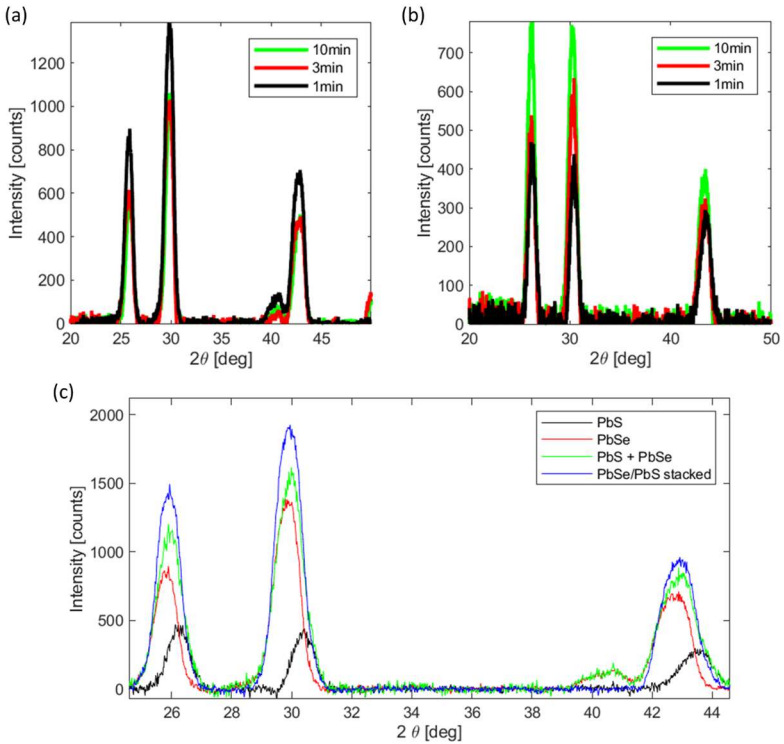


Figure 3.8. (a) PbSe XRD spectra for different annealing times. It can be seen that the peak height decreases with increasing annealing time, indicating a decrease of crystallinity for longer annealing times. (b) PbS XRD spectra for different annealing times. It can be seen that the peak height increases with increasing annealing time, indicating an increase in crystallinity for longer annealing times. (c) XRD pattern a single layer of PbS (black) and a single layer of PbSe (red) annealed for 1 min at 310 °C. The arithmetic sum of the annealed PbSe and PbS pattern (green) and the GIXRD pattern of the stacked PbSe/PbS layers. It can be seen that the shape of the single layers matches very well the shape of the PbSe/PbS bilayer stack. The difference in peak intensity is attributed to a difference in the thickness of the measured layers.

3.6.3 AFM Characterization

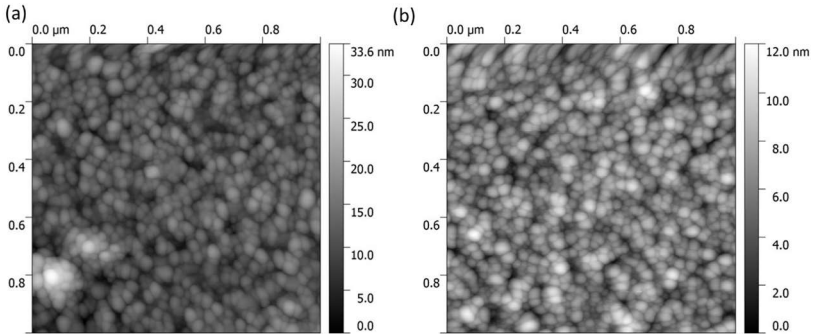


Figure 3.9. (a) AFM image of 1 min at 310°C annealed PbSe showing a root mean square (RMS) surface roughness of 3.54 nm. (b) AFM image of 1 min at 310°C annealed PbS showing a RMS surface roughness 1.75nm.

3.6.4 Optical Setup

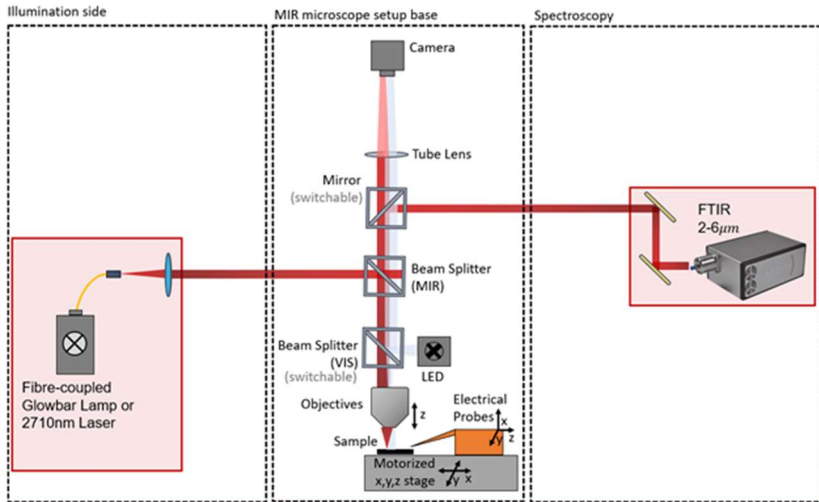


Figure 3.10. Illustration of the optical setup used for the electro-optical characterization.

3 Sintered PbSe/PbS Photodetector

3.6.5 Discussion on the Origin of the Photoconductivity in the Annealed PbSe cQD Layers

The annealed PbSe shows a significant photoresponse in the MIR without any sensitization. Recent works suggest that the formation of trap states at grain boundaries, which are often accredited to oxides, play a significant role for the photoconductance of PbSe [103, 204]. Although, no oxides are expected to form in the annealed PbSe cQD layer, we suspect that trap states exist at the grain boundaries.

More precisely, layers consisting of cQDs have a very large surface due to the large surface to volume ratio of the individual cQDs. The surfaces of cQDs usually have a large number of defects which is why a lot of effort has been put into different ligand exchange methods to passivate the surface and surface traps. We expect that during the annealing most of ligands evaporate and several cQDs fuse into larger grains. Despite the fusing we suspect that a large number of the original traps on surface of the individual cQDs are still present at the grain boundaries of the annealed layer. Since the cQDs crystallize into small grains many boundaries with the accompanying traps exist in these layers, which lead to an increased photoresponse.

3.6.6 Discussion on the Presences of a Heterojunction

In the main text we have already argued that the heterojunction formation can be observed by the fact that the current decreases in the PbSe/PbS stack when applying a forward current due to the depletion of carriers at the interface. Here we give more arguments for the formation of a heterojunction.

It can be expected that the two materials form a heterojunction since bulk PbSe has an electron affinity of $\chi_{\text{PbSe, bulk}} \approx 4.7$ eV and a bulk band gap of $E_{\text{g, PbSe}} \approx 0.27$ eV, which is known to form a heterojunction with PbS ($\chi_{\text{PbS, bulk}} \approx 4.55$ eV, $E_{\text{g, PbS}} \approx 0.4$ eV) [181–184]. Although these values can differ for cQDs [183, 184, 205–207] and the exact values are unknown for the annealed cQD layers presented in this work, the formation of a heterojunction between individual PbS and PbSe crystal domains may be expected due to the differences in the band gap.

A further indicator of the presence of a heterojunction can be seen by analyzing the normalized I-V curves shown in Figure 3.11. PbS forms an ohmic contact with Au which results in the nearly linear I-V, whereas PbSe

forms a Schottky type contact. This difference in contact type indicates that the barrier height between Au and the pristine materials PbS and PbSe are likely to be different. In such a case it can be argued that energetic band position of PbS and PbSe differ as well, which also should lead to the formation of a heterojunction if the materials are brought into contact with each other.

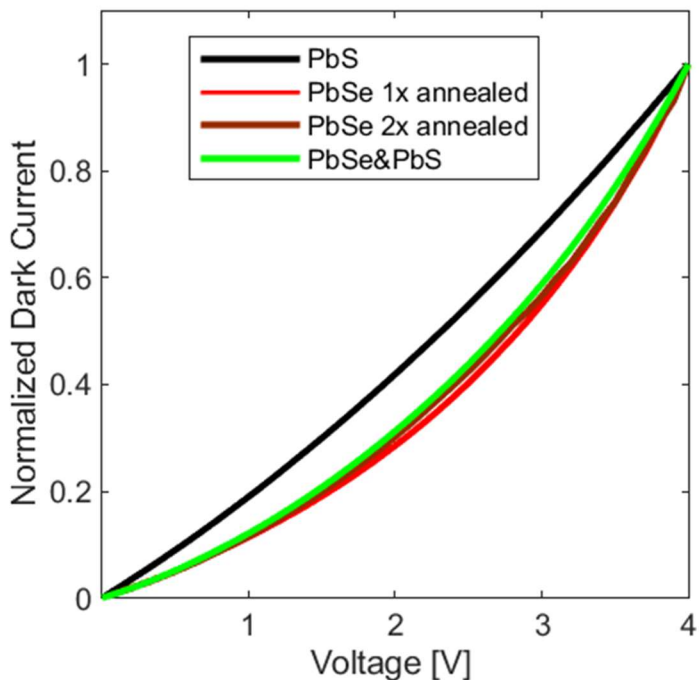


Figure 3.11. To maximum current normalized dark current. It can be seen that the different materials form different contact types to the Au electrodes.

3 Sintered PbSe/PbS Photodetector

3.6.7 Time Dependent Photoresponse

In Figure 3.12 (a) the photoresponse over a long period of time is shown and in Figure 3.12 (b) the photocurrent at a modulation frequency of 4 Hz, which was used to measure a responsivity of ~ 250 A/W. The ratio of the maximum current of these measurements was used to calculate the maximum responsivity of ~ 375 A/W at a wavelength of 2710nm. Both measurements were performed under identical illumination conditions.

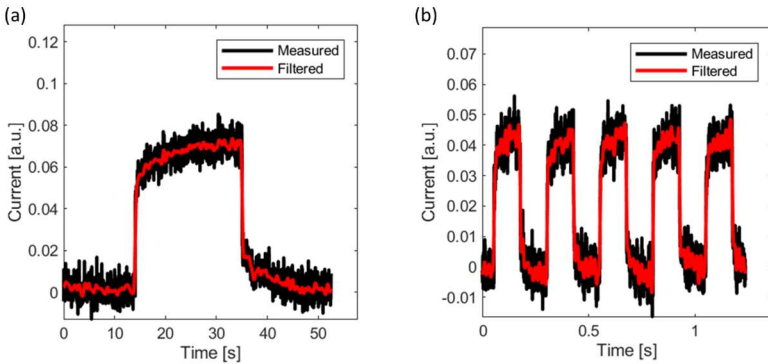


Figure 3.12. (a) Time dependent photoresponse of PbSe/PbS metamaterial enhanced photodetector. (b) Time dependent photoresponse of PbSe/PbS metamaterial enhanced photodetector at a modulation frequency of 4 Hz. Both measurements were performed under identical illumination conditions at a wavelength of 2710 nm.

3.6.8 Polarization Dependent Passive Absorption

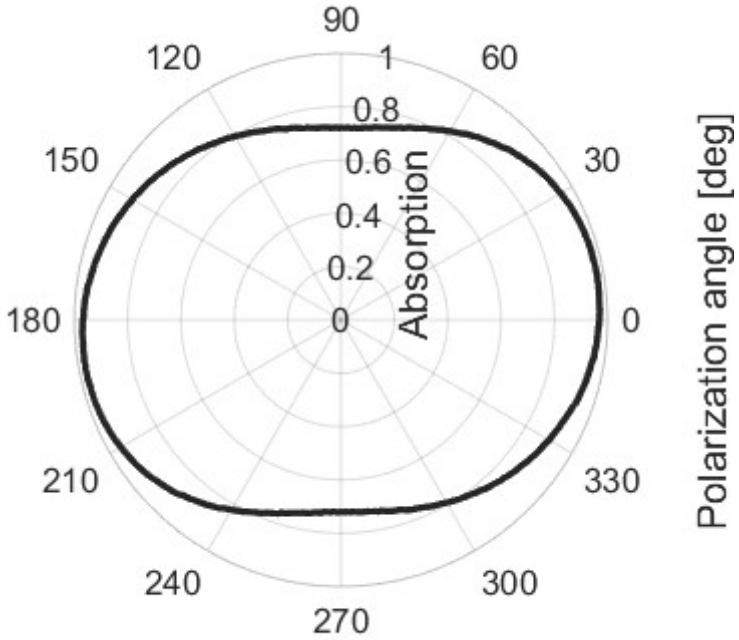


Figure 3.13. Polarization dependent passive absorption of a PbSe/PbS metamaterial enhanced photodetector ($l = 350\text{nm}$ and $p = 1\ \mu\text{m}$) characterized at a wavelength of $2710\ \text{nm}$ with a polarization controller. It can be seen that the absorption does not drop below 75% and that a near unity absorption can be reached for an ideal polarization state.

3 Sintered PbSe/PbS Photodetector

3.6.9 Characterization Metamaterial Photodetectors

Table 3.1. Metamaterial parameters and wavelengths at which they were characterized.

Device	Characterization Wavelength [nm]	Resonator length l [nm]	Period p [μm]
i	2710	350	1
ii	3250	400	0.8
iii	4000	550	0.9
iv	4250	600	0.9

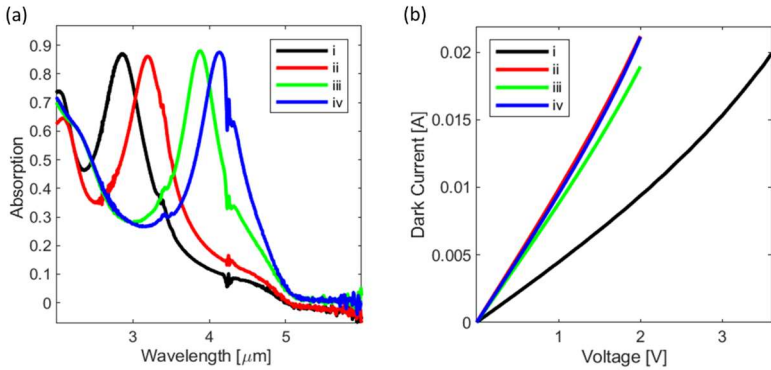


Figure 3.14. Additional measurements of the metamaterial photodetectors. Design parameters of the different detectors are listed in Table S1. (a) Passive absorption spectra of metamaterial photodetectors. (b) Dark I-V measurements of metamaterial photodetectors.

3.6.10 Comparison of Photodetectors

The below presented table provides an overview of recent publications of photodetectors operating in the MIR. The responsivities and detectivities are used as a figure of merit. This comparison focuses on 2D and cQD materials and their combination and is not complete. A single representative responsivity and detectivity value was selected if several values were given in the referenced publications.

Table 3.2. Comparison of this work and representative recent publications. Listing the materials and enhancement schemes such as metamaterials (MM), operation wavelength, responsivity R, detectivity, operating temperature and references.

Material	Wavelength (nm)	R (A/W)	Detectivity [Jones]	Temperature (K)	REF
PbSe, PbS & MM	2710	375	1×10^8	290	this work
PbSe, PbS & MM	3250	208	5×10^7	290	this work
PbSe, PbS& MM	4000	16	3×10^6	290	this work
PbSe, PbS& MM	4250	7.85	9×10^5	290	this work
HgTe	2500	0.8	6.5×10^{11}	290	[208]
HgTe	4800	1.5	5.4×10^{10}	80	[66]
HgTe & MM	4500	1.62	4×10^{11}	85	[74]
HgTe & Graphene	4000	0.08	4.2×10^{10}	138	[82]
HgTe & Graphene	2500	800	4.2×10^8	80	[83]

3 Sintered PbSe/PbS Photodetector

HgTe & Graphene	2500	0.0065	3×10^9	290	[84]
HgTe & MOS₂	2100	5000	1×10^{12}	290	[85]
HgSe	6000	0.8	1.5×10^8	290	[209]
HgSe	5000	0.0013	3×10^8	80	[210]
HgSe & HgTe	4400	0.001	1.5×10^9	RT	[211]
Ag₂Se	4500	0.02	1×10^7	RT	[212]
Ag₂Se	4400	0.013	3×10^5	RT	[213]
PbSe	3500	11	4.5×10^{10}	RT	[55]
PbSe	4000	49	-	RT	[176]
PbSe	4000	8	-	RT	[56]
Graphene & MM	4000	0.036	5×10^6	RT	[214]
Graphene & Ti₂O₃	4200	300	7×10^8	RT	[81]
Graphene & hBN antenna	6600	0.027	-	RT	[215]
Graphene & antenna	3000	1	-	RT	[216]
WS₂ & HfS₂	4700	791	3×10^{10}	RT	[217]
BP	3400	0.518	-	77	[218]
BP	3390	82	-	RT	[219]
BP & PETG	4320	3	5.97×10^9	RT	[220]

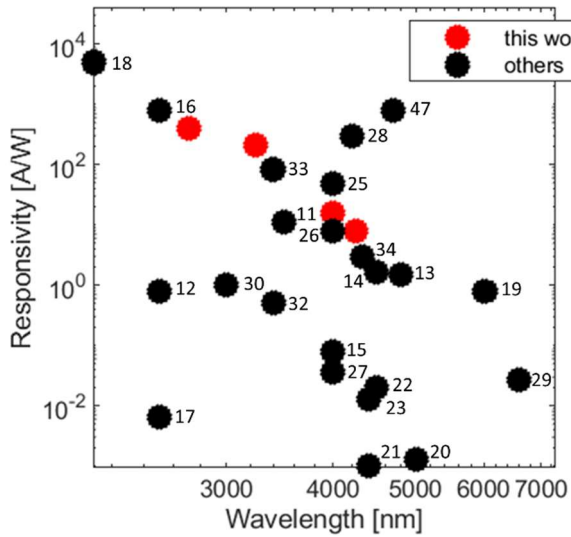


Figure 3.15. Responsivity comparison of published works and this work with references.

3 Sintered PbSe/PbS Photodetector

4 Metamaterial Optimization

Metamaterial Engineering for Superior HgTe cQD Photodetector Performance^{†*}

Raphael Schwanninger, Shadi Nashashibi, Olesya Yarema, Stefan M. Koepfli, Yuriy Fedoryshyn, Vanessa Wood, Juerg Leuthold

Advanced Optical Materials, vol. 15, no. 8, pp. 10847–10857, 2024

Abstract

Highly responsive, low noise, and inexpensive photodetectors that operate in the mid-infrared (MIR) wavelength regime are in high demand for applications ranging from fundamental science to large scale industries. However, simultaneously achieving all this in one device architecture is very challenging. In this work, mercury telluride (HgTe) colloidal quantum dot (cQD) based photodetectors are systematically improved by the introduction of new metamaterial designs. The new designs are found by utilizing simulations. Thereby the structures are optimized to increase the responsivity and simultaneously decrease the noise spectral current density. This is achieved by focusing on improving the photogenerated charge carrier collection efficiency while reducing the active material volume without altering the near unity absorption. A standard metamaterial perfect absorber architecture based on disc resonators is used as a starting point for the optimization process. By optimizing the carrier extraction through contact engineering, resulting in a narrow slot metamaterial, an overall ≈ 13 -fold responsivity and ≈ 345 -fold detectivity increase is achieved. The final metamaterial design reaches a responsivity of 16.2 A W^{-1} and detectivity of 6×10^8 Jones at a wavelength of 2710 nm. The analysis therefore provides a route to improve the responsivity and noise characteristics of mid-infrared photodetectors based on cost-efficient colloidal quantum dots.

* This chapter has been published in [J 1]. Copyright 2024 The Authors. Advanced Optical Materials published by Wiley-VCH GmbH. Figures, tables and notation were adapted for consistency throughout the thesis.

4 Metamaterial Optimization

Keywords

HgTe, metamaterial, mid-infrared, photodetectors, quantum dots

4.1 Introduction

Photodetectors are essential components for various applications such as thermal imaging[221], biomedical sensing[160], spectroscopy[222], environmental[81, 223] and gas monitoring[157, 158]. Given their great importance, ongoing efforts focus on enhancing their performance metrics, including responsivity and detectivity, while simultaneously reducing their cost. Achieving improvements across all these metrics is particularly challenging for detectors operating in the low energy photon MIR wavelength regime.[90]

Commercially available high-performance MIR-photodetectors are based on low band gap materials such as indium antimonide (InSb)[224], or multi quantum well structures (MQW)[225, 226]. These material systems are well established and can even reach performances close to the physical limitations.[95] However, these materials and their fabrication are often expensive and rely on sophisticated equipment. Additionally, such detectors often require operation at cryogenic conditions that typically entails further costs.[46, 73]

Promising alternatives to these materials and MQW structures are cQDs. They have the advantage that they can be fabricated and deposited using simple methods.[28, 227] HgTe cQDs are among the most promising materials for detectors operating in the infrared regime.[62] This can be attributed to their absorption tuneability which ranges from the shortwave infrared (SWIR 1.5-2.5 μm)[72, 208] to the MIR (3-5 μm) and even the THz[209, 228] spectral wavelength range.[229, 230] Although cQD materials hold great promise, they have unwanted limiting properties that have to be considered when designing a photodetector. Such limitations include low charge carrier mobility,[29] charge carrier traps and large $1/f$ noise.[231] The low mobility in combination with traps, which can act as recombination centers, can result in photogenerated electron-hole pairs recombining before reaching the contacts where they can be collected, thus decreasing the photoresponse.[29, 122]

Recently, what was referred to as band-like transport has been shown to occur in HgTe cQD clusters. It was observed that in small clusters of strongly coupled cQDs the mobility is increased compared to long range transport.[70] Audrey Chu et al.[72] utilized the observed effect to drastically increase the photoresponse while simultaneously reducing the noise in nanogap photodetectors. If electrodes are spaced at very small distances, photogenerated carriers can be collected more efficiently due to

4 Metamaterial Optimization

the short transfer time resulting from short charge carrier travel paths, which also increases gain.[58, 232, 233] Further, if the distances are extremely small, the mentioned mobility increase can be observed, leading to an additional increase of the responsivity. It has been also shown that the nanogap photodetectors exhibit a decrease of the noise spectral current density due to smaller $1/f$ noise since the active material volume is reduced[72, 234] such nanogap photodetectors can drastically increase the internal quantum efficiency and device performance, efficient optical coupling to such nanogaps and achieving high absorption in the cQD layer is difficult and thus limits the responsivity and practicability.

A method to overcome these limitations is by combining thin cQD layers with absorption enhancement schemes such as metamaterials. Metamaterial perfect absorbers have been combined in various ways with photoactive materials, where they have shown to enhance the absorption and device performance or achieve other functionalities.[235–238]

While absorption enhancement strategies such as metamaterials can improve the absorption, the photodetector can still be ineffective if the photogenerated charge carriers must travel large distances and thus recombine before reaching the contacts. Demonstrations of combining optical metamaterial resonators with electrical contact lines have shown improved performance for devices based on novel materials such as 2D materials and cQD.[2][6][5] However, metamaterial designs combining short carrier traveling lengths and high absorption are still scarce for lateral detector configurations.

In this work, we systematically improve the performance of metallic metamaterial enhanced HgTe cQDs photodetectors. We show that by optimizing the extraction of photogenerated charge carriers we can improve the responsivity and decrease the noise spectral current density while simultaneously maximizing the absorption. As an initial device a simple disc resonator-based metamaterial perfect absorber structure was combined with a thin HgTe cQD layer to increase the absorption. We then introduce electrical charge extraction in the form of straight interdigitated contact lines in between individual disc shaped resonators. These contacts were bent around the disc resonators in the following design to extract as many photogenerated carriers as possible. The contact lines were placed as close as possible to the areas with the strongest light absorption without distorting the metamaterial resonance, enabling more efficient charge carrier extraction and a volume reduction of active material, thus increasing

the responsivity, and decreasing noise. Ultimately, to achieve a narrow slot metamaterial, the contact lines were merged with the resonators forming a meander-shaped slot metamaterial. This simulation supported systematic engineering of the carrier extraction of the metamaterial enhanced photodetector led to an ≈ 13 -fold increase in responsivity, reaching 16 A W^{-1} at a wavelength of 2710 nm, and an average ≈ 50 -fold reduction of the noise current spectral density when comparing simple disc resonators with the slot metamaterial. These improvements resulted in a ≈ 345 -fold increase of the specific detectivity reaching $\approx 6 \times 10^8$ Jones at room temperature and a wavelength of 2710 nm. Furthermore, simulations showed for all metamaterials good angular stability and little polarization dependent absorption. All presented design improvements are supported by optical and electrical simulations giving a qualitative and intuitive understanding of concepts used to improve the photodetectors. This demonstration therefore enables the efficient design of future metamaterial-enhanced photodetectors operating at various wavelengths.

4 Metamaterial Optimization

4.2 Results and Discussion

4.2.1 Device Architecture

The metamaterial cQD photodetector optimization process was carried out with a metamaterial perfect absorber architecture as visualized in Figure 4.1(a). The devices were fabricated on a silicon (Si) substrate covered with a 250 nm thick thermally grown silicon dioxide (SiO_2) layer. On to this oxidized substrate the metamaterial stack was deposited consisting of a 100 nm thick gold (Au) backplane a 17.5 nm thick alumina (Al_2O_3) spacer layer and a 60 nm thick gold (Au) metamaterial top layer. The resonating top layer was covered by a 5 nm thin alumina layer, see inset in Figure 4.1(a). This thin insulating alumina layer that is only located on top of the contacts and resonating elements restricts the current flows through the absorbing QD layer to a lateral direction. Furthermore, this layer may reduce exciton quenching that has been observed in other works.[76] Lastly, the metamaterials are covered by a 60 nm HgTe cQD absorber layer that is passivated by a 120 nm thick PMMA layer. The photodetectors were fabricated in two sizes with an active area of 15×15 and $30 \times 30 \mu\text{m}^2$. In the visualizations shown in Figure 4.1. In the visualizations shown in Figure 4.1 – the cQD layer is only placed in between the contacts and resonators and the PMMA layer has been omitted to increase comprehensibility. The HgTe cQDs used in this work had an average diameter of ≈ 9 nm and an absorption onset at ≈ 4650 nm, see Figure 4.8(c) Section 4.5.1. A detailed description of their synthesis, ligand exchange and the used deposition method can be found in the Section 4.5.1.

The metamaterial resonator layer was systematically improved to achieve near unity optical absorption and high carrier extraction efficiency at the same time. Figure 4.1(b) illustrates the initial metamaterial structure that consists solely out of gold disc resonators. The metamaterial design in Figure 4.1(b) can only enhance the absorption and does not contribute to improving the carrier extraction. In order to improve the carrier extraction electrical contacts were added to the metamaterial. Figure 4.1(c) shows the disc resonators combined with electrical contact lines in between the resonators. Next, we bend the contact lines around the disc resonators as illustrated in Figure 4.1(d). The final design merges the contact lines and resonators, thereby consisting only out of contact lines that form a narrow-slot metamaterial themselves, Figure 4.1(e). Based on these four designs, we show the systematic enhancement of the photodetector performance.

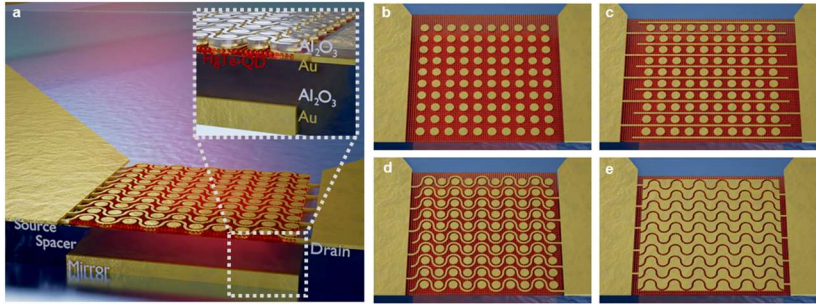


Figure 4.1. (a) Illustration of a metamaterial enhanced HgTe photodetector with source and drain contacts. The detectors consist of a 100 nm Au back reflector (Mirror), a 17.5 nm alumina spacer layer (Spacer), followed by 60 nm thick Au resonator with 5 nm alumina on top. The resonator layer is imbedded in a ≈ 60 nm HgTe layer that is covered by 120 nm PMMA nm layer for passivation. For comprehensibility the cQD layer was only infilled between the resonators and the PMMA was omitted in the main image. The inset shows the layer stack in more detail. Illustration of (b) disc resonator top layer, (c) disc resonator top layer with straight interdigitated finger contacts, (d) indicates the area disc resonator top layer with bent interdigitated contacts and (e) of narrow slot metamaterial.

4.2.2 Device Simulation

To optimize the metamaterial photodetectors optical and electrical simulations were performed using CST Suite 2022. A schematic of a unit cell implemented in CST can be seen Figure 4.2(a). The metamaterial was first simulated with respect to its optical characteristics and designed in such a way that near unity total absorption could be achieved. More precisely, 40% of the absorption is lost in the metal discs, whereas 60% of the absorption occurs in the HgTe cQD layer at a wavelength of 2710 nm. Identical absorption values in the HgTe layer on the order of 60% could also be achieved for all designs further below. It was observed that the absorption in the cQD layer decreased for larger wavelengths although still reaching overall near unity absorption. This decrease of absorption in the active layer coincides with the decreasing absorptivity of the cQDs, see Supporting Information Section 4.5.1 Figure 4.8(c) for the absorption spectra of the HgTe cQDs. The losses in the metal layer were mainly limited to the disc resonators to which the incoming light resonantly coupled, no grating effects or coupling of the incoming light to the contact lines was observed. Furthermore, all designs were simulated in such a way that the peak position can be tuned depending on the geometrical design parameters. The

4 Metamaterial Optimization

dependency plots of the absorption spectra on these parameters and the dependence of the absorption spectra on the polarization and illumination angle can be found in detail in the Supporting Information Section 4.5.2 for all designs. All designs were observed to demonstrate absorption that is independent of the polarization angle, coupled with excellent stability for varying illumination angles.

The simulated absorption spectra of the metamaterial for different disc diameters d can be seen in Figure 4.2(b), additionally in Figure 4.2(c) the spatial optical absorption distribution for unpolarized light in the cQD layer is shown.

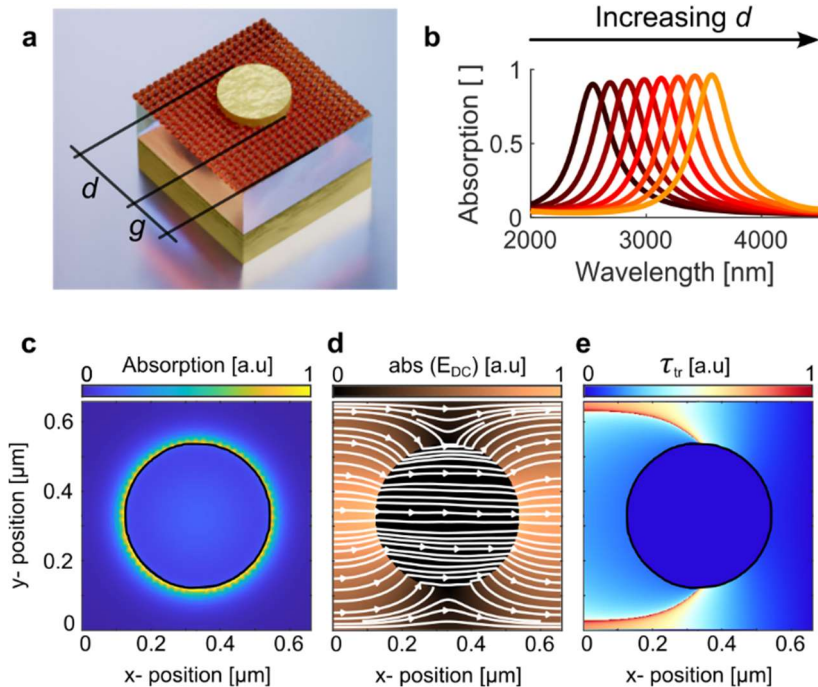


Figure 4.2. (a) Illustration of a disc metamaterial unit cell. (b) Simulated absorption spectra with varying diameter d ranging from 380 to 590 nm. The disc diameter d is increased in increments of 30 nm. The distance g between the disc resonators was kept constant at 80 nm. The spectra shift to larger wavelengths with increasing disc diameter (c) Normalized optical losses (absorption) of a disc resonator surrounded by HgTe cQDs. (d) Normalized static electric field resulting from external DC biasing including streamlines. (e) Normalized transition time for single type of charge carrier.

Electrical simulations were used to investigate the electric field (E_{DC} -field) distribution resulting from an externally applied static DC bias. The normalized static E_{DC} -field of the disc metamaterial without contact lines can be seen in Figure 4.2(d). From the electrical stimulation we extract the distribution of the normalized transition time τ_{tr} of photogenerated carriers in the QD layer. This distribution can be seen in Figure 4.2(e). Details on how the transition time distribution was calculated can be found in the Supporting Information Section 4.5.2.

Ideally the areas of greatest absorption, surrounding the disc resonator, and the areas with the shortest transition time overlap. This corresponds to the most efficient way to transport the photogenerated carriers to the contacts. Clearly, when analyzing Figure 4.2 (c)-(e), the absorption distribution (Figure 4.2(c)) does not show a strong overlap with the regions corresponding to the fastest carrier extraction pathways (Figure 4.2(e)). Further, in the case of simple disc resonator the carriers must travel across several unit cells until they reach the contacts. This long travel paths can have the consequence that a large number of photogenerated carriers recombine before they can be collected.

A simple method to increase the carrier extraction in a disc metamaterial is to place straight interdigitated contacts in between the individual disc resonators. A unit cell of such a metamaterial with interdigitated contacts can be seen in Figure 4.3(a), with a signal contact on the left and a ground contact on the right. Optical simulations showed that the interdigitated contact lines hardly distort the metamaterial disc resonance, as shown in Figure 4.3(b)-(c). Only when the contact lines are closer than 100 nm a broadening and shift of the resonance can be observed, see Supporting Information Section 4.5.2. In Figure 4.3 (c)-(e), the fields resulting from the optical and electrical simulations are shown. It can be seen that the normalized E_{DC} -field, absorption and the transition time distribution within a cell do not significantly change compared to the disc metamaterial without contact lines presented in Figure 4.2. The benefit of this design is that due to the metal contact lines, the carriers get extracted within each cell. Thus, the extraction pathways are cut down which that should improve the responsivity.

4 Metamaterial Optimization

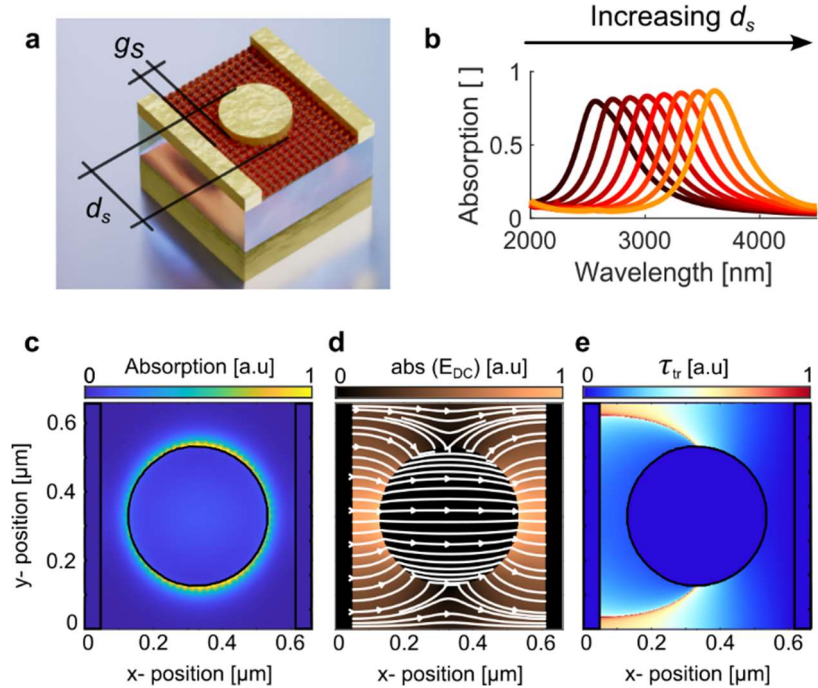


Figure 4.3. (a) Illustration of disc metamaterial unit cell with straight contact lines. (b) Simulated absorption spectra with varying diameter ranging from 380 to 590 nm. The disc diameter d_s is increased in increments of 30 nm. The distance g_s between the disc resonators is kept constant at 80 nm. The spectra shift to larger wavelengths with increasing disc diameter. (c) Normalized optical losses (absorption) of a disc resonator with straight contact lines surrounded by HgTe cQDs. (d) Normalized static electric field resulting from external DC biasing including streamlines. (e) Normalized transition time for single type of charge carrier.

To further improve the carrier extraction, we propose a new design consisting of interdigitated contact lines wrapped around the disc resonators. This design and the resulting field distribution can be seen in Figure 4.4. It was discovered that the meandering contact lines hardly influence the disc resonator resonance, as shown in the spectral absorption plot Figure 4.4(b)-(c). Similar to the metamaterials with straight contact lines, only when the contact lines are very close, i.e., below 80 nm, to the resonators a shift and broadening of the resonances can be observed, see Supporting Information Section 4.5.2.

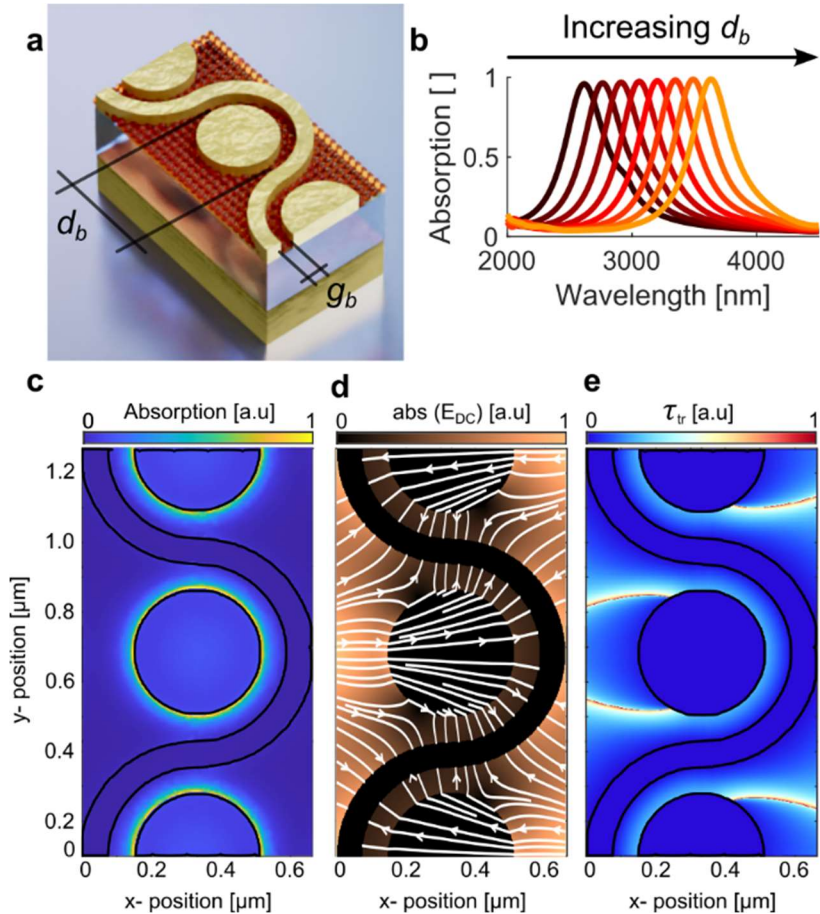


Figure 4.4. (a) Illustration of a disc metamaterial unit cell with bent contact lines. (b) Simulated absorption spectra with varying diameter ranging from 380 to 590 nm. The disc diameter d_b is increased in increments of 30 nm. The distance g_b between the disc resonators was kept constant at 80 nm. The spectra shift to larger wavelengths with increasing disc diameter. (c) Normalized optical losses (absorption) of a disc resonator with bent contact lines surrounded by HgTe cQDs. (d) Normalized static electric field resulting from external DC biasing including streamlines. (e) Normalized transition time for single type of charge carrier.

The design with the bent disc lines exhibits an improved overlap of the area of absorption (Figure 4.4(c)) and short carrier extraction (Figure 4.4(e)), which is expected to increase the device performance. The largest overlap

4 Metamaterial Optimization

is achieved in the area where the contact lines are bent around the discs forming a narrow slot. However, this area only covers half of the resonator; therefore, the design can be further improved.

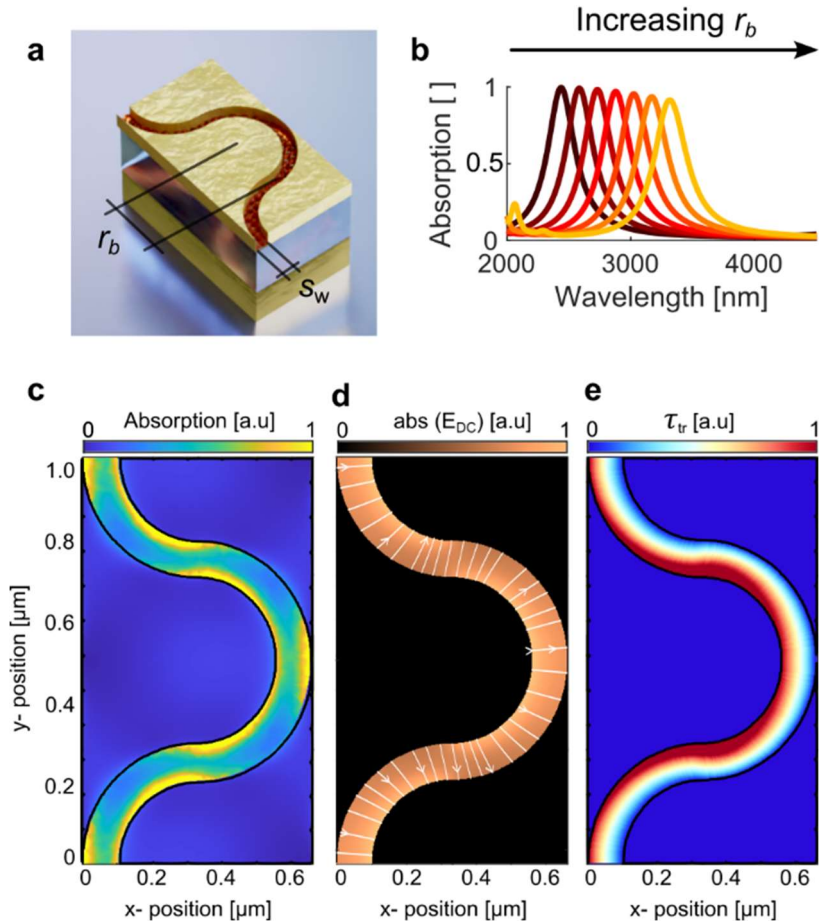


Figure 4.5. (a) Illustration of a narrow slot metamaterial unit cell. (b) Simulated absorption spectra with varying bend radius r_b ranging from 240 to 330 nm. The radius r_b is increased in increments of 15 nm. The slot width s_w of the metamaterial is kept constant at 80 nm. The spectra shift to larger wavelengths with increased radii. (c) Normalized optical losses (absorption) of a narrow slot metamaterial filled with HgTe cQDs. (d) Normalized static electric field resulting from external DC biasing including streamlines. (e) Normalized transition time for single type of charge carrier

To achieve the highest overlap of short carrier transit times and absorption, we propose the final design presented in this work, depicted in Figure 4.5. This metamaterial only consists of deformed interdigitated electrodes forming a narrow-slot metamaterial. With this design near unity absorption with $\approx 60\%$ absorption in the HgTe cQD layer could be achieved at a wavelength of 2710 nm, same as for the all disc metamaterials mentioned above. The absorption, static E_{DC} -field and resulting transition time distribution of this metamaterial can be seen in Figures 4.5(b)-(d). This metamaterial exhibits an ideal overlap of the static E_{DC} -field resulting from the external applied bias and area of absorption. Furthermore, the slots are very narrow therefore the transition times are short. A slight asymmetry in the plotted field can be observed, this is the result of an asymmetry of the design for narrow slots. The metamaterial design was scaled by a factor of 1.1 in the x-direction for gaps smaller than 80 nm achieving a minor increase of absorption and a improved Q-factor.

4.2.3 Passive Characterization

Following the metamaterial design and simulation process the envisioned metamaterials were fabricated, see scanning electron micrographs (SEM) in Figure 4.6. For detailed information on the fabrication process, we refer to the Experimental Methods Section. The HgTe cQD metamaterial detectors were characterized with a Fourier-transform infrared (FTIR) spectrometer to gain the spectral absorption after fabrication. The FTIR measurements were done in a reflection setup configuration. A schematic of the setup can be found in the Supporting Information Section 4.5.3, Figure 4.13.

In Figure 4.6 the measured and simulated spectra of the different metamaterials are plotted. The radii of the disc metamaterials and the radius of the bend of the slot metamaterials were varied, whereas the gap between discs, discs and contact lines or the slot width were kept the same at 80 nm. It can be seen that the simulated and measured absorption spectra generally match well. A small shift of the peak resonance position for the measured against the simulated slot metamaterials as well as lower absorption maxima is observed. We attribute this to fabrication deviations such as angled metal sidewalls that result in broadening of the resonance as well as deviating materials parameters of the cQD.

4 Metamaterial Optimization

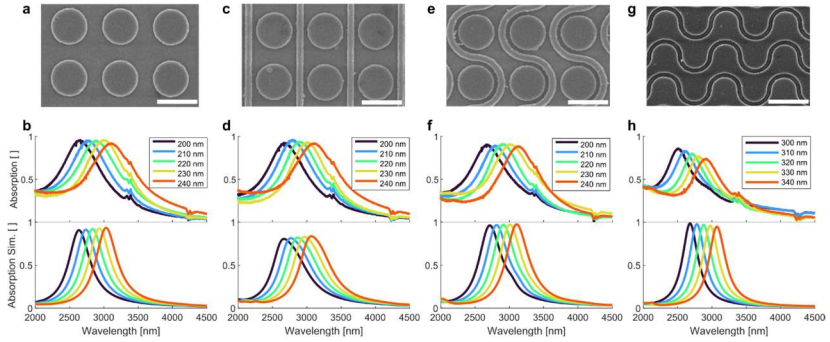


Figure 4.6. SEM image of the metamaterials before cQD deposition, measured (top) and simulated absorption spectra (bottom) for different radii of (a)-(b) disc metamaterial, (c)-(d) disc metamaterial with straight contact lines, (e)-(f) disc metamaterial with bend contact lines and (g)-(h) narrow slot metamaterial. All spectral measurements were done with metamaterials covered with HgTe cQDs and PMMA. The scalebar in the SEM images indicates a length of 500 nm.

Another difference between simulated and measured absorption spectra can be seen for all designs at smaller wavelengths. Here the measured absorption is larger than simulations predicted. This is attributed to material property data used for the simulations, which was for cQDs with a smaller diameter and therefore a different absorption onset.

In summary, all absorption spectra exhibit a narrow peak with a maximum overall absorption between 70 – 95%. Further, from these measurements it is clear that the absorption peaks can be tuned over a wide range.

4.2.4 Metamaterial cQD Photodetector Performance Characterization

The optical characterizations revealed that for all four metamaterial variations a similar optical absorption enhancement can be achieved. To verify the expected beneficial contributions of the contact lines, we subsequently characterize the photodetectors in terms of their active optoelectric (O-E) performance. This was done with a similar setup configuration as used for the passive characterization where the sample was illuminated from the top, same as for the O-E characterization. A schematic of the setup configuration can be found in the Supporting information Section 4.5.3, Figure 4.14.

We illuminate the different photodetectors under identical conditions with a laser source operating at a wavelength of 2710 nm. Electrically, the detectors were biased at their ideal operation voltage, i.e., in case of the disc metamaterials with contact lines and the slot metamaterial this meant that they were biased at a voltage where they exhibited the greatest photoresponse. For the disc metamaterials without contact lines a voltage was selected ensuring reliable operation, close but below the breakdown voltage. Further details on the voltage dependent photoresponse and current of different metamaterial photodetectors is shown in the Supporting Information Section 4.5.4.

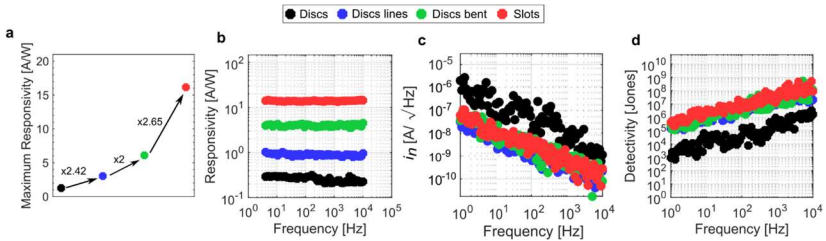


Figure 4.7. O-E characterization of the four different metamaterials. “Disc” refers to the disc metamaterial without contact lines, “Disc lines” refers to disc metamaterials with straight contact lines, “Disc bent” refers to disc metamaterials with bent meander shaped contact lines and “Slots” refers to narrow slot metamaterials. (a) Maximum responsivity of the 4 four different metamaterials. (b) Frequency dependent responsivity of typical metamaterial devices. (c) Current noise spectral density in versus frequency. (d) Detectivity versus frequency.

4 Metamaterial Optimization

We first compare the metamaterial cQD photodetector performance in terms of achievable responsivity. In Figure 4.7(a) the maximum responsivity of each of the metamaterials is plotted. The plot compares the best performing devices of each metamaterial design operating at its ideal conditions. In the plot it can be seen that there is a continuous increase of the responsivity for each of the improvement steps. The lowest responsivity is measured for the disc metamaterial with no contact lines with 1.25 AW^{-1} . By introducing the straight contact lines an increase of the responsivity by a factor of 2.4x could be achieved, resulting in a responsivity of 3 AW^{-1} . This increase is attributed to the increased carrier extraction, since the carriers are collected in between each disc. An additional increase of the photoresponse by a factor of 2x could be achieved by bending the contact lines around the disc resonators, highlighting the importance of the overlap of the external applied static EDC-field and the area of absorption. This design change step resulted in a responsivity of 6 AW^{-1} . The largest responsivity was recorded for the slot metamaterial, which was yet another factor 2.65x greater than for the disc metamaterial with bent meander shaped contact lines, reaching a responsivity of 16 AW^{-1} . We therefore achieved an overall factor 13x improvement over the disc resonator metamaterial, even though the overall absorption of the narrow slot metamaterial only reached $\approx 76\%$ at a wavelength of 2710 nm. These results are in line with our theoretical analysis on the extraction of the photo generated carriers.

To verify the here reported responsivity enhancement, we have additionally performed measurements on several devices to gain a statistical analysis. The resulting distributions and a discussion can be found in the Supporting Information Section 4.5.4.

The photodetectors were also characterized with respect to their frequency response as shown in Figure 4.7(b). For these measurements different detectors were characterized compared to the plot in Figure 4.7(a), but with the same design parameters. All photodetectors exhibited a constant photoresponse between a frequency range of 4 to 10 '000 Hz. The measurements were limited to this frequency range due to the limitations of the mechanical chopper used to modulate the incoming light. Time dependent photoresponse measurements at the maximum frequency of the mechanical chopper were additionally performed, see Supporting Information Section 4.5.6. From these measurements we were able to extract a rise time of $\tau_{rise} = 14 \mu\text{s}$ and a fall time of $\tau_{fall} = 17 \mu\text{s}$ for all devices.

No significant difference of the rise and fall time for the different photodetectors could be observed.

The engineering of the metamaterials was not only focused on increasing the responsivity but also on reducing the noise current spectral density by decreasing the active material volume. In the low frequency regime, where $1/f$ noise is dominant, it is possible to reduce the noise by reducing the volume of the cQD material. This is the case since $1/f$ noise can be seen as a superposition of Lorentzian shaped generation and recombination noise with different time constants and characteristics.[J 6] The generation and recombination noise is often dependent on trapping and de-trapping processes which that are related to defect sights in cQDs. By decreasing the volume of the cQD material the number of defect sights can be reduced resulting in an decrease of noise.[58, 239, 240] The noise reduction with the decrease of the active material volume between the contacts could also be observed throughout our measurements, as depicted in Figure 4.7(c). It can be seen that the disc metamaterial without any contact lines exhibits the largest noise. The introduction of straight contact lines in the disc metamaterial results in an average current noise reduction by a factor of 46, while bent contact lines yield a reduction by a factor of 30. Similarly, slot metamaterials exhibit a noise reduction by a factor of 27 compared to disc metamaterials without contact lines. The difference of the noise current of the photodetectors with contact lines and the slot metamaterial is attributed to the lower resistance. The different current noise of the different photodetectors therefore stems from the correlation between noise current and dark current magnitude.[241]

The reduced noise and increased responsivity result ultimately in an increase of the specific detectivity as shown in Figure 4.7(d). The specific detectivity D^* was calculated using the equation $D^* = R * (\sqrt{A}/i_n)$, with A being the active area and R the responsivity. The detectivity was increased by a factor of $\approx 110x$, $\approx 145x$, and $\approx 345x$ when comparing the metamaterial with straight contacts, bent contacts and the slot metamaterial with the disc metamaterial, respectively.

This clearly highlights the importance of charge extraction engineering in cQD photodetectors. Furthermore, these findings are not only limited to design of photodetectors operating in the MIR spectral range. A short discussion on the applicability of these findings can be found in the Supporting Information Section 4.5.7.

4 Metamaterial Optimization

4.3 Conclusion

In this work we designed, simulated, fabricated, and characterized metamaterial enhanced HgTe cQD photodetectors operating in the MIR spectral range. The focus of this work was set on enhancing the photodetector performance by increasing the photogenerated collection efficiency and therefore the responsivity while simultaneously decreasing the noise and using cost-efficient cQDs. To this end a metallic disc metamaterial enhanced photodetector was stepwise improved using simulations and then verified experimentally. The carrier collection efficiency was improved by reducing the carrier extraction time. This was partially achieved by introducing contacts in between the disc resonators, thus drastically reducing the carrier extraction path lengths. To further improve the devices the contacts were deformed and wrapped around the resonator to gain a greater overlap between the externally applied E_{DC} -field, responsible for carrier extraction, and the area of greatest absorption, concentrated around the disc resonators. Finally, a metamaterial was designed consisting only out of slots with a uniform absorption overlapping with the extraction E_{DC} -field and short carrier extraction times. This systematic by simulations supported improvements resulted in a ≈ 13 -fold increase of the measured responsivity comparing the disc metamaterial and the slot metamaterial. Further, the introduction of the contact lines leading to final metamaterial design resulted also to a decrease of the noise by an average of a factor of ≈ 50 x, which is attributed to a reduced volume of the active material between the contacts. Overall, the design improvements lead to a 345-fold increase of the specific detectivity highlighting the importance of the contact engineering of metamaterial enhanced photodetectors.

Although a drastic improvement of the device performance could be shown by optimizing the metamaterials, there is still potential for further improvements especially concerning the absorber material. The observed responsivity increase is a result of the decreased carrier transition time due to shorter transition path lengths. An additional decrease of the transition time could be achieved by optimizing the cQD synthesis and ligand exchange, which could lead to increased mobilities.[65, 70] Further, it has been observed that the dark current can be decreased with a narrow size distribution of the cQD, leading to a reduced noise spectral density.[242] We expect that these improvements, coupled with more efficient infilling of the metamaterial slots, have the potential to enhance the performance of the

presented narrow slot metamaterial photodetector beyond current state-of-the-art detectors in terms of detectivity and cost-effectiveness.

The demonstrated design improvements highlighting the importance of the carrier extraction efficiencies and the reduction of material volume are not limited to photodetectors operating in the MIR spectral range but are of interest for photodetectors operating in various wavelength regimes.

4 Metamaterial Optimization

4.4 Experimental Section

4.4.1 Simulations

The electrical and optical device simulations were carried out using CST Studio Suite 2022. The material data was either used from the CST library or in case of HgTe extracted from the work of Prachi Rastogi et al.[243] The distributions of the transition time were gained by post processing of the electrical simulation results and is discussed in more detail in the Supporting Information Section S2 (Supporting Information).

4.4.2 cQD Synthesis

A detailed description of the synthesis of HgTe CQDs used in this work, transmission electron microscopy images, XRD characterization and FTIR absorption spectra can be found in the Supporting Information Section S1 (Supporting Information).

4.4.3 Device Fabrication

For the metamaterial enhanced photodetector fabrication, a Si substrate with 200 nm thermally grown SiO₂ layer on top was used. A 100 nm thick Au backplane for the metamaterial was deposited on to the substrate followed by atomic layer deposition of a 20 nm alumina spacer layer. Subsequently, standard e-beam lithography and lift-off process was used to define the resonant metasurface. The 55 nm thick Au layer and a 5 nm alumina layer on top were deposited using e-beam evaporation. On to the metamaterial structures a ≈60 nm thick ligand exchanged HgTe cQDs layer was deposited using spin coating. The ligand exchange was done in optimized fashion to previous reports.[72] A discussion on the choice of the absorber layer thickness can be found in the Supporting Information Section S8 (Supporting Information). The fabricated devices were 15×15 and 30×30 μm² in size. For the passive characterization large metamaterial areas with 175×175 μm² were fabricated.

4.4.4 Metamaterial and HgTe cQDs Absorption Measurements

The ligand exchanged cQDs were purified and drop cast onto an Au covered Si substrate and the characterized using a custom-built setup (Supporting Information Section S3, Supporting Information) with a free-space coupled Arc Optics FTIR-Rocket spectrometer in a reflection measurement configuration. The same setup was used to perform the

passive characterization of the different metamaterials covered with 60 nm cQDs and a 120 nm PMMA layer.

4.4.5 O-E Characterization

A schematic of the used setup for the optical excitation of the photodetectors can be found in the Supporting Information Section 4.5.3 (Supporting Information), Figure 4.14. A Keysight B2902A SMU was used for biasing the photodetector, which was then connected in series to the transimpedance amplifier current input of a MFLI lock-in amplifier from Zurich Instruments. With the help of the lock-in amplifier it was possible to acquire the noise current spectral density and the photoresponse of the device under test.

A reference photodetector with an area of $15 \times 15 \mu\text{m}^2$ was used to characterize the power distribution of the incoming light on the sample stage. The distribution of the power can be found in the Supporting Information Section S6 (Supporting Information). It was found that the spot size was larger than $15 \times 15 \mu\text{m}^2$. Further, a calibrated powermeter EO TH5B-BL-DZ-D0 from Gentec was used to measure the overall incoming power. These two measurements were used to calculate the power illuminating the DUT.

4.4.6 XRD Characterization

The ligand exchanged HgTe CQDs were deposited on to a Si substrate using drop casting and then characterized using a Rigaku SmartLab 9KW XRD-diffractometer.

4 Metamaterial Optimization

4.5 Supporting Information

4.5.1 HgTe Colloidal Quantum Dots: Synthesis, Ligand Exchange and Material Characterization

HgTe Synthesis

Chemicals used for HgTe cQD synthesis: oleylamine (90%, Acros Organic), mercury (II) chloride (99.999%, Strem), bis(trimethylsilyl)telluride (98%, Fisher), hexane, tetrachloroethylene, methanol, ethanol.

The oleylamine was previously degassed in a Schlenk line under vacuum at 120 °C for 1 hour and stored in a glovebox for future use.

The synthesis of HgTe nanocrystals followed a modified recipe.[64] Specifically, 0.54 g of HgCl₂ was mixed with 80 ml of purified oleylamine in the glovebox. The mixture was then transferred to the Schlenk line, degassed at room temperature for 20 minutes, and then degassed at 100 °C for an additional hour.

Following this the solution was heated to 120 °C in N₂ atmosphere, 280 μl of bis(trimethylsilyl)telluride in 10 ml of hexane were rapidly injected in mercury precursor solution. After 10 minutes of growth the reaction was quenched with 50 ml of tetrachloroethylene.

HgTe Ligand exchange and Deposition

The synthesized cQDs were ligand exchanged in solution before they were deposited onto the metamaterial chips. The ligand exchange was carried with a optimized recipe as already reported.[72]

The as synthesized cQDs were purified using a precipitation and redispersion process utilizing centrifugation. The initial washing was done by mixing the synthesis solution with methanol in a 1:1 ratio and centrifuging it. Then, the supernatant was discarded and the cQDs were dissolved in a toluene and oleylamine solution. The cQD solution was then 3 more times purified using methanol and a toluene oleylamine solution. After the purification the cQDs were dissolved at a concentration of ~15 mg/ml. The ligand exchange solution was prepared by dissolving HgCl₂ in a concentration of 0.5 mg/ml and Mph 120 μl/ml in DMF. The ligand solution was mixed in a 1:1 ratio with the cQD solution and then mixed vigorously for 1min resulting in a phase transfer of the cQDs. After the mixing hexane was added to the solution followed by another mixing step and subsequent

removal of the clear hexane phase. The purification step with hexane was repeated twice before centrifuging the solution and redissolving the cQDs in 100 μl of DMF.

The cQD ink was then placed on the sample with the metamaterial structures and spun for 180 s at 1200 rpm resulting in a ~ 60 nm thick layer.

HgTe Characterization

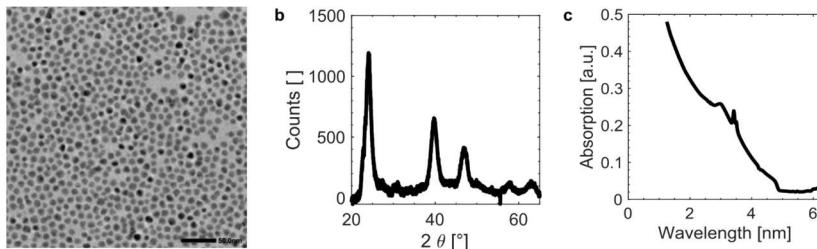


Figure 4.8. (a) TEM image of HgTe cQDs, scalebar 50 nm. (b) GIXRD spectra of HgTe cQDs showing characteristic pattern of HgTe. (c) FTIR Absorption spectrum of HgTe cQDs showing an absorption onset at a wavelength of ~ 4.65 μm .

The HgTe cQDs were characterized after synthesis to ensure high material quality. Therefore, the cQDs were characterized using TEM, see Figure 4.8(a) showing the spherical HgTe cQDs. These particles were also characterized with energy dispersive X-ray (EDX) to ensure a 1:1 Hg:Te ratio, the results of 3 measurements at different areas can be found in Table 1. Further characterization was done using grazing incidence X-ray diffraction (GIXRD). The GIXRD spectra with the for HgTe typical peaks can be seen in Figure 4.8(b). FTIR measurements of the HgTe were additionally done, see Figure 4.8(c).

4 Metamaterial Optimization

Table 4.1. Composition of HgTe nanocrystals, as derived by Energy-dispersive X-ray (EDX) spectroscopy (three separate measurements shown, indicating the 1:1 stoichiometry, consistently).

	Hg, at %	Te, at%
Measurement 1	49.08	50.92
Measurement 2	50.15	49.85
Measurement 3	49.40	50.60

4.5.2 Simulations

Transition Time Calculation

The normalized distribution of the transition time was gained by post processing of the electrical CST simulations in a simple physics framework. From these simulations the E-field \vec{E} distribution was gained, which was used to calculate the drift velocity \vec{v}_{drift} in each point of the simulation area using a constant mobility μ and the equation $\vec{v}_{\text{drift}} = \mu \vec{E}$. This velocity was then used to calculate the transition time t_r by using the equation $t_r = \sum \frac{dl}{v_{\text{drift}}}$ with dl being a fixed length. The sum was calculated along the path individual charge carriers take to reach the contacts resulting from the external bias field.

Absorption Spectra and Design Parameters

In this section simulation results are presented which highlight the tuneability of the absorption spectra depending on geometrical parameters of the metamaterial. Additionally, we present the dependence of the absorption on the polarisation angle Φ and the angle of the excitation θ . All metamaterials show good tunability and great angular stability while maintaining polarisation independence.

Disc Metamaterial Simulations

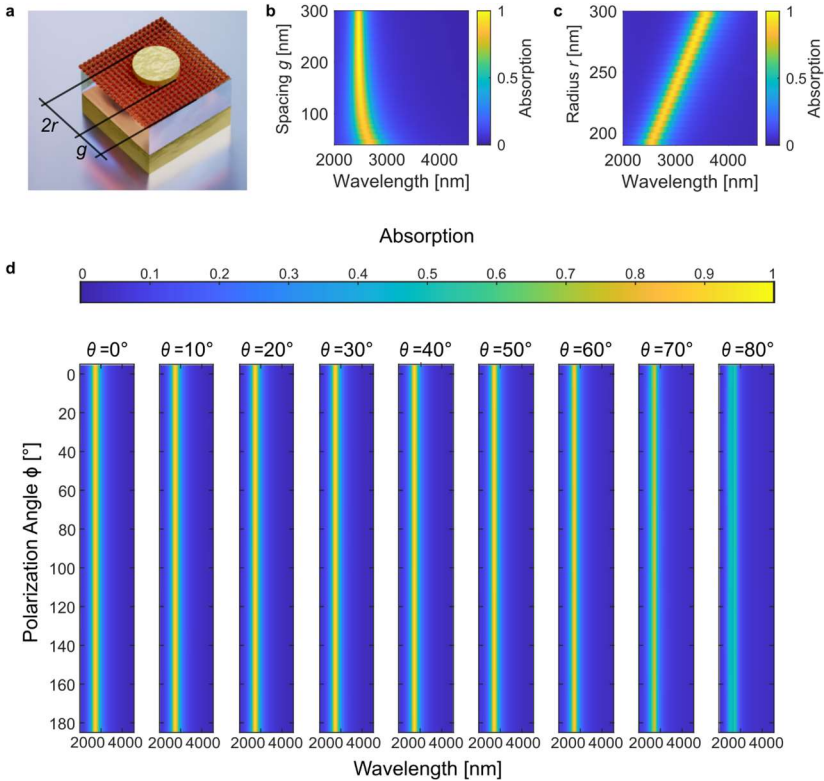


Figure 4.9. The simulated metamaterial stack consisted out of a 100nm Au backplane, a 17.5 nm Al_2O_3 spacer layer and a 60 nm thick top layer with embedded in a 60 nm thick HgTe layer. (a) Illustration of disc metamaterial unit cell including indication of design parameters. (b) Spectra absorption depending on spacing between individual discs g . Showing that a shift of the resonance to larger wavelengths and slight broadening takes place below ~ 80 nm spacing. (c) Spectra absorption depending on radius r of the disc resonator. It can be seen that the resonance position shifts to longer wavelengths with increasing radius. There is a linear relation between peak resonance position and radius of the disc resonators. (d) Shows the absorption spectra depending on the angle of the incoming excitation with the azimuth Φ and the elevation θ . The plotted absorption spectra show no dependence on the angle Φ which shows that the metamaterial is polarization independent. Furthermore, a drop of the absorption peak can only be observed for elevations larger than 60° .

4 Metamaterial Optimization

Disc Metamaterial with Straight Contacts Simulations

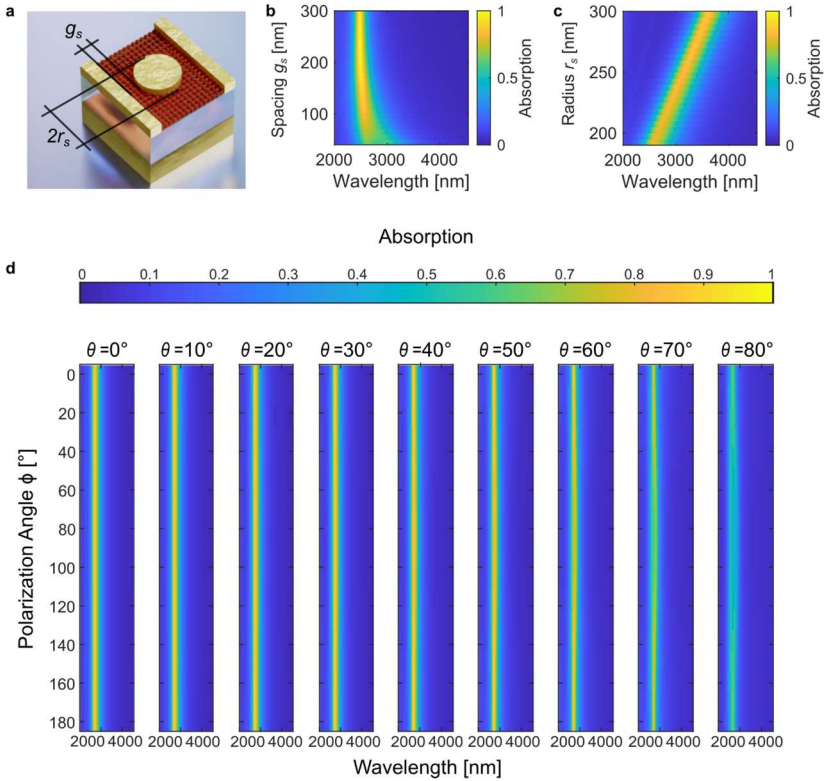


Figure 4.10. The simulated metamaterial stack simulated consisted out of a 100 nm Au backplane, a 17.5 nm Al_2O_3 spacer layer and a 60 nm thick top layer with embedded in a 60 nm thick HgTe layer. (a) Illustration of disc metamaterial with straight interdigitated contacts including indication of design parameters. (b) Spectra absorption depending on spacing between contacts and discs g_s . Showing that a shift of the resonance to larger wavelengths and broadening takes place below ~ 100 nm spacing. Further a decrease of the peak resonance can be observed. (c) Spectra absorption depending on radius r_s of the disc resonator. It can be seen that the resonance position shifts to longer wavelengths with increasing radius. There is a linear relation between peak resonance position and radius of the disc resonators. (d) Shows the absorption spectra depending on the angle of the incoming excitation with the azimuth Φ and the elevation θ . The plotted absorption spectra show no dependence on the angle Φ which shows that the metamaterial is polarization independent. Furthermore, a drop of the absorption peak can only be observed for elevations larger than 60° .

Disc Metamaterial with Bent Contacts Simulations

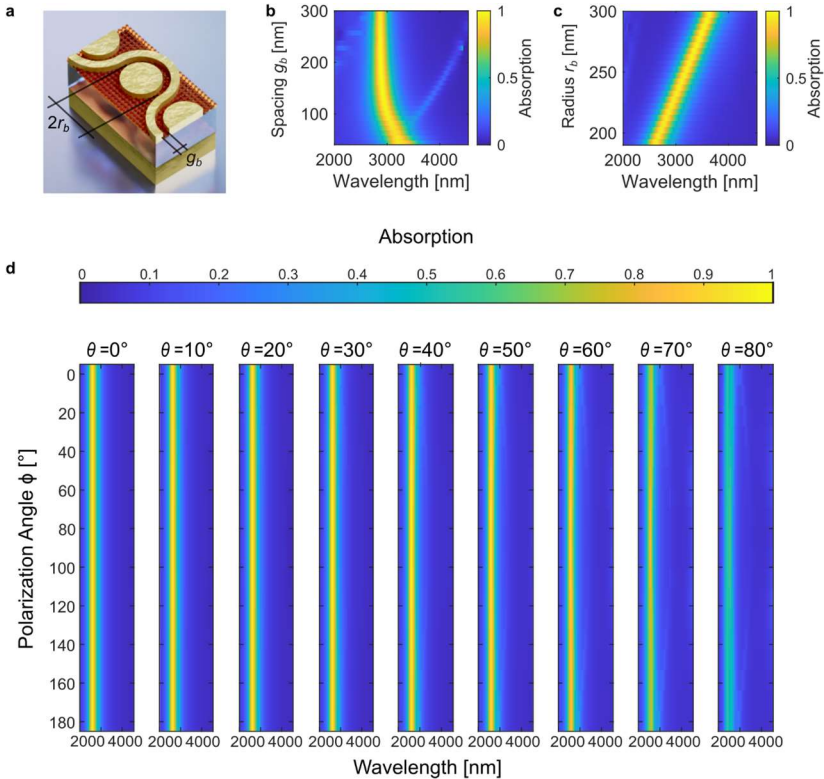


Figure 4.11. The simulated metamaterial stack consisted out of a 100 nm Au backplane, a 17.5 nm Al_2O_3 spacer layer and a 60 nm thick top layer with embedded in a 60 nm thick HgTe layer. (a) Illustration of disc metamaterial with bent interdigitated contacts including indication of design parameters. (b) Spectra absorption depending on spacing between contacts and discs g_b . Showing that a shift of the resonance to larger wavelengths and broadening takes place below ~ 100 nm spacing. Further a decrease of the peak resonance can be observed. (c) Spectra absorption depending on radius r_b of the disc resonator. It can be seen that the resonance position shifts to longer wavelengths with increasing radius. There is a linear relation between peak resonance position and radius of the disc resonators. (d) Shows the absorption spectra depending on the angle of the incoming excitation with the azimuth Φ and the elevation θ . The plotted absorption spectra show no dependence on the angle Φ which shows that the metamaterial is polarization independent. Furthermore, a drop of the absorption peak can only be observed for elevations larger than 60° .

4 Metamaterial Optimization

Slot Metamaterial with Bent Contacts

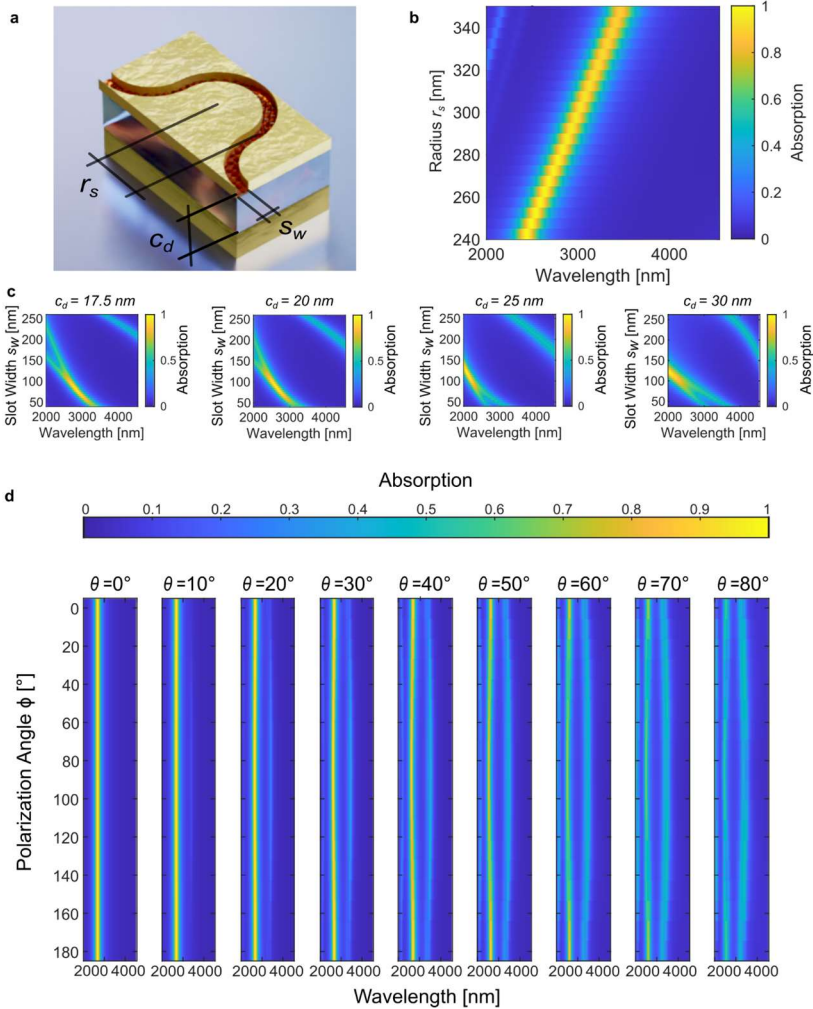


Figure 4.12. The simulated metamaterial stack consisted out of a 100 nm Au backplane, a Al₂O₃ spacer layer and a 60 nm thick top layer with embedded in a 60 nm thick HgTe layer. (a) Illustration of narrow slot metamaterial including indication of design parameters. (b) Spectra absorption depending on bent radius. The simulations show that the resonance peak position can be varied with the bent, an increase of the bent radius results in a shift of the resonance peak position to longer wavelengths. The Al₂O₃ spacer layer thickness was 17.5 nm. The thickness of the Al₂O₃ spacer layer c_d was varied for the slot width s_w sweep, with a thickness of

(c) 17.5 nm, 20 nm, 25 nm and 30 nm. It can be seen that for each spacer layer thickness an ideal gap width exists resulting in a narrow and near unity resonance. For larger slot widths a thicker spacer layer is desired. (d) Shows the absorption spectra depending on the angle of the incoming excitation with the azimuth Φ and the elevation θ . The plotted absorption spectra show no dependence on the angle Φ which shows that the metamaterials is polarization independent.

4.5.3 Characterization Setups

FTIR Measurement Setup

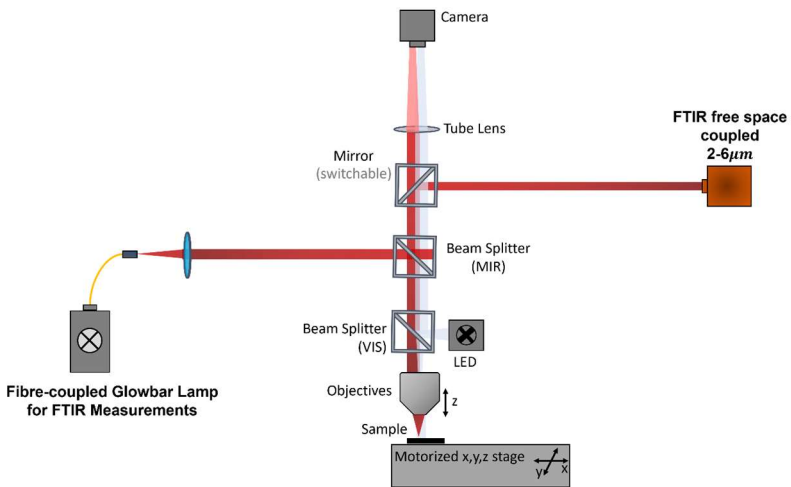


Figure 4.13. Illustration of the optical setup used for the passive characterization of the metamaterials (FTIR measurements). Adapted from [J 1].

4 Metamaterial Optimization

O-E Measurement Setup

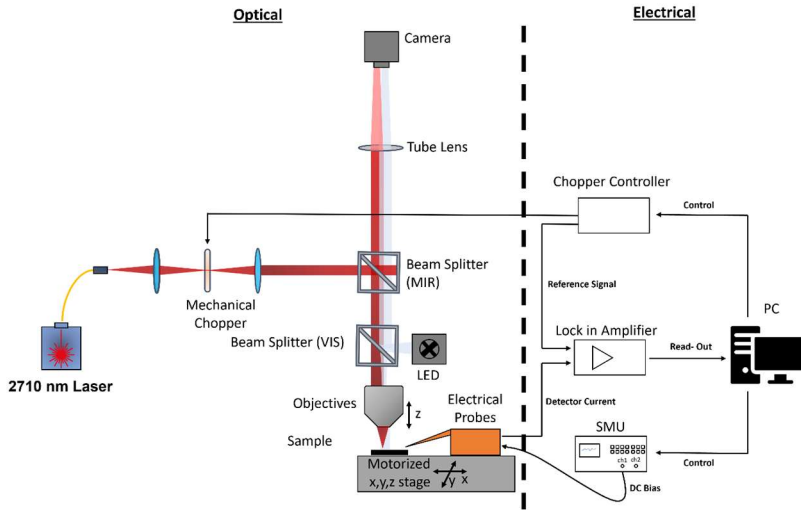


Figure 4.14. Illustration of the setup used for the opto-electric characterization of the photodetectors. Adapted from [244].

4.5.4 Photodetector Characterization

Current-Voltage Measurements

In this section we are presenting voltage dependent current and responsivity measurements. All measurements shown were done with devices exhibiting a typical photoresponse and current. In Figure 4.15 the voltage dependent currents of four metamaterial devices are plotted. It can be seen that the currents for the metamaterials with contacts and the slot metamaterial are large and show a different I-V trend, Figure 4.15(b)-(d), compared to the disc metamaterial photodetector, Figure 4.15(a). This is attributed to large conductivity of the HgTe cQDs and the short distances between the electrodes.

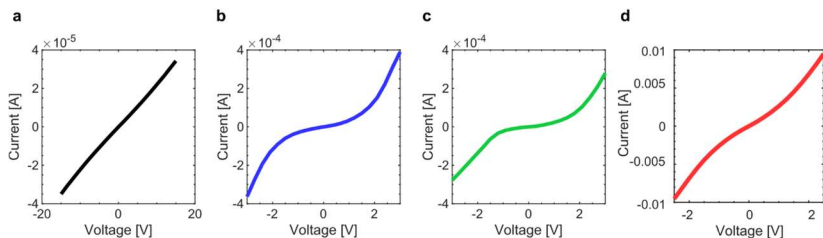


Figure 4.15. Current vs voltage measurement of (a) a disc metamaterial photodetector, (b) disc metamaterial photodetector with straight contacts in between the discs, (c) disc metamaterial photodetector with bent contacts in between the discs, (d) of a typical narrow slot metamaterial.

Responsivity-Voltage Measurements

In Figure 4.16 typical voltage dependent responsivity plots are shown. This plot should only visualize the trend of the voltage -responsivity curves of the different metamaterials. It can be seen that for metamaterials with contacts, plots Figure 4.16(b)-(d), the responsivity does only increase linearly over certain voltage range. After this range the responsivity does not increase further and for some devices even decrease. All detectors which were electro-optically characterized were biased with voltages in the linear voltage-responsivity regime ensuring reliable operation.

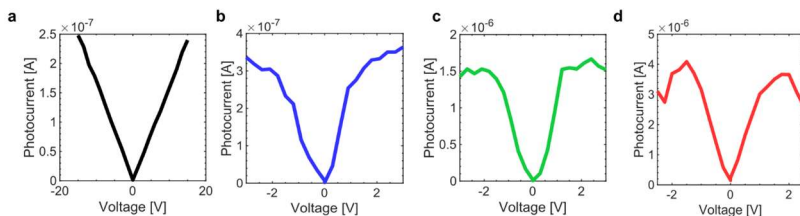


Figure 4.16. (a) Current vs voltage measurement of a typical disc metamaterial photodetector. (b) Current vs voltage measurement of a typical disc metamaterial photodetector with straight contacts in between the discs. (c) Current vs voltage measurement of a typical disc metamaterial photodetector with bent contacts in between the discs. (d) Current vs voltage measurement of a typical narrow slot metamaterial.

4 Metamaterial Optimization

Statistical Responsivity Analysis

Several photodetectors have been characterized and statistically analysed to ensure that the observed device trends are not only present in single selected devices. That this is indeed the case can be seen in Figure 4.17. It is shown that the average photoresponse scales in the same manner as presented in the main text. Further it can be seen that the deviation of the response increases for the metamaterial detectors with contacts. For these detectors the narrow slot metamaterial exhibits the largest deviation followed by the disc metamaterial with bent contact lines and the metamaterial with straight lines. This trend is attributed to variations of the infilling of cQDs in between the disc resonators and the contacts and the infilling of the narrow slots. Additionally, fabrication deviations have a greater influence on the device performance of slot metamaterials and disc metamaterials with bent contact lines than for the metamaterial with straight contacts.

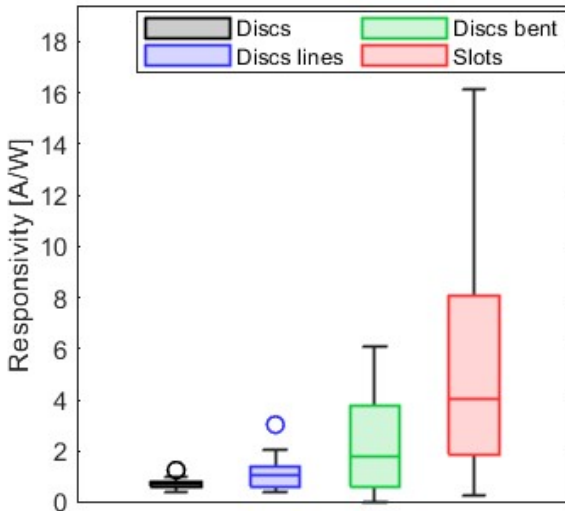


Figure 4.17. Box chart of the different metamaterials. “Disc” refers to the metamaterial consisting out of disc resonators without contact lines, “Disc lines”, refers to disc metamaterials with straight contact lines in between them, “Disc bent” refers to disc metamaterials with bent meander shaped contact lines and “Slots” refers to narrow slot metamaterials. For these measurements 11 device of each metamaterial were measured.

Time Dependent Photoresponse

Time dependent photoresponse measurements were performed at the maximum frequency of the mechanical chopper (10'000 Hz).

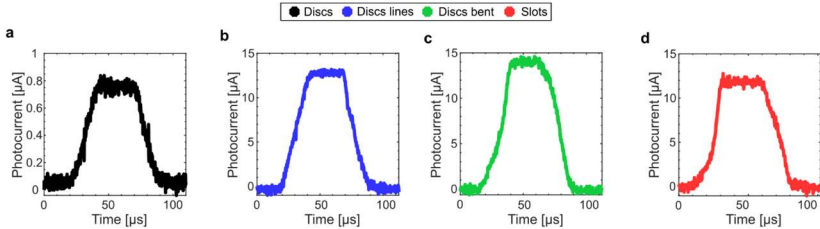


Figure 4.18. Photocurrent vs. time of (a) a disc metamaterial photodetector, (b) a disc metamaterial photodetector with straight contact lines, (c) a disc metamaterial with bent contact lines and (d) a slot metamaterial photodetector.

4.5.1 Power Distribution

This power distribution was acquired with a calibrated photodetector with an active area of $15 \times 15 \mu\text{m}^2$. The detector was used to scan the illumination area to gain the power distribution and calculate the incoming power on the cQD HgTe detectors.

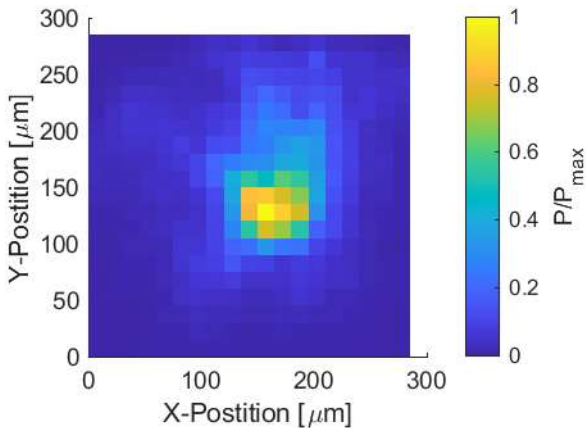


Figure 4.19. Power distribution on stage measured with a reference detector with an active area of $15 \times 15 \mu\text{m}^2$.

4 Metamaterial Optimization

4.5.2 Applicability to Other Wavelengths

We believe that the demonstrated concept of improving the photocarrier collection efficiency and thus increasing the responsivity and reducing the active material volume to decrease noise are of great importance for photodetector operating in various wavelength regimes such as UV, visible and NIR.

Although this work is of interest for photodetector operation at different wavelengths the presented metamaterial designs have certain limitations and are not applicable for all wavelength ranges. The peak enhancement wavelength of the disc metamaterials and slot metamaterials scale with the disc radii and bent radii, as shown in the Supporting Information Section 2. A smaller disc or bent radius blue shifts the peak enhancement wavelength. Thus, if the enhancement should take place at shorter wavelengths the feature size of the metamaterials have to be smaller, which finally leads to fabrication limitations. Therefore, it is not possible to directly scale the shown metamaterial designs in the UV and visible spectral range and another design needs to be found. However, the concepts of enhancing the carrier extraction while reducing material volume and maintaining large absorptions may be used for the design of novel metamaterials operating in the UV-VIS spectral range.

4.5.3 HgTe Absorber Thickness

The decision to set the active material layer thickness to 60 nm was mainly driven by fabrication considerations. Initially, we determined the thickness of the Au contacts which form the slot metamaterial. Selecting them to be 60nm thick was motivated by fabrication concerns with the additional 5nm alumina insulator on top. Thicker metal layers would result in higher aspect ratios of slot metal height to slot width, complicating the lift-off process significantly.

The absorber layer thickness has been selected after fixing the resonator metal thickness. The insulating layer on top of the electrodes forces the current to flow in a lateral direction in the slot, thus the HgTe thickness on top of the electrodes is irrelevant since the photogenerated charge carriers on are not collected at the electrodes. Only the absorber material in the slot contributes to the photoresponse. Ideally, the slot should be completely filled, necessitating the absorber layer to be at least as thick as the metal. Moreover, thin layers typically exhibit fewer cracks and often result in better uniformity. Therefore, it was decided that the active layer should be as thick as the metal layer.

5 Summary & Outlook

This doctoral thesis has explored the development of MIR photodetectors utilizing cQDs integrated with plasmonic metamaterials, addressing the challenges of cost and performance at room temperature operation in traditional photodetection technologies. The materials investigated were PbSe, PbS and HgTe cQDs due to their tunable optical properties and potential for high performance across the MIR spectrum. The achievements of this work can be summarized as followed:

Metamaterial Enhanced Sintered PbSe/PbS Photodetector

A novel method was developed for sintering solution-deposited cQDs into solid polycrystalline layers. This method effectively removed the quantum confinement, enabling MIR photoconductivity, improved carrier transport, and significantly larger photo-gain. Additionally, it facilitated the stacking of two distinct materials to form a heterostructure, which doubled the photoresponse of the device.

These sintered cQD layers were combined with a plasmonic perfect absorber metamaterial to develop a highly responsive mid-infrared photodetector. This integration led to near-unity absorption, tunable across a broad spectral range resulting in a responsivity increase of up to twenty times. Specifically, the photodetector exhibited exceptional responsivity values of 375 A/W at 2710 nm and 4 A/W at 4250 nm. These advancements highlight significant progress in the field of photodetection, leveraging the properties of cQDs and the capabilities of metamaterials.

Metamaterial Engineering for HgTe cQD Photodetector

Electrical and optical simulations were used to improve the design of metamaterials for HgTe cQD photodetectors. The improved designs allowed for enhanced photogenerated carrier collection efficiency by reducing carrier transition times and optimizing the overlap of the externally applied electric field with the regions of strongest absorption in the cQD layer. Additionally, by reducing the active volume of the photoconducting material, it was possible to significantly decrease the noise current spectral density, while maintaining near-unity absorption. The resulting designs also allowed for tunable absorption across a broad spectral range, enhancing the versatility of applications. Ultimately, these improvements resulted in a 13-fold increase in responsivity, reaching 16 A/W, and a 345-fold increase in detectivity, achieving 6×10^8 Jones at a wavelength of 2710 nm.

5 Summary & Outlook

Outlook

Looking ahead, the demonstrated capability to enhance photodetector performance through material and design innovations presents a robust pathway for future advancements. Integrating cQDs with metamaterials presents a powerful approach for developing high-performance MIR photodetectors that function effectively at room temperature.

Future research of cQD materials is anticipated to achieve even higher carrier mobilities and lower noise levels through enhanced defect passivation. In combination with optimally designed metamaterials, these improvements are expected to surpass the performance of current state-of-the-art devices. Additionally, the flexibility of metamaterial designs not only enables their application across various spectral ranges but also allows their integration with diverse materials. This establishes them as a versatile platform for photodetection, capable of meeting a broad spectrum of operational requirements and wavelengths.

In conclusion, this thesis not only demonstrates significant advancements in MIR photodetector performance through the processing and integration of cQDs and metamaterials, but also lays a strong foundation for the future of photodetection technology.

Appendix A Electronic Band Structure

Various electrical and optical characteristics of semiconductors are defined by their electronic band structure. The band structure represents a quasi-continuum of energetic states that can be occupied by charge carriers and are separated by energy gaps. The energy gap between the filled band with highest energy states E_v (valence band) and the energetically closest unfilled band E_c (conduction band) defines the absorption onset in semiconductors. This energy gap is referred to as the band gap E_g of a semiconductor. If a photon with an energy

$$E_{ph} = h \frac{c}{\lambda}, \quad (5.1)$$

greater than the band gap energy interacts with the semiconductor it can be absorbed. In this equation c represents the speed of light, h the Planck constant and λ the wavelength.

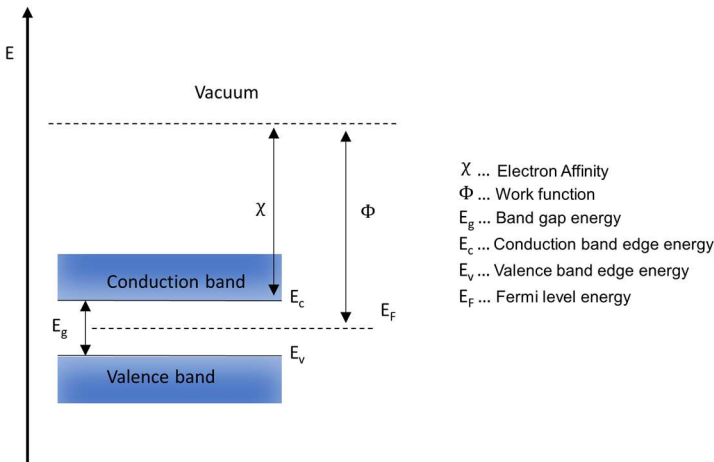


Figure 5.1. Band structure of a semiconductor showing relevant parameters.

An additional important energetic metric is the Fermi level E_F . The Fermi level is in the band theory regarded as a hypothetical energy level. At thermodynamic equilibrium, it represents the energy level at which there is a 50% probability of electron occupancy at any given time. In conductors, the Fermi level falls within the conduction band, allowing electrons to move freely. In insulators and semiconductors, it lies within the band gap,

While the band structure of bulk materials and the corresponding band gap are fundamental attributes, they can be modified by altering the dimensions of the material. Significant variations in the band structure can occur when the dimensions of the semiconductors approach a scale where quantum mechanical effects become relevant, a topic which is discussed in Section 2.2.

Appendix B Metal-Semiconductor Contacts

For semiconductor devices to be electrically operated and characterized they need to be electrically contacted. This is typically achieved by physically connecting them with metals, which are then integrated into the broader circuitry. The interface formed between the semiconductor and the metal plays a crucial role in the operation of the device. These interfaces can be classified into two types: ohmic and Schottky contacts. The type of contact interface is reflected in its current-voltage relationship. Ohmic contacts exhibit a linear current-voltage relationship, while Schottky contacts show a rectifying behavior.

In general, when a metal comes into electrical contact with a semiconductor, the Fermi levels of the two materials must align. If there exists an energetic difference between the Fermi levels of the metal and semiconductor, a redistribution of charge carriers at the interface will occur. This leads to a depletion or accumulation of charge carriers at the interface and bending of the energy bands within the semiconductor, whereas the energy levels in the metals stay unchanged.

The magnitude of the band bending, and subsequent barrier formation determines whether a contact exhibits an ohmic or rectifying behavior. The barrier height for electrons, $\Phi_{B,n}$, and holes, $\Phi_{B,p}$, can be expressed as

$$\Phi_{B,n} = \chi_s - \phi_m + V_d \quad (5.2)$$

$$\Phi_{B,p} = \chi_s - \phi_m - E_G + V_d \quad (5.3)$$

, with χ_s the electron affinity, ϕ_m the metal work function and V_d the applied voltage over the junction. For ohmic contacts the barrier is typically small when no voltage is applied. This enables carriers within the semiconductor to easily enter the metal and carriers to be easily injected into the semiconductor or extracted from the contact depending on the sign of the externally applied bias. There are several processes involved in the carrier injection and extraction when the barrier is small such as quantum tunnelling, thermionic emission and diffusion enabling a large number of carriers to be transported. For Schottky type contacts on the other hand there are large barriers present if no bias is applied. This barrier hinders carriers to be injected and extracted from the semiconductor for small voltages. Depending on the sign and magnitude of the externally applied bias, the barrier will either increase, continuing to block the carriers, or

Appendix B Metal-Semiconductor Contacts

decrease. By applying a bias that reduces the barrier height electrons can overcome the barrier resulting in a current increase exponentially with the applied voltage. This voltage dependence results in the rectifying behavior. The simplified band diagrams for n and p doped semiconductors forming ohmic and Schottky type contacts can be seen in Figure 5.3.

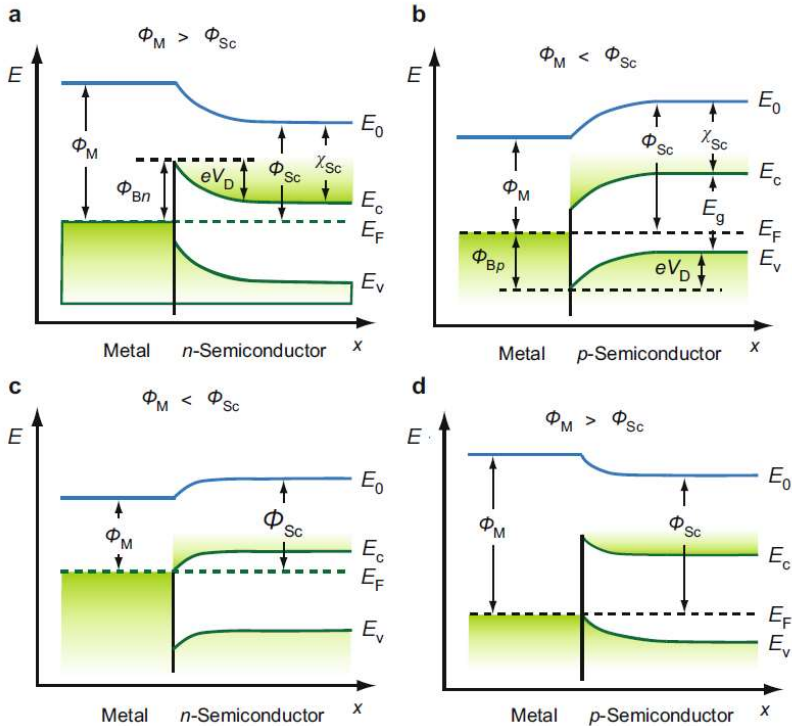


Figure 5.3. Band diagram of a Schottky contact with a metal contacting (a) n-doped semiconductor with a metal work function greater than the semiconductor work function. (b) p-doped semiconductor with a metal work function smaller than the semiconductor work function. (c) n-doped semiconductor with a metal work function smaller than the semiconductor work function. (d) p-doped semiconductor with a metal work function greater than the semiconductor work function. The alignment depicted in (a) and (b) lead to carrier blocking whereas in (c) and (d) charges can be transported. Reprinted with permission from [126]. Copyright Springer International Publishing AG 2018.

The rectifying behavior of metal-semiconductor contacts with moderate barriers arises from thermionic emission processes. In the case of an n-doped semiconductor, electrons possessing sufficient energy are thermally excited, overcoming the energy barrier and thus are transported from the semiconductor into the metal. To maintain charge neutrality, a hole from the metal must diffuse into the semiconductor. This scenario is reversed in the case of a p-doped semiconductor.

The thermionic emission which can be expressed as

$$J = A^* T^2 \cdot e^{-\frac{q\Phi_B}{k_B T}} \left(e^{\frac{eV_{Bias}}{k_B T}} - 1 \right) \quad (5.4)$$

, with A^* the Richardson constant and V_{Bias} the bias voltage.

When it was attempted to verify the Schottky-Mott theory concerning the barrier height, significant deviations between the theoretically predicted barrier height and the experimentally observed height were encountered. For example, in some cases there was hardly any influence of the metal type on the contact characteristics. Bardeen was one of the first to point out this discrepancy. He proposed that surface states pin the Fermi level at a specific energy (Fermi level pinning), therefore making the barrier height independent of the metal.

Appendix B Metal-Semiconductor Contacts

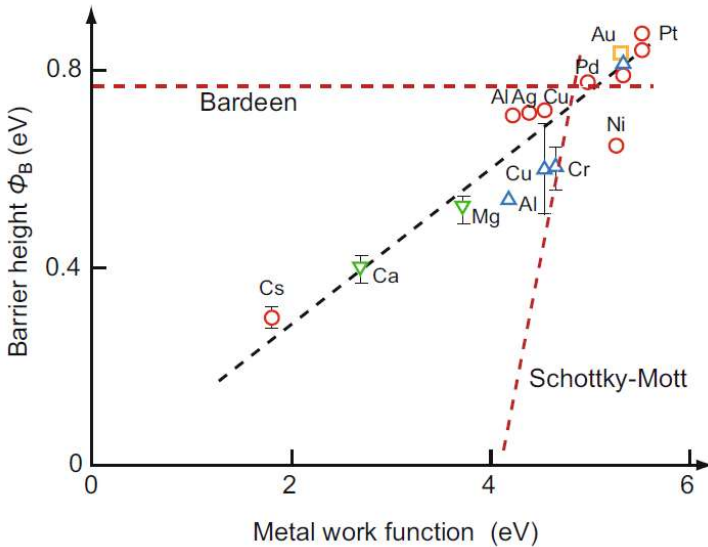


Figure 5.4. Schottky barrier height for a metal-semiconductor contact for silicon and different metals. The red dashed lines show the barrier height according to the model of Bardeen and the Schottky-Mott model. The black dashed line shows a fit in between the limits of the two in red indicated models. Reprinted with permission from [126]. Copyright Springer International Publishing AG 2018.

Subsequent research revealed that the assumption of surface states alone does not fully explain the observed behavior. It was discovered that a linear relationship exists for most semiconductor-metal contacts depending on the metal work function. This linearity falls between the predictions of the Schottky-Mott theory and Bardeen's theory. Figure 5.4 illustrates this linear behavior for silicon. This “intermediate” behavior between the two theories is a result of various effects taking place at the interface, including surface states, dipole formation, alloying and other effects varying for each semiconductor and metal combination.

Appendix C Semiconductor Heterojunction

Like metal-semiconductor interfaces, semiconductor-semiconductor interfaces are present in various devices. Thus, an understanding thereof is of great importance.

Semiconductor band gaps can align in different ways defining their behavior. This alignment can be categorized into three types depending on the band gap offset and magnitude, see Figure 5.5.

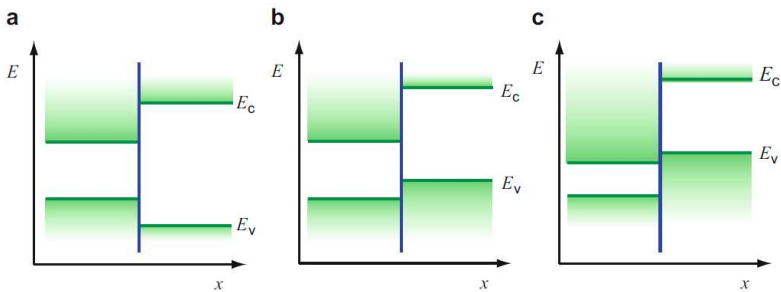


Figure 5.5. Band diagrams of two semiconductors with different band gaps and electron affinities. (a) Straddling gap (type I), (b) Staggered gap (type II), (c) Broken type (type III). Reprinted with permission from [126]. Copyright Springer International Publishing AG 2018.

The band alignment at a semiconductor-semiconductor interface generally follows the same principles as those for metal-semiconductor interfaces, with some notable distinctions. When a metal is brought into contact with a semiconductor and the Fermi level and work function do not align, mainly the band of the semiconductor bends, while the energy levels in the metal remain unchanged due to its high carrier densities. However, in the case of a semiconductor-semiconductor interfaces with different Fermi levels, both bands bend. This band bending leads to a depletion region extending into both semiconductors. A band diagram of a staggered type heterojunction interface can be seen in Figure 5.6.

Appendix C Semiconductor Heterojunction

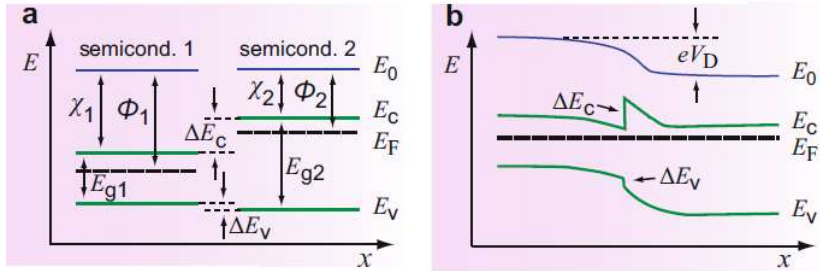


Figure 5.6. (a) Illustration of two semiconductor diagrams with relevant metrics. Showing the individual materials before they come in contact. (b) Illustration of the resulting band diagram of the two semiconductors when they are in contact. Reprinted with permission from [126]. Copyright Springer International Publishing AG 2018.

Various models have been developed to describe and understand the band alignment. They often focus on modeling the band offsets ΔE_v and ΔE_c at the material interface after bringing them into contact. These models utilize either linear or nonlinear approaches. Linear models aim to describe band alignment based on bulk material properties and linear combinations thereof. Nonlinear models, on the other hand, account for additional interface influences such as defects and dipole formations. These nonlinear models provide a more comprehensive understanding of band alignment at heterostructure interfaces, whereas the linear models are typically simpler.

One of the simplest and commonly used linear models for describing band alignment is the Anderson model. It assumes that the interface is an abrupt transition, where strain, interface states and dipole effects will be neglected, as well as effects originating from different crystal orientations. This model uses the electron affinities of the bulk materials to determine the band offset.

$$\Delta E_c = \chi_1 - \chi_2 \quad (5.5)$$

$$\Delta E_v = (\chi_1 + E_{G1}) - (\chi_2 + E_{G2}) \quad (5.6)$$

Although this model is widely and often used, it is known to be inaccurate. It has been shown that experimental results can vary from the theoretical model. However, despite its limitations, the model can still provide valuable initial insights and general information regarding band alignment. More detailed models, linear and non-linear, their description and comparisons can be found in various.

Appendix D Defect Centers in Semiconductors

Defect centers in semiconductors are hardly avoidable and play a critical role in influencing the characteristics and performance of semiconductor devices. They are of great importance for recombination processes which can drastically influence photodetectors. The origin of such defects can vary greatly and can include crystal imperfections, impurities, surface states, and dangling bonds. Understanding and mitigating these defects is crucial for optimizing device functionality across a range of applications.

A common classification for these defects is based on their energetic position relative to the band gap edges. They can be categorized as shallow-level or deep-level defects depending on their proximity to the band edges or the band gap center. Further, an important aspect of the defects are their eigenfunctions and how they interact with the band of the lattice.

Typically, the eigenfunctions of shallow -level defects extend beyond their neighboring atoms and mix with the energetically closest band. This means that they either interact with the valence band or the conduction band. Such shallow defects can be modeled using a quasi-hydrogen approximation.

Deep-level defect centers are characterized by tightly bound electrons localized near the core. Unlike shallow-level defects, the eigenfunctions of deep-level defects can mix with both conduction and valence bands. These deep level defect centers can act as deep traps for either electrons or holes.

Defect Interactions and Metrics

Depending on what type of defect is present in a semiconductor the probability of a charge carrier to interact with defect can vary. A metric used to define this probability is the capture cross-section

$$S_{nonrad} = \pi r_0^2 \tag{5.7}$$

, with r_0 being the radius of the eigenstate at an energy greater than $k_B T$. The probability of capturing a carrier is high if a carrier with an energy smaller than $k_B T$ comes within this radius.

Furthermore, with the capture cross-section it becomes possible to define a lifetime, τ_r , of a carrier. This time is the time between generation and capturing of a carrier in a defect state and defined as

References

$$\tau_r = \frac{1}{v_{rms} s_{nonrad} (N_t - n_n)} \quad (5.8)$$

In this equation v_{rms} represents the average carrier velocity and $(N_t - n_n)$ is the density of unoccupied recombination centers. This equation is of a general character and can be adapted to different recombination processes by introducing different capture cross-sections resulting from the different eigenstate radii and recombination center densities. For example, if a shallow-level trap is modeled utilizing a Hydrogen like approximation the capture cross-section can be defined as

$$s_{HM} = \pi r_{HM}^2 = \frac{q^4}{64\pi(\epsilon_{lattice}\epsilon_o k_B T)^2} \quad (5.9)$$

With $\epsilon_{lattice}$ being the dielectric constant of the host material where the defect is located in.

The definition of the capturing cross-section for deep-level defect is more complex due to the strong coupling between their electron eigenfunctions and lattice oscillations. This coupling can result in oscillations of the surrounding lattice atoms. When this is the case, these oscillations induce changes in the eigenstate of the defects and consequently alter the energy of the defect state. This dynamic interplay results in the defect state energetically fluctuating within the band gap.

Further, an often-used metric in the discussions of recombination process is the capture coefficient c_{trap} . It is a measure of the probability per unit time that a free carrier (electron or hole) will be captured by a trap when it comes into its vicinity. It is essentially a rate constant that describes how effectively a trap captures a carrier and defined as

$$c_{trap} = v_{rms} s_{nonrad} \quad (5.10)$$

By multiplying this capture coefficient with the charge density (n or p) and unoccupied trap density $(N_t - n_n)$ it is possible define the capture rate R_c .

$$R_c = c_{trap} n (N_t - n_n) \quad (5.11)$$

This describes the total rate at which carriers are captured by traps across the entire semiconductor. When discussing the interaction of carriers with defects, it's important to differentiate between trapping and recombining processes. Trapping occurs when a carrier from either the valence or conduction band is captured by a defect state and subsequently

reemitted back into the band from which it originated, typically this involves shallow defects. Recombination, on the other hand, involves the carrier combining with a carrier of the opposite charge and involves deep-level defects.

Carrier Dynamics of Deep -level Defects

Here, a brief introduction to the rate equations of deep level traps is provided giving additional context for discussion of recombination mechanism. While shallow defects, such as impurity doping, are mostly ionized at room temperature, deep levels defects are not, as their binding energy relative to the conduction band or valence band exceeds $k_B T$. Consequently, these deep levels can remain charged with electrons or holes even at room temperature and beyond. Deep-level defects can interact with the valence and conduction band thus it is necessary to introduce capture and emission coefficients for the interaction of electrons from the conduction band with traps, $c_{c,trap}$ and $e_{trap,c}$. Similarly, capture and emission coefficients for holes have to be defined, $c_{trap,v}$ and $e_{v,trap}$. Figure 5.7 illustrates these rates in a simple schematic.

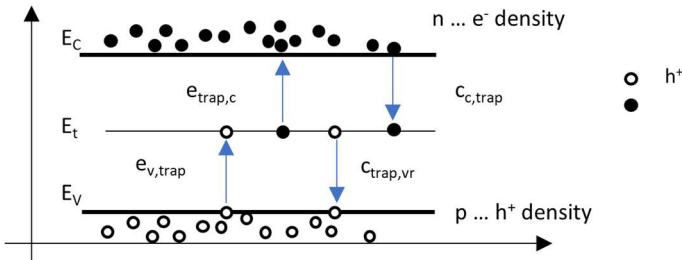


Figure 5.7. Illustration of a band diagram including one type of trap state. In the illustration the possible transitions for electrons from the conduction band and holes from the valence band are shown to and from the trap states, including the variables used to describe their rates.

The population of deep-level traps is determined by the balance between the emission and capture processes of electrons and holes. At the thermal equilibrium, the capture and emission rates of electrons and holes are equal. This leads to the result that the density of filled trap states is constant which can be expressed as

References

$$\frac{dn_n(t)}{dt} = 0 = (c_{c,trap} + c_{trap,v})(N_t - n_n(t)) - (e_{trap,c} + e_{v,trap})n_n(t) \quad (5.12)$$

With this equation, the balanced rate equations, and the consideration that the population of traps follows a Fermi-Dirac distribution, it is possible to express the average trap population as

$$n_n(\infty) = N_t \frac{d_0}{d_1} \frac{1}{1 + e^{\frac{E_t - E_F}{k_B T}}} \quad (5.13)$$

With d_0 being the degeneracy state of an unfilled and d_1 filled defect state, and E_t the trap state energy. Further the emission rates for electrons can be found to be

$$e_{trap,c} = s_{nonrad} v_{rms} N_c \frac{g_0}{g_1} e^{\frac{E_t - E_F}{k_B T}} \quad (5.14)$$

Furthermore, it is possible to use the same formalism and assumptions to derive the hole emission rate.

References

- [1] S. B. William Herschel, "XIV. Experiments on the refrangibility of the invisible rays of the sun," *Philos Trans R Soc Lond*, vol. 90, pp. 284–292, Dec. 1800, doi: 10.1098/RSTL.1800.0015.
- [2] A. Rogalski, "History of infrared detectors," *Opto-Electronics Review*, vol. 20, no. 3, pp. 279–308, Jul. 2012, doi: 10.2478/S11772-012-0037-7/METRICS.
- [3] T. W. Case, "RESISTANCE OIL SUBSTANCES IN LIGHT. NOTES ON THE CHANGE OF RESISTANCE OF CERTAIN SUBSTANCES IN LIGHT. "".
- [4] W. D. Lawson, S. Nielsen, E. H. Putley, and A. S. Young, "Preparation and properties of HgTe and mixed crystals of HgTe-CdTe," *Journal of Physics and Chemistry of Solids*, vol. 9, no. 3–4, pp. 325–329, Mar. 1959, doi: 10.1016/0022-3697(59)90110-6.
- [5] C. Corsi, "Infrared: A key technology for security systems," *Advances in Optical Technologies*, 2012, doi: 10.1155/2012/838752.
- [6] G. R.-Annu. Rev. Astron. Astrophys. and undefined 2007, "Infrared detector arrays for astronomy," *annualreviews.orgGH RiekeAnnu. Rev. Astron. Astrophys., 2007•annualreviews.org*, vol. 45, pp. 77–115, 2007, doi: 10.1146/annurev.astro.44.051905.092436.
- [7] S. Serjeant, M. Elvis, and G. Tinetti, "The future of astronomy with small satellites," *Nature Astronomy 2020 4:11*, vol. 4, no. 11, pp. 1031–1038, Nov. 2020, doi: 10.1038/s41550-020-1201-5.

References

- [8] K. B. Beć, J. Grabska, and C. W. Huck, "Near-Infrared Spectroscopy in Bio-Applications," *Molecules* 2020, Vol. 25, Page 2948, vol. 25, no. 12, p. 2948, Jun. 2020, doi: 10.3390/MOLECULES25122948.
- [9] K. Y. Su and W. L. Lee, "Fourier Transform Infrared Spectroscopy as a Cancer Screening and Diagnostic Tool: A Review and Prospects," *Cancers* 2020, Vol. 12, Page 115, vol. 12, no. 1, p. 115, Jan. 2020, doi: 10.3390/CANCERS12010115.
- [10] Ah. A. H. Abdellatif, H. M. Tawfeek, M. A. Younis, M. Alsharidah, and O. Al Rugaie, "Biomedical Applications of Quantum Dots: Overview, Challenges, and Clinical Potential," *Int J Nanomedicine*, vol. 17, pp. 1951–1970, 2022, doi: 10.2147/IJN.S357980.
- [11] C. Prater *et al.*, "Fluorescently Guided Optical Photothermal Infrared Microspectroscopy for Protein-Specific Bioimaging at Subcellular Level," *J Med Chem*, vol. 66, no. 4, pp. 2542–2549, Feb. 2023, doi: 10.1021/ACS.JMEDCHEM.2C01359/ASSET/IMAGES/LARGE/JM2C01359_0005.JPEG.
- [12] J. Qian, Z. Feng, X. Fan, A. Kuzmin, A. S. L. Gomes, and P. N. Prasad, "High contrast 3-D optical bioimaging using molecular and nanoprobe optically responsive to IR light," *Phys Rep*, vol. 962, pp. 1–107, Jun. 2022, doi: 10.1016/J.PHYSREP.2022.02.004.
- [13] M. J. Walsh, R. K. Reddy, and R. Bhargava, "Label-free biomedical imaging with mid-IR spectroscopy," *IEEE Journal on Selected Topics in Quantum Electronics*, vol. 18, no. 4, pp. 1502–1513, 2012, doi: 10.1109/JSTQE.2011.2182635.
- [14] Y. Luo *et al.*, "Megapixel large-format colloidal quantum-dot infrared imagers with resonant-cavity enhanced

- photoresponse,” *APL Photonics*, vol. 8, no. 5, p. 56109, May 2023, doi: 10.1063/5.0145374/2892296.
- [15] Z. Cheng, T. Zhao, and H. Zeng, “2D Material-Based Photodetectors for Infrared Imaging,” *Small Science*, vol. 2, no. 1, p. 2100051, Jan. 2022, doi: 10.1002/SMSC.202100051.
- [16] E. A. Plis, “InAs/GaSb Type-II Superlattice Detectors,” *Advances in Electronics*, vol. 2014, no. 1, p. 246769, Jan. 2014, doi: 10.1155/2014/246769.
- [17] A. G. U. Perera, “Heterojunction and superlattice detectors for infrared to ultraviolet,” *Prog Quantum Electron*, vol. 48, pp. 1–56, Jul. 2016, doi: 10.1016/J.PQUANTELEC.2016.05.001.
- [18] C. Downs and T. E. Vandervelde, “Progress in Infrared Photodetectors Since 2000,” *Sensors 2013, Vol. 13, Pages 5054-5098*, vol. 13, no. 4, pp. 5054–5098, Apr. 2013, doi: 10.3390/S130405054.
- [19] C. L. Tan and H. Mohseni, “Emerging technologies for high performance infrared detectors,” *Nanophotonics*, vol. 7, no. 1, pp. 169–197, Jan. 2018, doi: 10.1515/nanoph-2017-0061.
- [20] N. Ilyas, D. Li, Y. Song, H. Zhong, Y. Jiang, and W. Li, “Low-Dimensional Materials and State-of-the-Art Architectures for Infrared Photodetection,” *Sensors 2018, Vol. 18, Page 4163*, vol. 18, no. 12, p. 4163, Nov. 2018, doi: 10.3390/S18124163.
- [21] T. Nakotte *et al.*, “Colloidal quantum dot based infrared detectors: extending to the mid-infrared and moving from the lab to the field,” *J Mater Chem C Mater*, vol. 10, no. 3, pp. 790–804, 2022, doi: 10.1039/d1tc05359k.

References

- [22] W. Gong, P. Wang, D. Dai, Z. Liu, L. Zheng, and Y. Zhang, "Infrared colloidal quantum dots for photoelectric conversion devices," *J Mater Chem C Mater*, vol. 9, no. 9, pp. 2994–3025, Mar. 2021, doi: 10.1039/D0TC05902A.
- [23] R. Guo, M. Zhang, J. Ding, A. Liu, F. Huang, and M. Sheng, "Advances in colloidal quantum dot-based photodetectors," *J Mater Chem C Mater*, vol. 10, no. 19, pp. 7404–7422, May 2022, doi: 10.1039/D2TC00219A.
- [24] A. Rogalski, "Progress in Quantum Dot Infrared Photodetectors," pp. 1–74, 2021, doi: 10.1007/978-3-030-74270-6_1.
- [25] R. Chang, H. Yang, Z. Wu, and H. Shen, "Recent advances in mid-infrared photodetection based on colloidal quantum dots: Challenges and possible solutions," *Coord Chem Rev*, vol. 500, p. 215539, Feb. 2024, doi: 10.1016/J.CCR.2023.215539.
- [26] Q. Zhao *et al.*, "Colloidal Quantum Dot Solar Cells: Progressive Deposition Techniques and Future Prospects on Large-Area Fabrication," *Advanced Materials*, vol. 34, no. 17, p. 2107888, Apr. 2022, doi: 10.1002/ADMA.202107888.
- [27] F. P. García de Arquer, D. V. Talapin, V. I. Klimov, Y. Arakawa, M. Bayer, and E. H. Sargent, "Semiconductor quantum dots: Technological progress and future challenges," *Science*, vol. 373, no. 6555, Aug. 2021, doi: 10.1126/SCIENCE.AAZ8541/ASSET/C3AC7CAD-9110-4FD1-85BA-03C145F887FC/ASSETS/IMAGES/LARGE/SCIENCE.AAZ8541-F6.JPG.
- [28] H. Lu, G. M. Carroll, N. R. Neale, and M. C. Beard, "Infrared quantum dots: Progress, challenges, and opportunities," *ACS*

- Nano*, vol. 13, no. 2, pp. 939–953, Jan. 2019, doi: 10.1021/acsnano.8b09815.
- [29] M. Liu, N. Yazdani, M. Yarema, M. Jansen, V. Wood, and E. H. Sargent, “Colloidal quantum dot electronics,” *Nat Electron*, vol. 4, no. 8, pp. 548–558, Aug. 2021, doi: 10.1038/s41928-021-00632-7.
- [30] M. Chen, L. Lu, H. Yu, C. Li, and N. Zhao, “Integration of Colloidal Quantum Dots with Photonic Structures for Optoelectronic and Optical Devices,” *Advanced Science*, vol. 8, no. 18, p. 2101560, Sep. 2021, doi: 10.1002/ADVS.202101560.
- [31] J. Chen and K. Rong, “Nanophotonic devices and circuits based on colloidal quantum dots,” *Mater Chem Front*, vol. 5, no. 12, pp. 4502–4537, Jun. 2021, doi: 10.1039/DOQM01118E.
- [32] E. Cortés *et al.*, “Optical Metasurfaces for Energy Conversion,” *Chem Rev*, vol. 122, no. 19, pp. 15082–15176, Oct. 2022, doi: 10.1021/ACS.CHEMREV.2C00078.
- [33] A. S. Solntsev, G. S. Agarwal, and Y. Y. Kivshar, “Metasurfaces for quantum photonics,” *Nature Photonics* 2021 15:5, vol. 15, no. 5, pp. 327–336, Apr. 2021, doi: 10.1038/s41566-021-00793-z.
- [34] J. Guan, J. E. Park, S. Deng, M. J. H. Tan, J. Hu, and T. W. Odom, “Light-Matter Interactions in Hybrid Material Metasurfaces,” *Chem Rev*, vol. 122, no. 19, pp. 15177–15203, Oct. 2022, doi: 10.1021/ACS.CHEMREV.2C00011/ASSET/IMAGES/LARGE/CR2C00011_0020.JPEG.

References

- [35] C. Yu *et al.*, “Heterojunctions of Mercury Selenide Quantum Dots and Halide Perovskites with High Lattice Matching and Their Photodetection Properties,” *Materials*, vol. 17, no. 8, p. 1864, Apr. 2024, doi: 10.3390/MA17081864/S1.
- [36] X. Zhang, C. Yang, P. Li, S. Chen, Z. Guo, and S. Feng, “Growth of Si/PbS Heterostructure Infrared Photodetectors for NIR Detection,” *ACS Photonics*, vol. 11, no. 3, pp. 1197–1204, Mar. 2024, doi: 10.1021/ACSPHOTONICS.3C01720/ASSET/IMAGES/LARGE/H3C01720_0005.JPEG.
- [37] M. Sulaman *et al.*, “Hybrid Bulk-Heterojunction of Colloidal Quantum Dots and Mixed-Halide Perovskite Nanocrystals for High-Performance Self-Powered Broadband Photodetectors,” *Adv Funct Mater*, vol. 32, no. 28, p. 2201527, Jul. 2022, doi: 10.1002/ADFM.202201527.
- [38] Y. Zhang *et al.*, “Hybrid Quantum Dot/Organic Heterojunction: A Route to Improve Open-Circuit Voltage in PbS Colloidal Quantum Dot Solar Cells,” *ACS Energy Lett*, vol. 5, no. 7, pp. 2335–2342, Jul. 2020, doi: 10.1021/ACSENERGYLETT.0C01136/ASSET/IMAGES/LARGE/N20C01136_0005.JPEG.
- [39] H. Li and Z. Yang, “Recent progress in mid-infrared photodetection devices using 2D/nD (n=0, 1, 2, 3) heterostructures,” *Mater Des*, vol. 225, p. 111446, Jan. 2023, doi: 10.1016/J.MATDES.2022.111446.
- [40] J. Yang *et al.*, “Bi2S3 Electron Transport Layer Incorporation for High-Performance Heterostructure HgTe Colloidal Quantum Dot Infrared Photodetectors,” *ACS Photonics*, vol. 10, no. 7, pp. 2226–2233, Jul. 2023, doi:

10.1021/ACSPHOTONICS.2C01145/ASSET/IMAGES/LARGE/P
H2C01145_0005.JPEG.

- [41] T. Kim, M. L. Kelley, D. Kim, A. B. Greytak, and S. Jeong, "Purification of Colloidal Nanocrystals Along the Road to Highly Efficient Photovoltaic Devices," *International Journal of Precision Engineering and Manufacturing - Green Technology*, vol. 8, no. 4, pp. 1309–1321, Jul. 2021, doi: 10.1007/S40684-020-00231-5/TABLES/1.
- [42] X. Lan, S. Masala, and E. H. Sargent, "Charge-extraction strategies for colloidal quantum dot photovoltaics," *Nature Materials* 2014 13:3, vol. 13, no. 3, pp. 233–240, Feb. 2014, doi: 10.1038/nmat3816.
- [43] S. Shoaee, M. Stolterfoht, and D. Neher, "The Role of Mobility on Charge Generation, Recombination, and Extraction in Polymer-Based Solar Cells," *Adv Energy Mater*, vol. 8, no. 28, p. 1703355, Oct. 2018, doi: 10.1002/AENM.201703355.
- [44] Y. Zhang, G. Wu, F. Liu, C. Ding, Z. Zou, and Q. Shen, "Photoexcited carrier dynamics in colloidal quantum dot solar cells: insights into individual quantum dots, quantum dot solid films and devices," *Chem Soc Rev*, vol. 49, no. 1, pp. 49–84, Jan. 2020, doi: 10.1039/C9CS00560A.
- [45] P. Martyniuk *et al.*, "New concepts in infrared photodetector designs □ APPLIED PHYSICS REVIEWS-FOCUSED REVIEW New concepts in infrared photodetector designs," *Appl. Phys. Rev*, vol. 1, p. 41102, 2014, doi: 10.1063/1.4896193.
- [46] A. Rogalski, P. Martyniuk, M. Kopytko, and W. Hu, "applied sciences Review Trends in Performance Limits of the HOT Infrared Photodetectors," 2021, doi: 10.3390/app11020501.

References

- [47] C. Liu *et al.*, "Silicon/2D-material photodetectors: from near-infrared to mid-infrared," *Light: Science & Applications* 2021 10:1, vol. 10, no. 1, pp. 1–21, Jun. 2021, doi: 10.1038/s41377-021-00551-4.
- [48] R. Chakraborty *et al.*, "Advances in mid-infrared detection and imaging: a key issues review," *Reports on Progress in Physics*, vol. 77, no. 8, p. 082401, Aug. 2014, doi: 10.1088/0034-4885/77/8/082401.
- [49] A. Karim and J. Y. Andersson, "Infrared detectors: Advances, challenges and new technologies," *IOP Conf Ser Mater Sci Eng*, vol. 51, no. 1, p. 012001, Dec. 2013, doi: 10.1088/1757-899X/51/1/012001.
- [50] A. Rogalski *et al.*, "Infrared HOT material systems vs. Law 19 paradigm," *Measurement*, vol. 230, p. 114495, May 2024, doi: 10.1016/J.MEASUREMENT.2024.114495.
- [51] E. R.-C. rendus. Physique and undefined 2003, "Physical frontiers in infrared photo-detectors," *comptes-rendus.academie-sciences E RosencherComptes rendus. Physique, 2003•comptes-rendus.academie-sciences ...*, vol. 4, pp. 1155–1158, 2003, doi: 10.1016/j.crhy.2003.10.023.
- [52] Mohamed. Henini and M. Razeghi, *Handbook of infrared detection technologies*. Elsevier Advanced Technology, 2002. Accessed: Jun. 27, 2024. [Online]. Available: <http://www.sciencedirect.com:5070/book/9781856173889/handbook-of-infra-red-detection-technologies>
- [53] Z. Wu, Y. Ou, M. Cai, Y. Wang, R. Tang, and Y. Xia, "Short-Wave Infrared Photodetectors and Imaging Sensors Based on Lead Chalcogenide Colloidal Quantum Dots," *Adv Opt Mater*, vol. 11, no. 1, p. 2201577, Jan. 2023, doi: 10.1002/ADOM.202201577.

- [54] X. Zhao *et al.*, “Lead Chalcogenide Colloidal Quantum Dots for Infrared Photodetectors,” *Materials 2023, Vol. 16, Page 5790*, vol. 16, no. 17, p. 5790, Aug. 2023, doi: 10.3390/MA16175790.
- [55] H. Dortaj *et al.*, “High-speed and high-precision PbSe/PbI₂ solution process mid-infrared camera,” *Sci Rep*, vol. 11, no. 1, p. 1533, 2021, doi: 10.1038/s41598-020-80847-4.
- [56] M. Dolatyari, A. Rostami, S. Mathur, and A. Klein, “UV/IR Dual-Wavelength Photodetector Design Based on ZnO/PMMA/PbSe Nanocomposites,” *IEEE Trans Nanotechnol*, vol. 17, no. 3, pp. 574–581, May 2018, doi: 10.1109/TNANO.2018.2827201.
- [57] M.-H. Jang *et al.*, “Photoconductive mechanism of IR-sensitive iodized PbSe thin films via strong hole–phonon interaction and minority carrier diffusion,” *Appl Opt*, vol. 59, no. 33, p. 10228, 2020, doi: 10.1364/ao.403641.
- [58] G. Konstantatos and E. H. Sargent, “PbS colloidal quantum dot photoconductive photodetectors: Transport, traps, and gain,” *Appl Phys Lett*, vol. 91, no. 17, 2007, doi: 10.1063/1.2800805.
- [59] X. Ding *et al.*, “In situ synergistic halogen passivation of semiconducting PbS quantum dot inks for efficient photovoltaics †,” vol. 16, p. 5115, 2024, doi: 10.1039/d3nr05951k.
- [60] Q. Hao *et al.*, “Mercury Chalcogenide Colloidal Quantum Dots for Infrared Photodetectors,” *Materials 2023, Vol. 16, Page 7321*, vol. 16, no. 23, p. 7321, Nov. 2023, doi: 10.3390/MA16237321.

References

- [61] C. Gréboval, A. Chu, N. Goubet, C. Livache, S. Ithurria, and E. Lhuillier, “Mercury Chalcogenide Quantum Dots: Material Perspective for Device Integration,” *Chem Rev*, vol. 121, no. 7, pp. 3627–3700, Apr. 2021, doi: 10.1021/ACS.CHEMREV.0C01120/ASSET/IMAGES/LARGE/CR0C01120_0037.JPEG.
- [62] Y. Tian *et al.*, “Mercury chalcogenide colloidal quantum dots for infrared photodetection: from synthesis to device applications,” *Nanoscale*, vol. 15, no. 14, pp. 6476–6504, Apr. 2023, doi: 10.1039/d2nr07309a.
- [63] S. Keuleyan, E. Lhuillier, V. Brajuskovic, and P. Guyot-Sionnest, “Mid-infrared HgTe colloidal quantum dot photodetectors,” *Nature Photonics* 2011 5:8, vol. 5, no. 8, pp. 489–493, Jul. 2011, doi: 10.1038/nphoton.2011.142.
- [64] G. Shen, M. Chen, and P. Guyot-Sionnest, “Synthesis of Nonaggregating HgTe Colloidal Quantum Dots and the Emergence of Air-Stable n-Doping,” *Journal of Physical Chemistry Letters*, vol. 8, no. 10, pp. 2224–2228, May 2017, doi: 10.1021/ACS.JPCLETT.7B00775/ASSET/IMAGES/LARGE/JZ-2017-00775Y_0005.JPEG.
- [65] J. Yang *et al.*, “Ligand-Engineered HgTe Colloidal Quantum Dot Solids for Infrared Photodetectors,” *Nano Lett*, vol. 22, no. 8, pp. 3465–3472, Apr. 2022, doi: 10.1021/ACS.NANOLETT.2C00950/ASSET/IMAGES/MEDIUM/NL2C00950_M003.GIF.
- [66] M. Chen *et al.*, “High Carrier Mobility in HgTe Quantum Dot Solids Improves Mid-IR Photodetectors,” *ACS Photonics*, vol. 6, no. 9, pp. 2358–2365, Sep. 2019, doi: 10.1021/acsp Photonics.9b01050.

- [67] K. A. Sergeeva *et al.*, “Obviating Ligand Exchange Preserves the Intact Surface of HgTe Colloidal Quantum Dots and Enhances Performance of Short Wavelength Infrared Photodetectors,” *Advanced Materials*, vol. 36, no. 17, Apr. 2024, doi: 10.1002/ADMA.202306518.
- [68] M. Chen, X. Xue, T. Qin, C. Wen, Q. Hao, and X. Tang, “Universal Homojunction Design for Colloidal Quantum Dot Infrared Photodetectors,” *Adv Mater Technol*, vol. 8, no. 16, Aug. 2023, doi: 10.1002/ADMT.202300315.
- [69] H. Zhang, J. C. Peterson, A. Caillas, and P. Guyot-Sionnest, “High Mobility HgTe Quantum Dot Films with Small Energy and Dynamic Disorder,” *The Journal of Physical Chemistry C*, vol. 128, no. 16, pp. 6726–6734, Apr. 2024, doi: 10.1021/acs.jpcc.3c07908.
- [70] X. Lan *et al.*, “Quantum dot solids showing state-resolved band-like transport,” *Nat Mater*, vol. 19, no. 3, pp. 323–329, Mar. 2020, doi: 10.1038/s41563-019-0582-2.
- [71] Z. Yang *et al.*, “Mixed-quantum-dot solar cells,” *Nat Commun*, vol. 8, no. 1, 2017, doi: 10.1038/s41467-017-01362-1.
- [72] A. Chu *et al.*, “Infrared photoconduction at the diffusion length limit in HgTe nanocrystal arrays,” *Nat Commun*, vol. 12, no. 1, p. 1794, Dec. 2021, doi: 10.1038/s41467-021-21959-x.
- [73] X. Xue, M. Chen, Y. Luo, T. Qin, X. Tang, and Q. Hao, “High-operating-temperature mid-infrared photodetectors via quantum dot gradient homojunction,” *Light Sci Appl*, vol. 12, no. 1, p. 2, Jan. 2023, doi: 10.1038/s41377-022-01014-0.

References

- [74] X. Tang, M. M. Ackerman, and P. Guyot-Sionnest, "Thermal Imaging with Plasmon Resonance Enhanced HgTe Colloidal Quantum Dot Photovoltaic Devices," *ACS Nano*, vol. 12, no. 7, pp. 7362–7370, Jul. 2018, doi: 10.1021/acsnano.8b03871.
- [75] Y. Yifat, M. Ackerman, and P. Guyot-Sionnest, "Mid-IR colloidal quantum dot detectors enhanced by optical nano-antennas," *Appl Phys Lett*, vol. 110, no. 4, p. 41106, Jan. 2017, doi: 10.1063/1.4975058.
- [76] M. Chen *et al.*, "Photocurrent Enhancement of HgTe Quantum Dot Photodiodes by Plasmonic Gold Nanorod Structures," *ACS Nano*, vol. 8, no. 8, pp. 8208–8216, Aug. 2014, doi: 10.1021/nn502510u.
- [77] T. H. Dang *et al.*, "Nanocrystal-Based Active Photonics Device through Spatial Design of Light-Matter Coupling," *ACS Photonics*, vol. 9, no. 7, pp. 2528–2535, Jul. 2022, doi: 10.1021/acsp Photonics.2c00738.
- [78] C. Dabard *et al.*, "Electroluminescence and Plasmon-Assisted Directional Photoluminescence from 2D HgTe Nanoplatelets," *Journal of Physical Chemistry C*, vol. 127, no. 30, pp. 14847–14855, Aug. 2023, doi: 10.1021/ACS.JPCC.3C04126/ASSET/IMAGES/LARGE/JP3C04126_0005.JPEG.
- [79] T. H. Dang *et al.*, "Broadband Enhancement of Mid-Wave Infrared Absorption in a Multi-Resonant Nanocrystal-Based Device," *Adv Opt Mater*, vol. 10, no. 9, May 2022, doi: 10.1002/ADOM.202200297.
- [80] K. A. Sergeeva *et al.*, "Laser-Printed Plasmonic Metasurface Supporting Bound States in the Continuum Enhances and Shapes Infrared Spontaneous Emission of Coupled HgTe

- Quantum Dots,” *Adv Funct Mater*, vol. 33, no. 44, Oct. 2023, doi: 10.1002/ADFM.202307660.
- [81] X. Yu *et al.*, “Narrow bandgap oxide nanoparticles coupled with graphene for high performance mid-infrared photodetection,” *Nat Commun*, vol. 9, no. 1, pp. 1–8, Oct. 2018, doi: 10.1038/s41467-018-06776-z.
- [82] P. Guyot-Sionnest and J. A. Roberts, “Background limited mid-infrared photodetection with photovoltaic HgTe colloidal quantum dots,” *Appl Phys Lett*, vol. 107, no. 25, Dec. 2015, doi: 10.1063/1.4938135.
- [83] M. J. Grotevent *et al.*, “Colloidal HgTe Quantum Dot/Graphene Phototransistor with a Spectral Sensitivity Beyond 3 μm ,” *Advanced Science*, vol. 8, no. 6, Mar. 2021, doi: 10.1002/advs.202003360.
- [84] U. N. Noubé *et al.*, “Reconfigurable 2D/0D p-n Graphene/HgTe Nanocrystal Heterostructure for Infrared Detection,” *ACS Nano*, vol. 14, no. 4, pp. 4567–4576, Apr. 2020, doi: 10.1021/acsnano.0c00103.
- [85] N. Huo, S. Gupta, and G. Konstantatos, “MoS₂–HgTe Quantum Dot Hybrid Photodetectors beyond 2 μm ,” *Advanced Materials*, vol. 29, no. 17, May 2017, doi: 10.1002/adma.201606576.
- [86] R. D. Septianto *et al.*, “Enabling metallic behaviour in two-dimensional superlattice of semiconductor colloidal quantum dots,” *Nature Communications 2023 14:1*, vol. 14, no. 1, pp. 1–10, May 2023, doi: 10.1038/s41467-023-38216-y.
- [87] J. Pinna *et al.*, “Approaching Bulk Mobility in PbSe Colloidal Quantum Dots 3D Superlattices,” *Advanced Materials*, vol.

References

- 35, no. 8, p. 2207364, Feb. 2023, doi: 10.1002/adma.202207364.
- [88] J. Zha *et al.*, “Infrared Photodetectors Based on 2D Materials and Nanophotonics,” *Adv Funct Mater*, vol. 32, no. 15, p. 2111970, Apr. 2022, doi: 10.1002/ADFM.202111970.
- [89] X. Guan *et al.*, “Recent Progress in Short- to Long-Wave Infrared Photodetection Using 2D Materials and Heterostructures,” *Adv Opt Mater*, vol. 9, no. 4, Feb. 2021, doi: 10.1002/ADOM.202001708.
- [90] M. Long *et al.*, “Room temperature high-detectivity mid-infrared photodetectors based on black arsenic phosphorus,” *Sci Adv*, vol. 3, no. 6, Jun. 2017, doi: 10.1126/SCIADV.1700589/SUPPL_FILE/1700589_SM.PDF.
- [91] J. Bullock *et al.*, “Polarization-resolved black phosphorus/molybdenum disulfide mid-wave infrared photodiodes with high detectivity at room temperature,” *Nature Photonics* 2018 12:10, vol. 12, no. 10, pp. 601–607, Aug. 2018, doi: 10.1038/s41566-018-0239-8.
- [92] P. Tian *et al.*, “Ultrasensitive broadband photodetectors based on two-dimensional Bi₂O₂Te films,” *J Mater Chem C Mater*, vol. 9, no. 39, pp. 13713–13721, Oct. 2021, doi: 10.1039/D1TC02877D.
- [93] M. Long *et al.*, “Palladium diselenide long-wavelength infrared photodetector with high sensitivity and stability,” *ACS Nano*, vol. 13, no. 2, pp. 2511–2519, Feb. 2019, doi: 10.1021/ACS.NANO.8B09476/ASSET/IMAGES/LARGE/NN-2018-09476H_0004.JPEG.
- [94] X. Yu *et al.*, “Atomically thin noble metal dichalcogenide: a broadband mid-infrared semiconductor,” *Nature*

- Communications 2018 9:1*, vol. 9, no. 1, pp. 1–9, Apr. 2018, doi: 10.1038/s41467-018-03935-0.
- [95] A. Rogalski, M. Kopytko, W. Hu, and P. Martyniuk, “Infrared HOT Photodetectors: Status and Outlook,” *Sensors*, vol. 23, no. 17, p. 7564, Aug. 2023, doi: 10.3390/s23177564.
- [96] F. Wang, T. Zhang, R. Xie, Z. Wang, and W. Hu, “How to characterize figures of merit of two-dimensional photodetectors,” *Nature Communications 2023 14:1*, vol. 14, no. 1, pp. 1–9, Apr. 2023, doi: 10.1038/s41467-023-37635-1.
- [97] F. Wang *et al.*, “2D Metal Chalcogenides for IR Photodetection,” *Small*, vol. 15, no. 30, Jul. 2019, doi: 10.1002/SMLL.201901347.
- [98] J. An *et al.*, “Research development of 2D materials based photodetectors towards mid-infrared regime,” *Nano Select*, vol. 2, no. 3, pp. 527–540, Mar. 2021, doi: 10.1002/NANO.202000237.
- [99] G. Liang, X. Yu, X. Hu, B. Qiang, C. Wang, and Q. J. Wang, “Mid-infrared photonics and optoelectronics in 2D materials,” *Materials Today*, vol. 51, pp. 294–316, Dec. 2021, doi: 10.1016/J.MATTOD.2021.09.021.
- [100] A. Rogalski, “HgCdTe infrared detector material: History, status and outlook,” *Reports on Progress in Physics*, vol. 68, no. 10, pp. 2267–2336, 2005, doi: 10.1088/0034-4885/68/10/R01.
- [101] M. C. Gupta, J. T. Harrison, and M. T. Islam, “Photoconductive PbSe thin films for infrared imaging,” *Mater Adv*, vol. 2, no. 10, pp. 3133–3160, May 2021, doi: 10.1039/d0ma00965b.

References

- [102] S. Ganguly, M. H. Jang, Y. Tan, S. S. Yoo, M. C. Gupta, and A. W. Ghosh, "A multiscale materials-to-systems modeling of polycrystalline PbSe photodetectors," *J Appl Phys*, vol. 126, no. 14, p. 143103, Oct. 2019, doi: 10.1063/1.5087818.
- [103] J. T. Harrison and M. C. Gupta, "Mechanistic studies of oxidation and iodization of PbSe thin film sensitization for mid-infrared detection," *J Appl Phys*, vol. 131, no. 2, Jan. 2022, doi: 10.1063/5.0077053.
- [104] M. Kopytko and A. Rogalski, "New insights into the ultimate performance of HgCdTe photodiodes," *Sens Actuators A Phys*, vol. 339, p. 113511, Jun. 2022, doi: 10.1016/J.SNA.2022.113511.
- [105] A. Rogalski, P. Martyniuk, M. Kopytko, P. Madejczyk, and S. Krishna, "InAsSb-Based Infrared Photodetectors: Thirty Years Later On," *Sensors 2020, Vol. 20, Page 7047*, vol. 20, no. 24, p. 7047, Dec. 2020, doi: 10.3390/S20247047.
- [106] L. Lei *et al.*, "Midwavelength interband cascade infrared photodetectors with superlattice absorbers and gain," <https://doi.org/10.1117/1.OE.57.1.011006>, vol. 57, no. 1, p. 011006, Sep. 2017, doi: 10.1117/1.OE.57.1.011006.
- [107] W. Huang *et al.*, "Current-matching versus non-current-matching in long wavelength interband cascade infrared photodetectors," *J Appl Phys*, vol. 122, no. 8, Aug. 2017, doi: 10.1063/1.4989382/394846.
- [108] W. Huang *et al.*, "Electrical gain in interband cascade infrared photodetectors," *J Appl Phys*, vol. 123, no. 11, Mar. 2018, doi: 10.1063/1.5019019/155273.
- [109] A. Rogalski, P. Martyniuk, and M. Kopytko, "Type-II superlattice photodetectors versus HgCdTe photodiodes,"

- Prog Quantum Electron*, vol. 68, p. 100228, Nov. 2019, doi: 10.1016/j.pquantelec.2019.100228.
- [110] S. Fusetto, A. Aprile, P. Malcovati, and E. Bonizzoni, "Readout IC Architectures and Strategies for Uncooled Micro-Bolometers Infrared Focal Plane Arrays: A Review," *Sensors* 2023, Vol. 23, Page 2727, vol. 23, no. 5, p. 2727, Mar. 2023, doi: 10.3390/S23052727.
- [111] L. Yu, Y. Guo, H. Zhu, M. Luo, P. Han, and X. Ji, "Low-Cost Microbolometer Type Infrared Detectors," *Micromachines* 2020, Vol. 11, Page 800, vol. 11, no. 9, p. 800, Aug. 2020, doi: 10.3390/M11090800.
- [112] S. Ben Mbarek, N. Alcheikh, and M. I. Younis, "Recent advances on MEMS based Infrared Thermopile detectors," *Microsystem Technologies*, vol. 28, no. 8, pp. 1751–1764, Aug. 2022, doi: 10.1007/S00542-022-05306-8/TABLES/3.
- [113] Y. Zhu, H. Xu, P. Yu, and Z. Wang, "Engineering plasmonic hot carrier dynamics toward efficient photodetection," *Appl Phys Rev*, vol. 8, no. 2, p. 21305, Jun. 2021, doi: 10.1063/5.0029050/933269.
- [114] C. Zhang, Y. Luo, S. A. Maier, and X. Li, "Recent Progress and Future Opportunities for Hot Carrier Photodetectors: From Ultraviolet to Infrared Bands," *Laser Photon Rev*, vol. 16, no. 6, p. 2100714, Jun. 2022, doi: 10.1002/LPOR.202100714.
- [115] S. Jha, P. Mathur, S. Ramteke, and N. K. Jain, "Pharmaceutical potential of quantum dots," *Artif Cells Nanomed Biotechnol*, vol. 46, no. sup1, pp. 57–65, Oct. 2018, doi: 10.1080/21691401.2017.1411932.
- [116] B. Mishra, B. B. Patel, and S. Tiwari, "Colloidal nanocarriers: a review on formulation technology, types and applications

References

- toward targeted drug delivery," *Nanomedicine*, vol. 6, no. 1, pp. 9–24, Feb. 2010, doi: 10.1016/J.NANO.2009.04.008.
- [117] X. Wang, G. Sun, N. Li, and P. Chen, "Quantum dots derived from two-dimensional materials and their applications for catalysis and energy," *Chem Soc Rev*, vol. 45, no. 8, pp. 2239–2262, Apr. 2016, doi: 10.1039/C5CS00811E.
- [118] Y. Jiang and E. A. Weiss, "Colloidal Quantum Dots as Photocatalysts for Triplet Excited State Reactions of Organic Molecules," *J Am Chem Soc*, vol. 142, no. 36, pp. 15219–15229, Sep. 2020, doi: 10.1021/JACS.0C07421/ASSET/IMAGES/LARGE/JA0C07421_0004.JPEG.
- [119] D. Y. Wang, Y. Y. Yin, C. W. Feng, Rukhsana, and Y. M. Shen, "Advances in Homogeneous Photocatalytic Organic Synthesis with Colloidal Quantum Dots," *Catalysts 2021, Vol. 11, Page 275*, vol. 11, no. 2, p. 275, Feb. 2021, doi: 10.3390/CATAL11020275.
- [120] E. A. Weiss, "Designing the surfaces of semiconductor quantum dots for colloidal photocatalysis," *ACS Energy Lett*, vol. 2, no. 5, pp. 1005–1013, May 2017, doi: 10.1021/ACSENERGYLETT.7B00061/ASSET/IMAGES/LARGE/NZ-2017-00061K_0007.JPEG.
- [121] A. P. Litvin, I. V. Martynenko, F. Purcell-Milton, A. V. Baranov, A. V. Fedorov, and Y. K. Gun'Ko, "Colloidal quantum dots for optoelectronics," *J Mater Chem A Mater*, vol. 5, no. 26, pp. 13252–13275, Jul. 2017, doi: 10.1039/C7TA02076G.
- [122] C. R. Kagan, E. Lifshitz, E. H. Sargent, and D. V. Talapin, "Building devices from colloidal quantum dots," *Science (1979)*, vol. 353, no. 6302, Aug. 2016, doi: 10.1126/science.aac5523.

- [123] S. O. Kasap, *Photoconductivity and Photoconductive Materials*, vol. 1–2. Wiley, 2022. doi: 10.1002/9781119579182.
- [124] M. Brinza, J. Willekens, M. L. Benkhedir, E. V. Emelianova, and G. J. Adriaenssens, “Photoconductivity methods in materials research,” *Journal of Materials Science: Materials in Electronics*, vol. 16, no. 11–12, pp. 703–713, Nov. 2005, doi: 10.1007/S10854-005-4972-7/METRICS.
- [125] Z. Jakšić, “Micro and nanophotonics for semiconductor infrared detectors: Towards an ultimate uncooled device,” *Micro and Nanophotonics for Semiconductor Infrared Detectors: Towards an Ultimate Uncooled Device*, vol. 9783319096742, pp. 1–258, Sep. 2014, doi: 10.1007/978-3-319-09674-2/COVER.
- [126] K. W. Böer and U. W. Pohl, “Semiconductor Physics,” *Semiconductor Physics*, vol. 1–2, pp. 1–1419, Feb. 2023, doi: 10.1007/978-3-031-18286-0/COVER.
- [127] J. Chu and A. Sher, “Device Physics of Narrow Gap Semiconductors,” *Device Physics of Narrow Gap Semiconductors*, 2010, doi: 10.1007/978-1-4419-1040-0.
- [128] G. Konstantatos and E. H. Sargent, *Colloidal quantum dot optoelectronics and photovoltaics*, vol. 9780521198. Cambridge University Press, 2010. doi: 10.1017/CBO9781139022750.
- [129] S. O. Kasap, “Photoconductivity and Photoconductive Materials: Fundamentals, Techniques and Applications: Volume 1 and 2,” *Photoconductivity and Photoconductive Materials: Fundamentals, Techniques and Applications: Volume 1 and 2*, vol. 1–2, pp. 1–868, Jan. 2022, doi: 10.1002/9781119579182.

References

- [130] C. H. Henry and D. V. Lang, "Nonradiative capture and recombination by multiphonon emission in GaAs and GaP," *Phys Rev B*, vol. 15, no. 2, pp. 989–1016, Jan. 1977, doi: 10.1103/PhysRevB.15.989.
- [131] A. L. Efros, "Nanocrystal Quantum Dots," *Nanocrystal Quantum Dots, Second Edition*, pp. 97–132, 2003, Accessed: Jun. 28, 2024. [Online]. Available: <https://www.taylorfrancis.com/chapters/edit/10.1201/9780203913260-10/fine-structure-polarization-properties-band-edge-excitions-semiconductor-nanocrystals>
- [132] Z. Peng Yu and M. Wang, *Quantum Dot Optoelectronic Devices*, vol. 27. in *Lecture Notes in Nanoscale Science and Technology*, vol. 27. Cham: Springer International Publishing, 2020. doi: 10.1007/978-3-030-35813-6.
- [133] S. G. Kwon and T. Hyeon, "Formation mechanisms of uniform nanocrystals via hot-injection and heat-up methods," *Small*, vol. 7, no. 19, pp. 2685–2702, Oct. 2011, doi: 10.1002/SMLL.201002022.
- [134] V. K. Lamer and R. H. Dinegar, "Theory, Production and Mechanism of Formation of Monodispersed Hydrosols", Accessed: Jun. 28, 2024. [Online]. Available: <https://pubs.acs.org/sharingguidelines>
- [135] M. Liu, G. Tang, Y. Liu, and F. L. Jiang, "Ligand Exchange of Quantum Dots: A Thermodynamic Perspective," *Journal of Physical Chemistry Letters*, vol. 15, no. 7, pp. 1975–1984, Feb. 2024, doi: 10.1021/ACS.JPCLETT.3C03413.
- [136] O. E. Semonin, J. M. Luther, and M. C. Beard, "Quantum dots for next-generation photovoltaics," *Materials Today*, vol. 15, no. 11, pp. 508–515, Nov. 2012, doi: 10.1016/S1369-7021(12)70220-1.

- [137] L. Brus, "Electronic wave functions in semiconductor clusters: Experiment and theory," *Journal of Physical Chemistry*, vol. 90, no. 12, pp. 2555–2560, 1986, doi: 10.1021/J100403A003/ASSET/J100403A003.FP.PNG_V03.
- [138] L. E. Brus, "Electron-electron and electron-hole interactions in small semiconductor crystallites: The size dependence of the lowest excited electronic state," *J Chem Phys*, vol. 80, no. 9, pp. 4403–4409, 1984, doi: 10.1063/1.447218.
- [139] P. R. Brown *et al.*, "Energy level modification in lead sulfide quantum dot thin films through ligand exchange," *ACS Nano*, vol. 8, no. 6, pp. 5863–5872, Jun. 2014, doi: 10.1021/NN500897C/SUPPL_FILE/NN500897C_SI_001.PDF.
- [140] C. R. Kagan and C. B. Murray, "Charge transport in strongly coupled quantum dot solids," *Nature Nanotechnology 2015 10:12*, vol. 10, no. 12, pp. 1013–1026, Nov. 2015, doi: 10.1038/nnano.2015.247.
- [141] K. V. Vokhmintcev, P. S. Samokhvalov, and I. Nabiev, "Charge transfer and separation in photoexcited quantum dot-based systems," *Nano Today*, vol. 11, no. 2, pp. 189–211, Apr. 2016, doi: 10.1016/J.NANTOD.2016.04.005.
- [142] "Nano Express TOPICAL REVIEW • OPEN ACCESS Recent progress in photovoltaic and thermoelectric applications of coupled colloidal quantum dot solids: insights into charge transport fundamentals," 2024, doi: 10.1088/2632-959X/ad2b7e.
- [143] P. Guyot-Sionnest, "Electrical transport in colloidal quantum dot films," May 03, 2012, *American Chemical Society*. doi: 10.1021/jz300048y.

References

- [144] B. Shklovskii and A. Efros, *Electronic properties of doped semiconductors*, vol. 45. in Springer Series in Solid-State Sciences, vol. 45. Berlin, Heidelberg: Springer Berlin Heidelberg, 1984. doi: 10.1007/978-3-662-02403-4.
- [145] D. Yu, C. Wang, B. L. Wehrenberg, and P. Guyot-Sionnest, "Variable range hopping conduction in semiconductor nanocrystal solids," *Phys Rev Lett*, vol. 92, no. 21, p. 216802, May 2004, doi: 10.1103/PhysRevLett.92.216802.
- [146] N. Dordevic, "Colloidal Quantum Dot Absorption and Luminescence for Optoelectronics: From Machine Learning to Plasmonic-Enhanced Devices," Sep. 2021, doi: 10.3929/ETHZ-B-000503335.
- [147] N. Yazdani *et al.*, "Charge transport in semiconductors assembled from nanocrystal quantum dots," *Nat Commun*, vol. 11, no. 1, pp. 1–9, Jun. 2020, doi: 10.1038/s41467-020-16560-7.
- [148] A. Shabaev, A. L. Efros, and A. L. Efros, "Dark and photo-conductivity in ordered array of nanocrystals," *Nano Lett*, vol. 13, no. 11, pp. 5454–5461, Nov. 2013, doi: 10.1021/nl403033f.
- [149] B. E. A. Saleh and M. C. Teich, "Fundamentals of Photonics," Aug. 1991, doi: 10.1002/0471213748.
- [150] R. Alaee, M. Albooyeh, and C. Rockstuhl, "Theory of metasurface based perfect absorbers," *J Phys D Appl Phys*, vol. 50, no. 50, p. 503002, Nov. 2017, doi: 10.1088/1361-6463/AA94A8.
- [151] S. A. Maier, "Plasmonics: Fundamentals and applications," *Plasmonics: Fundamentals and Applications*, pp. 1–223, 2007, doi: 10.1007/0-387-37825-1/COVER.

- [152] W. Cai and V. Shalaev, "Optical metamaterials: Fundamentals and applications," *Optical Metamaterials: Fundamentals and Applications*, pp. 1–200, 2010, doi: 10.1007/978-1-4419-1151-3/COVER.
- [153] A. Lochbaum, "Metamaterial-Based Mid-Infrared Gas Sensing," *ETH Zürich Series in Electromagnetic Fields*, vol. 15, Aug. 2020, doi: 10.3929/ETHZ-B-000431783.
- [154] A. Tittl *et al.*, "A Switchable Mid-Infrared Plasmonic Perfect Absorber with Multispectral Thermal Imaging Capability," *Advanced Materials*, vol. 27, no. 31, pp. 4597–4603, Aug. 2015, doi: 10.1002/ADMA.201502023.
- [155] J. A. Bossard, L. Lin, S. Yun, L. Liu, D. H. Werner, and T. S. Mayer, "Near-ideal optical metamaterial absorbers with super-octave bandwidth," *ACS Nano*, vol. 8, no. 2, pp. 1517–1524, Feb. 2014, doi: 10.1021/NN4057148.
- [156] W. Li *et al.*, "Refractory Plasmonics with Titanium Nitride: Broadband Metamaterial Absorber," *Adv. Mater*, 2014, doi: 10.1002/adma.201401874.
- [157] J. Hodgkinson and R. P. Tatam, "Optical gas sensing: A review," *Meas Sci Technol*, vol. 24, no. 1, p. 012004, Jan. 2013, doi: 10.1088/0957-0233/24/1/012004.
- [158] A. Lochbaum *et al.*, "Compact Mid-Infrared Gas Sensing Enabled by an All-Metamaterial Design," *Nano Lett*, vol. 20, no. 6, pp. 4169–4176, Jun. 2020, doi: 10.1021/acs.nanolett.0c00483.
- [159] F. Zhuge *et al.*, "Nanostructured Materials and Architectures for Advanced Infrared Photodetection," *Adv Mater Technol*, vol. 2, no. 8, p. 1700005, Aug. 2017, doi: 10.1002/admt.201700005.

References

- [160] H. Altug, S. H. Oh, S. A. Maier, and J. Homola, “Advances and applications of nanophotonic biosensors,” *Nat Nanotechnol*, vol. 17, no. 1, pp. 5–16, Jan. 2022, doi: 10.1038/s41565-021-01045-5.
- [161] M. Hermes *et al.*, “Mid-IR hyperspectral imaging for label-free histopathology and cytology,” *Journal of Optics (United Kingdom)*, vol. 20, no. 2, p. 023002, Feb. 2018, doi: 10.1088/2040-8986/aaa36b.
- [162] M. Vainio and L. Halonen, “Mid-infrared optical parametric oscillators and frequency combs for molecular spectroscopy,” *Physical Chemistry Chemical Physics*, vol. 18, no. 6, pp. 4266–4294, 2016, doi: 10.1039/c5cp07052j.
- [163] J. Tang and E. H. Sargent, “Infrared colloidal quantum dots for photovoltaics: Fundamentals and recent progress,” *Advanced Materials*, vol. 23, no. 1, pp. 12–29, Jan. 2011, doi: 10.1002/adma.201001491.
- [164] N. Moody *et al.*, “Decreased Synthesis Costs and Waste Product Toxicity for Lead Sulfide Quantum Dot Ink Photovoltaics,” *Adv Sustain Syst*, vol. 3, no. 10, Oct. 2019, doi: 10.1002/adsu.201900061.
- [165] L. Feng, P. Huo, Y. Liang, and T. Xu, “Photonic Metamaterial Absorbers: Morphology Engineering and Interdisciplinary Applications,” *Advanced Materials*, vol. 32, no. 27, p. 1903787, Sep. 2020, doi: 10.1002/adma.201903787.
- [166] A. Dorodnny, S. M. Koepfli, A. Lochbaum, and J. Leuthold, “Design of CMOS-compatible metal–insulator–metal metasurfaces via extended equivalent-circuit analysis,” *Sci Rep*, vol. 10, no. 1, p. 17941, Dec. 2020, doi: 10.1038/s41598-020-74849-5.

- [167] H. Fang and W. Hu, "Photogating in Low Dimensional Photodetectors," *Advanced Science*, vol. 4, no. 12, Dec. 2017, doi: 10.1002/advs.201700323.
- [168] K. S. Novoselov, A. Mishchenko, A. Carvalho, and A. H. Castro Neto, "2D materials and van der Waals heterostructures," *Science (1979)*, vol. 353, no. 6298, Jul. 2016, doi: 10.1126/science.aac9439.
- [169] M. Liu *et al.*, "Highly sensitive, broad-band organic photomultiplication-type photodetectors covering UV-Vis-NIR \dagger ," *J. Mater. Chem. C*, vol. 9, pp. 6357–6364, 2021, doi: 10.1039/d1tc00555c.
- [170] Z. Zhao *et al.*, "Filter-Free Narrowband Photomultiplication-Type Planar Heterojunction Organic Photodetectors," *Adv Funct Mater*, 2022, doi: 10.1002/ADFM.202212149.
- [171] A. Zavabeti, A. Jannat, L. Zhong, A. A. Haidry, Z. Yao, and J. Z. Ou, "Two-Dimensional Materials in Large-Areas: Synthesis, Properties and Applications," *Nanomicro Lett*, vol. 12, no. 1, pp. 66–66, 2020, doi: 10.1007/s40820-020-0402-x.
- [172] U. Koch *et al.*, "A monolithic bipolar CMOS electronic–plasmonic high-speed transmitter," *Nature Electronics 2020 3:6*, vol. 3, no. 6, pp. 338–345, Jun. 2020, doi: 10.1038/s41928-020-0417-9.
- [173] J. Qiu, Y. Liu, G. Zhang, K. Shi, Y. Li, and Y. Luo, "Modified vapor phase deposition technology for high-performance uncooled MIR PbSe detectors," *RSC Adv*, vol. 11, no. 55, pp. 34908–34914, Oct. 2021, doi: 10.1039/d1ra06144e.
- [174] B. Weng, J. Qiu, Z. Yuan, P. R. Larson, G. W. Strout, and Z. Shi, "Responsivity enhancement of mid-infrared PbSe detectors using CaF₂ nano-structured antireflective coatings," *Appl*

References

- Phys Lett*, vol. 104, no. 2, p. 021109, Jan. 2014, doi: 10.1063/1.4861186.
- [175] M.-H. Jang, M. T. Kramer, S.-S. Yoo, and M. C. Gupta, "Laser annealing to improve PbSe thin film photosensitivity and specific detectivity," *Appl Opt*, vol. 59, no. 30, p. 9409, Oct. 2020, doi: 10.1364/ao.401535.
- [176] M. Dolatyari, A. Rostami, S. Mathur, and A. Klein, "Trap engineering in solution processed PbSe quantum dots for high-speed MID-infrared photodetectors," *J Mater Chem C Mater*, vol. 7, no. 19, pp. 5658–5669, 2019, doi: 10.1039/c8tc06093b.
- [177] A. Efros, "Interband light absorption in semiconductor spheres," *Soviet physics. Semiconductors*, vol. 16, no. 7, pp. 772–775, 1982.
- [178] F. W. Wise, "Lead salt quantum dots: The limit of strong quantum confinement," *Acc Chem Res*, vol. 33, no. 11, pp. 773–780, 2000, doi: 10.1021/ar970220q.
- [179] S. Adachi, *Optical Constants of Crystalline and Amorphous Semiconductors*. Boston, MA: Springer US, 1999. doi: 10.1007/978-1-4615-5247-5.
- [180] U. Schlichting and K. H. Gobrecht, "The mobility of free carriers in PbSe crystals," *Journal of Physics and Chemistry of Solids*, vol. 34, no. 4, pp. 753–758, 1973, doi: 10.1016/S0022-3697(73)80183-0.
- [181] R. Dalven, "A review of the semiconductor properties of PbTe, PbSe, PbS and PbO," *Infrared Phys*, vol. 9, no. 4, pp. 141–184, Dec. 1969, doi: 10.1016/0020-0891(69)90022-0.

- [182] R. A. Knapp, D. of Zhyst, V. of Rochester, and P. Irorh, "DE HAAS-SHUBNI KOV EFFE CT IN Sb Photoelectric Properties of Lead Sulfide in the Near and Vacuum Ultraviolet*," vol. 132, no. 5, 1963.
- [183] S. H. Wei and A. Zunger, "Electronic and structural anomalies in lead chalcogenides," *Phys Rev B Condens Matter Mater Phys*, vol. 55, no. 20, pp. 13605–13610, 1997, doi: 10.1103/PhysRevB.55.13605.
- [184] B. R. Hyun *et al.*, "Electron injection from colloidal PbS quantum dots into titanium dioxide nanoparticles," *ACS Nano*, vol. 2, no. 11, pp. 2206–2212, 2008, doi: 10.1021/nn800336b.
- [185] Z. Ren *et al.*, "Bilayer PbS Quantum Dots for High-Performance Photodetectors," *Advanced Materials*, vol. 29, no. 33, p. 1702055, Sep. 2017, doi: 10.1002/adma.201702055.
- [186] J. M. Luther, M. Law, Q. Song, C. L. Perkins, M. C. Beard, and A. J. Nozik, "Structural, optical, and electrical properties of self-assembled films of PbSe nanocrystals treated with 1,2-ethanedithiol," *ACS Nano*, vol. 2, no. 2, pp. 271–280, Feb. 2008, doi: 10.1021/nn7003348.
- [187] Z. Zhao *et al.*, "Ultraviolet Narrowband Photomultiplication Type Organic Photodetectors with Fabry–Pérot Resonator Architecture," *Adv Funct Mater*, vol. 32, no. 29, p. 2203606, Jul. 2022, doi: 10.1002/adfm.202203606.
- [188] K. Yang *et al.*, "Highly sensitive broadband photomultiplication type all-polymer photodetectors and their applications in optical pulse counting," *J Mater Chem C Mater*, vol. 10, no. 30, pp. 10888–10894, Aug. 2022, doi: 10.1039/d2tc02144g.

References

- [189] Z. Zhao *et al.*, “Highly stable photomultiplication-type organic photodetectors with single polymers containing intramolecular traps as the active layer,” *J Mater Chem C Mater*, vol. 10, no. 20, pp. 7822–7830, 2022, doi: 10.1039/d2tc01297a.
- [190] X. Zhao *et al.*, “Photomultiplication type organic photodetectors with different response characteristics under forward or reverse bias,” *Org Electron*, vol. 108, p. 106587, Sep. 2022, doi: 10.1016/j.orgel.2022.106587.
- [191] R. Saran and R. J. Curry, “Lead sulphide nanocrystal photodetector technologies,” *Nat Photonics*, vol. 10, no. 2, pp. 81–92, Feb. 2016, doi: 10.1038/nphoton.2015.280.
- [192] G. Konstantatos and E. H. Sargent, “Nanostructured materials for photon detection,” *Nat Nanotechnol*, vol. 5, no. 6, pp. 391–400, May 2010, doi: 10.1038/nnano.2010.78.
- [193] G. Konstantatos *et al.*, “Hybrid graphene-quantum dot phototransistors with ultrahigh gain,” *Nat Nanotechnol*, vol. 7, no. 6, pp. 363–368, 2012, doi: 10.1038/nnano.2012.60.
- [194] Y. Wei *et al.*, “Lateral Photodetectors Based on Double-Cable Polymer/Two-Dimensional Perovskite Heterojunction,” *ACS Appl Mater Interfaces*, vol. 12, no. 7, pp. 8826–8834, Feb. 2020, doi: 10.1021/acsami.9b19467.
- [195] T. Q. Trung *et al.*, “An Omnidirectionally Stretchable Photodetector Based on Organic-Inorganic Heterojunctions,” *ACS Appl Mater Interfaces*, vol. 9, no. 41, pp. 35958–35967, Oct. 2017, doi: 10.1021/acsami.7b09411.
- [196] M. Peng *et al.*, “Room-Temperature Direct Synthesis of PbSe Quantum Dot Inks for High-Detectivity Near-Infrared

- Photodetectors,” *ACS Appl Mater Interfaces*, vol. 13, no. 43, pp. 51198–51204, Nov. 2021, doi: 10.1021/acscami.1c13723.
- [197] P. Luo *et al.*, “PbSe Quantum Dots Sensitized High-Mobility Bi₂O₂Se Nanosheets for High-Performance and Broadband Photodetection beyond 2 μ m,” *ACS Nano*, vol. 13, no. 8, pp. 9028–9037, Aug. 2019, doi: 10.1021/acsnano.9b03124.
- [198] X. Liu, T. Starr, A. F. Starr, and W. J. Padilla, “Infrared spatial and frequency selective metamaterial with near-unity absorbance,” *Phys Rev Lett*, vol. 104, no. 20, May 2010, doi: 10.1103/PhysRevLett.104.207403.
- [199] A. Lochbaum, Y. Fedoryshyn, A. Dorodnyy, U. Koch, C. Hafner, and J. Leuthold, “On-Chip Narrowband Thermal Emitter for Mid-IR Optical Gas Sensing,” *ACS Photonics*, vol. 4, no. 6, pp. 1371–1380, Jun. 2017, doi: 10.1021/acsp Photonics.6b01025.
- [200] V. Adinolfi and E. H. Sargent, “Photovoltage field-effect transistors,” *Nature*, vol. 542, no. 7641, pp. 324–327, Feb. 2017, doi: 10.1038/nature21050.
- [201] W. Gong *et al.*, “Limiting Factors of Detectivity in Near-Infrared Colloidal Quantum Dot Photodetectors,” *ACS Appl Mater Interfaces*, vol. 14, no. 22, pp. 25812–25823, 2022, doi: 10.1021/acscami.2c06620.
- [202] D. Lachance-Quirion *et al.*, “Telegraphic noise in transport through colloidal quantum dots,” *Nano Lett*, vol. 14, no. 2, pp. 882–887, 2014, doi: 10.1021/nl404247e.
- [203] M. A. Hines and G. D. Scholes, “Colloidal PbS Nanocrystals with Size-Tunable Near-Infrared Emission: Observation of Post-Synthesis Self-Narrowing of the Particle Size

References

- Distribution,” *Advanced Materials*, vol. 15, no. 21, pp. 1844–1849, Nov. 2003, doi: 10.1002/adma.200305395.
- [204] J. N. Humphrey and R. L. Petritz, “Photoconductivity of lead selenide: Theory of the mechanism of sensitization,” *Physical Review*, vol. 105, no. 6, pp. 1736–1740, 1957, doi: 10.1103/PhysRev.105.1736.
- [205] J. J. Choi *et al.*, “PbSe Nanocrystal Excitonic Solar Cells,” *Nano Lett*, vol. 9, no. 11, pp. 3749–3755, Dec. 2009, doi: 10.1021/nl901930g.
- [206] J. Jasieniak, M. Califano, and S. E. Watkins, “Size-dependent valence and conduction band-edge energies of semiconductor nanocrystals,” *ACS Nano*, vol. 5, no. 7, pp. 5888–5902, Jul. 2011, doi: 10.1021/nn201681s.
- [207] E. M. Miller *et al.*, “Revisiting the Valence and Conduction Band Size Dependence of PbS Quantum Dot Thin Films,” *ACS Nano*, vol. 10, no. 3, pp. 3302–3311, Mar. 2016, doi: 10.1021/acsnano.5b06833.
- [208] M. M. Ackerman, M. Chen, and P. Guyot-Sionnest, “HgTe colloidal quantum dot photodiodes for extended short-wave infrared detection,” *Appl Phys Lett*, vol. 116, no. 8, p. 83502, Feb. 2020, doi: 10.1063/1.5143252.
- [209] E. Lhuillier *et al.*, “Infrared Photodetection Based on Colloidal Quantum-Dot Films with High Mobility and Optical Absorption up to THz,” *Nano Lett*, vol. 16, no. 2, pp. 1282–1286, Feb. 2016, doi: 10.1021/ACS.NANOLETT.5B04616/SUPPL_FILE/NL5B04616_SI_001.PDF.
- [210] M. Chen, G. Shen, and P. Guyot-Sionnest, “Size Distribution Effects on Mobility and Intraband Gap of HgSe Quantum

- Dots,” *Journal of Physical Chemistry C*, vol. 124, no. 29, pp. 16216–16221, 2020, doi: 10.1021/acs.jpcc.0c05268.
- [211] C. Livache *et al.*, “A colloidal quantum dot infrared photodetector and its use for intraband detection,” *Nat Commun*, vol. 10, no. 1, Dec. 2019, doi: 10.1038/s41467-019-10170-8.
- [212] S. Bin Hafiz, M. M. Al Mahfuz, S. Lee, and D. K. Ko, “Midwavelength Infrared p-n Heterojunction Diodes Based on Intraband Colloidal Quantum Dots,” *ACS Appl Mater Interfaces*, vol. 13, no. 41, pp. 49043–49049, Oct. 2021, doi: 10.1021/acsami.1c14749.
- [213] S. Bin Hafiz, M. M. Al Mahfuz, and D. K. Ko, “Vertically Stacked Intraband Quantum Dot Devices for Mid-Wavelength Infrared Photodetection,” *ACS Appl Mater Interfaces*, vol. 13, no. 1, pp. 937–943, Jan. 2021, doi: 10.1021/acsami.0c19450.
- [214] J. Wei *et al.*, “Zero-bias mid-infrared graphene photodetectors with bulk photoresponse and calibration-free polarization detection,” *Nat Commun*, vol. 11, no. 1, 2020, doi: 10.1038/s41467-020-20115-1.
- [215] S. Castilla *et al.*, “Plasmonic antenna coupling to hyperbolic phonon-polaritons for sensitive and fast mid-infrared photodetection with graphene,” *Nat Commun*, vol. 11, no. 1, 2020, doi: 10.1038/s41467-020-18544-z.
- [216] S. Cakmakyapan, P. K. Lu, A. Navabi, and M. Jarrahi, “Gold-patched graphene nano-stripes for high-responsivity and ultrafast photodetection from the visible to infrared regime,” *Light Sci Appl*, vol. 7, no. 1, pp. 2047–7538, 2018, doi: 10.1038/s41377-018-0020-2.

References

- [217] S. Lukman *et al.*, “High oscillator strength interlayer excitons in two-dimensional heterostructures for mid-infrared photodetection,” *Nat Nanotechnol*, vol. 15, no. 8, pp. 675–682, Jun. 2020, doi: 10.1038/s41565-020-0717-2.
- [218] X. Chen *et al.*, “Widely tunable black phosphorus mid-infrared photodetector,” *Nat Commun*, vol. 8, no. 1, 2017, doi: 10.1038/s41467-017-01978-3.
- [219] Q. Guo *et al.*, “Black phosphorus mid-infrared photodetectors with high gain,” *Nano Lett*, vol. 16, no. 7, pp. 4648–4655, 2016, doi: 10.1021/acs.nanolett.6b01977.
- [220] H. Kim *et al.*, “Actively variable-spectrum optoelectronics with black phosphorus,” *Nature*, vol. 596, no. 7871, pp. 232–237, 2021, doi: 10.1038/s41586-021-03701-1.
- [221] J. Miao *et al.*, “Single Pixel Black Phosphorus Photodetector for Near-Infrared Imaging.,” *Small*, vol. 14, no. 2, Jan. 2018, doi: 10.1002/sml.201702082.
- [222] J. Haas and B. Mizaikoff, “Advances in Mid-Infrared Spectroscopy for Chemical Analysis,” *Annual Review of Analytical Chemistry*, vol. 9, no. 1, pp. 45–68, Jun. 2016, doi: 10.1146/annurev-anchem-071015-041507.
- [223] C. Ho, A. Robinson, D. Miller, and M. Davis, “Overview of Sensors and Needs for Environmental Monitoring,” *Sensors*, vol. 5, no. 1, pp. 4–37, Feb. 2005, doi: 10.3390/s5010004.
- [224] B. W. Jia, K. H. Tan, W. K. Loke, S. Wicaksono, K. H. Lee, and S. F. Yoon, “Monolithic Integration of InSb Photodetector on Silicon for Mid-Infrared Silicon Photonics,” *ACS Photonics*, vol. 5, no. 4, pp. 1512–1520, Apr. 2018, doi: 10.1021/acsp Photonics.7b01546.

- [225] A. Rogalski and P. Martyniuk, "InAs/GaInSb superlattices as a promising material system for third generation infrared detectors," *Infrared Phys Technol*, vol. 48, no. 1, pp. 39–52, Apr. 2006, doi: 10.1016/J.INFRARED.2005.01.003.
- [226] H. Schneider and H. C. Liu, *Quantum Well Infrared Photodetectors*, vol. 126. in Springer Series in OPTICAL SCIENCES, vol. 126. Springer Berlin Heidelberg, 2006. doi: 10.1007/978-3-540-36324-8.
- [227] Y. Ma, Y. Zhang, and W. W. Yu, "Near infrared emitting quantum dots: synthesis, luminescence properties and applications," *J Mater Chem C Mater*, vol. 7, no. 44, pp. 13662–13679, 2019, doi: 10.1039/C9TC04065J.
- [228] N. Goubet *et al.*, "Terahertz HgTe Nanocrystals: Beyond Confinement," *J Am Chem Soc*, vol. 140, no. 15, pp. 5033–5036, Apr. 2018, doi: 10.1021/JACS.8B02039/SUPPL_FILE/JA8B02039_SI_001.PDF.
- [229] E. H. Sargent, "Solar Cells, Photodetectors, and Optical Sources from Infrared Colloidal Quantum Dots," *Advanced Materials*, vol. 20, no. 20, pp. 3958–3964, Oct. 2008, doi: 10.1002/adma.200801153.
- [230] S. Zhang, Y. Hu, and Q. Hao, "Advances of Sensitive Infrared Detectors with HgTe Colloidal Quantum Dots," *Coatings*, vol. 10, no. 8, p. 760, Aug. 2020, doi: 10.3390/coatings10080760.
- [231] Y. Lai, H. Li, D. K. Kim, B. T. Diroll, C. B. Murray, and C. R. Kagan, "Low-frequency (1/ f) noise in nanocrystal field-effect transistors," *ACS Nano*, vol. 8, no. 9, pp. 9664–9672, Sep. 2014, doi: 10.1021/nn504303b.
- [232] F. Prins *et al.*, "Fast and efficient photodetection in nanoscale quantum-dot junctions," *Nano Lett*, vol. 12, no.

References

- 11, pp. 5740–5743, Nov. 2012, doi: 10.1021/NL303008Y/SUPPL_FILE/NL303008Y_SI_001.PDF.
- [233] H. Wang *et al.*, “Transport in a Single Self-Doped Nanocrystal,” *ACS Nano*, vol. 11, no. 2, pp. 1222–1229, Feb. 2017, doi: 10.1021/ACSNANO.6B07898/ASSET/IMAGES/LARGE/NN-2016-078986_0004.JPEG.
- [234] F. N. Hooge, “The relation between $1/f$ noise and number of electrons,” *Physica B Condens Matter*, vol. 162, no. 3, pp. 344–352, Jul. 1990, doi: 10.1016/0921-4526(90)90030-X.
- [235] W. Li *et al.*, “Refractory plasmonics with titanium nitride: Broadband,” *Advanced Materials*, vol. 26, no. 47, pp. 7959–7965, Dec. 2014, doi: 10.1002/adma.201401874.
- [236] W. Li, Z. J. Coppens, L. V. Besteiro, W. Wang, A. O. Govorov, and J. Valentine, “Circularly polarized light detection with hot electrons in chiral plasmonic metamaterials,” *Nat Commun*, vol. 6, no. 1, p. 8379, Sep. 2015, doi: 10.1038/ncomms9379.
- [237] P. Yu *et al.*, “Broadband Metamaterial Absorbers,” *Adv Opt Mater*, vol. 7, no. 3, Feb. 2019, doi: 10.1002/adom.201800995.
- [238] M. Chen, Y. Wang, and Z. Zhao, “Monolithic Metamaterial-Integrated Graphene Terahertz Photodetector with Wavelength and Polarization Selectivity.,” *ACS Nano*, vol. 16, no. 10, pp. 17263–17273, Oct. 2022, doi: 10.1021/acsnano.2c07968.
- [239] A. De Iacovo, C. Venettacci, L. Colace, L. Scopa, and S. Foglia, “Noise performance of PbS colloidal quantum dot photodetectors,” *Appl Phys Lett*, vol. 111, no. 21, p. 211104, Nov. 2017, doi: 10.1063/1.5005805.

- [240] A. van der Ziel, "Noise in solid-state devices and lasers," *Proceedings of the IEEE*, vol. 58, no. 8, pp. 1178–1206, 1970, doi: 10.1109/PROC.1970.7896.
- [241] B. M. Wilamowski and J. D. Irwin, Eds., *Fundamentals of Industrial Electronics*. CRC Press, 2018. doi: 10.1201/9781315218441.
- [242] X. Xue *et al.*, "Low Dark-Current Quantum-Dot Infrared Imager," *ACS Photonics*, Nov. 2023, doi: 10.1021/ACSPHOTONICS.3C01070.
- [243] P. Rastogi *et al.*, "Complex Optical Index of HgTe Nanocrystal Infrared Thin Films and Its Use for Short Wave Infrared Photodiode Design," *Adv Opt Mater*, vol. 9, no. 10, p. 2002066, May 2021, doi: 10.1002/adom.202002066.
- [244] R. Schwanninger *et al.*, "Highly Responsive Mid-Infrared Metamaterial Enhanced Heterostructure Photodetector Formed out of Sintered PbSe/PbS Colloidal Quantum Dots," *ACS Appl Mater Interfaces*, vol. 15, no. 8, pp. 10847–10857, Mar. 2023, doi: 10.1021/ACSAMI.2C23050/ASSET/IMAGES/LARGE/AM2C23050_0006.JPEG.

List of Acronyms

0D	0-Dimensional
1D	1-Dimensional
2D	2-Dimensional
3D	3-Dimensional
AFM	Atomic force microscopy
Ag ₂ S	Silver sulfide
Ag ₂ Se	Silver selenide
Al ₂ O ₃	Alumina
Au	Gold
BLIP	Background-limited infrared photodetection
BP	Black phosphorous
BZ	Brillouin zone
CBD	Chemical bath deposition
CVD	Chemical vapor deposition
cQD	Colloidal Quantum Dot
DFT	Density function theory
DMF	Dimethylformamide
EM	Electro magnetic
EDT	Ethanedithiol
EDX	Energy dispersive X-ray
EQE	External quantum efficiency
GaAs	Gallium arsenide
Ge	Germanium
GIXRD	Grazing incident X-ray diffraction
nBN	Hexagonal boron nitride
Hg _{1-x} Cd _x Te	Mercury cadmium telluride

List of Acronyms

HEB	Hot electron Bolometer
HfS ₂	Hafnium disulfide
HOMO	Highest occupied molecular orbital
HgCl ₂	Mercury dichloride
HgSe	Mercury Selenide
HgTe	Mercury telluride
InSb	Indium antimonide
InP	Indium phosphide
LOMO	Lowest unoccupied molecular orbital
LWIR	Long wave infrared
MBE	Molecular beam epitaxy
MIR	Mid infrared
MM	Metamaterial
MoS ₂	Molybdenum disulfide
MQW	Multi quantum well
MQWIP	Multi quantum well infrared photodetection/ photodetector
NIR	Near infrared
O-E	Opto- electric
PbO	Lead oxide
PbS	Lead sulfide
PbSe	Lead selenide
PC	Photoconductor
PEM	Photoelectromagnetic detector
PMMA	Polymethylmethacrylat
PV	Photovoltaic
QD	Quantum Dot
QWIP	Quantum well infrared photodetection/ photodetector

RMS	Root mean square
SBD	Schottky barrier detector
SEM	Scanning electron microscopy
Si	Silicon
SiO ₂	Silicon dioxide
SRH	Shockley-Read-Hall
SWIR	Short wave infrared
TEM	Transmission electron microscopy
TEM	Transversal electro magnetic
Ti ₂ O ₃	Dititanium trioxide
TMD	Transition metal dichalcogenides
VIS	Visible
W	Tungsten
WS ₂	Tungsten disulfide
XRD	X-ray diffraction

List of Symbols

The symbols used in this thesis together are listed here with a brief explanation grouped as Latin symbols, Greek symbols and other symbols.

Latin Symbols

A	Active area, absorption
A^*	Richardson constant
B	Auger coefficient
c	Speed of light
c_0	Vacuum speed of light
$c_{c,trap}$	Capture coefficient for electrons from conduction band to a trap state
$c_{c,v}$	Capture coefficient for carriers from conduction band to valence band
$c_{trap,v}$	Capture coefficient for electrons from a trap state to the valence band
d	Sample thickness
d_0	Degeneracy of unfilled trap state
d_1	Degeneracy of filled trap state
D^*	Specific detectivity
e	Euler number
$e_{trap,c}$	Emission of carrier from trap to conduction band
$e_{v,trap}$	Emission of carrier from valence band to trap
E	Electric field
E_0	Electric field amplitude
E_c	Conduction band energy
E_F	Fermi level energy
E_G	Energy band gap
E_v	Valence band energy

List of Symbols

EQE	External quantum efficiency
E_t	Trap state energy
E_x	Electric field in x direction
E_{ph}	Photon energy
f	Frequency
f_0	Center frequency/ Frequency of interest
Δf	Bandwidth, width around frequency of interest
g_n	Illumination induced electron generation rate
g_p	Illumination induced hole generation rate
g_{ph}	Illumination induced carrier generation rate
h	Planck constant
H_0	Magnetic field amplitude
H_y	Magnetic field in y direction
i	Complex constant
i_n	Noise current
I_{ph}	Illumination intensity
I	Current
I_0	Illumination intensity at surface
I_{dark}	Electric current in dark
I_{light}	Electric current under illumination
I_{ph}	Photocurrent
J	Current density
J_{scl}	Injection limited current density
\mathbf{k}	Wave vector
k	Wave number
k_0	Vacuum wave number
k_B	<i>Boltzmann constant</i>
l_{ch}	Channel length

m_0	Electron mass
m_n	Effective electron mass
m_p	Effective hole mass
$M_{\mu\nu}$	Momentum matrix concerning bands μ and ν
n	Electron density
\mathbf{n}	Refractive index
\tilde{n}	Complex refractive index
Δn	Illumination induced electron density change
n_d	Hole density under in dark
n_i	Refractive index medium with incoming EM- wave
n_i	Intrinsic carrier concentration
n_{max}	Maximum electron concentration under illumination
n_n	Density of occupied defect states
n_{ph}	Electron density under illumination
n_r	Refractive index medium with transmitted EM- wave
N	Total number of carriers
N_t	Trap state density
p	Hole density
Δp	Illumination induced hole density change
P_{in}	Incident Power
p_d	Electron density under in dark
p_{ph}	Hole density under illumination
q	Elementary charge
Q	Total accumulated charge
R	Reflectance
\mathbf{R}	Responsivity
R_c	Total captured rate
R_{\perp}	Reflectance normal to plane

List of Symbols

R_{\parallel}	Reflectance in-plane
R_{noise}	Resistance of a system with noise
r	Radius
r_0	Eigenstate radius
r_A	Auger recombination rate
r_{ex}	Exciton radius
r_n	Electron recombination rate
r_p	Hole recombination rate
S_I	Noise current spectral density
$S_{I,G-R}$	Generation recombination noise current spectral density
$S_{I,shot}$	Shot noise current spectral density
S_{nonrad}	Carrier capture cross-section
S_v	Noise voltage spectral density
$S_{v,shot}$	Shot noise voltage spectral density
$S_{v,thermal}$	Thermal noise voltage spectral density
S_z	Poynting vector in z direction
t	Time
T	Temperature, transmission
t_0	Point in time, start of illumination
t_1	Point in time, stop of illumination
t_{trap}	Trap lifetime
$t_{tr,n}$	Electron transition time
$t_{tr,p}$	Hole transition time
V	Volume or potential energy
v_{rms}	RMS carrier velocity
V_{lim}	Injection limited voltage
$v_{thermal}$	Thermal carrier velocity
w_{ch}	Channel width w_{ch}

x	Point along x- direction, x- direction
y	Point along y- direction, y- direction
z	Point along z- direction, z- direction
Z_0	Free space impedance
Z_{MM}	Metamaterial impedance

Greek Symbols

α	Absorption coefficient
α_H	Hooge's constant
$\beta_{n,l}$	n^{th} zero of the Bessel function
ϵ'	Real part of relative permittivity
ϵ''	Imaginary part of relative permittivity
ϵ_0	Free space permittivity
ϵ_r	Relative permittivity
η	Quantum efficiency
θ	Azimuth angle
λ	Wavelength
μ'_r	Real part relative permeability
μ''_r	Imaginary part relative permeability
μ_0	Vacuum permeability
μ_n	Electron mobility
μ_p	Hole mobility
μ_r	Relative permeability
Γ	Gain
σ_d	Conductivity
$\Delta\sigma_{ph}$	Illumination induced conductivity change
σ_{ph}	Conductivity under illumination
τ_0	Time constant carrier density rise due to illumination

List of Symbols

τ_1	Time constant carrier density decrease stopping illumination
τ_A	Electron lifetime due to Auger recombination quantum mechanical framework
$\tau_{A,n}$	Electron lifetime due to Auger recombination
τ_n	Electron lifetime
τ_p	Hole lifetime
τ_{n0}	Electron lifetime in a SRH recombination process
τ_{p0}	Hole lifetime in a SRH recombination process
τ_r	Carrier lifetime
τ_{tot}	Total carrier lifetime several due to several recombination mechanism
ϕ	Elevation angle
$\Phi_{B,n}$	Electron Schottky barrier height
$\Phi_{B,p}$	Hole Schottky barrier height
ϕ_{in}	Incoming photon flux
ϕ_i	Angle of incoming EM- wave
ϕ_m	Metal work function
ϕ_r	Angle of reflected EM- wave
ϕ_t	Angle of transmitted EM- wave
Ψ	Carrier wave function
χ_s	Electron affinity
ω	Angular frequency

Other symbols

\hbar	Planck constant dived by 2π
k	Extinction coefficient

List of Supervised Theses

This chapter lists the group, semester and master theses supervised during the PhD studies. The order is by submission date starting with the most recent works.

Semester Theses

Thomas Dubach, “GeTe Nanoparticles for Optical Switches and Metamaterials” *Semester Thesis*, August 2021.

Lodovico Rossi, “Nonlinear Material for Electro-Optic Modulators,” *Semester Thesis*, December 2020.

Bachelor Thesis

Dongkyu Lee, “Plasmonic Slot Meta-Surface for Photodetection Applications,” *Bachelor Thesis*, October 2021.



List of Publications

This chapter lists the first author and co-author publications reported during the doctoral studies. The order in each category is by publication date starting with the most recent contributions.

Journal Papers

- [J 1] **Raphael Schwanninger**, Shadi Nashashibi, Olesya Yarema, Stefan M. Koepfli, Yuriy Fedoryshyn, Vanessa Wood, Juerg Leuthold, “Metamaterial Engineering for Superior HgTe cQD Photodetector Performance”, *Advanced Optical Materials*, vol. 15, no. 8, pp. 10847–10857, 2024
- [J 2] **Raphael Schwanninger**, Stefan M. Koepfli, Olesya Yarema, Alexander Dorodnyy, Maksym Yarema, Annina Moser, Shadi Nashashibi, Yuriy Fedoryshyn, Vanessa Wood, Juerg Leuthold, “Highly Responsive Mid-Infrared Metamaterial Enhanced Heterostructure Photodetector Formed out of Sintered PbSe/PbS Colloidal Quantum Dots”, *ACS Applied Materials and Interfaces*, vol. 15, no. 8, pp. 10847–10857, 2023
- [J 3] Shadi Nashashibi, Stefan M. Koepfli, **Raphael Schwanninger**, Michael Baumann, Michael Doderer, Dominik Bisang, Yuriy Fedoryshyn, and Juerg Leuthold, “Engineering Graphene Phototransistors for High Dynamic Range Applications”, *ACS Nano*, vol. 18, no. 20, pp. 12760–12770, 2024
- [J 4] Joel Winiger, Killian Keller, Patrik Gjini, David Moor, Michael Baumann, Daniel Chelladurai, Manuel Kohli, **Raphael Schwanninger**, Yuriy Fedoryshyn, Costanzo Tommaso, Ueli Koch, Gabriel Caruntu, and Juerg Leuthold, “Measuring dielectric and electro-optic responses of thin films using plasmonic devices”, *Optics Express*, vol. 32, no. 3, pp. 4511–4524, 2024

List of Symbols

- [J 5] Stefan M. Koepfli, Michael Baumann, Yesim Koyaz, Robin Gadola, Arif Güngör, Killian Keller, Yannik Horst, Shadi Nashashibi, **Raphael Schwanninger**, Michael Doderer, Elias Passerini, Yuriy Fedoryshyn, Juerg Leuthold, "Metamaterial Graphene Photodetector with Bandwidth Exceeding 500 GHz," *Science*, vol. 380, no. 6650, pp. 1169-1174, 2023.
- [J 6] Nikola Đorđević, **Raphael Schwanninger**, Maksym Yarema, Stefan M. Koepfli, Olesya Yarema, Yannick Salamin, Nolan Lassaline, Bojun Cheng, Nuri Yazdani, Alexander Dorodnyy, Yuriy Myronovych Fedoryshyn, Vanessa Wood, Juerg Leuthold, "Metasurface Colloidal Quantum Dot Photodetectors," *ACS Photonics*, vol. 9, 2, pp. 482-492, 2022.

Conference Contributions

- [C 1] Shadi Nashashibi, Stefan M. Koepfli, **Raphael Schwanninger**, Josua Graf, Qadood Haq, Yuriy Fedoryshyn, Eberhart Zrenner, and Juerg Leuthold, "Graphene Photogating Devices for Retinal Implants," In *CLEO: Applications and Technology* (pp. ATu4B-5). Optica Publishing Group.

Curriculum Vitae



Raphael Sebastian Schwanninger

Date of birth: 13.01.1991

Nationality: Austria

Work Experience

2019 – 2024 **Institute of Electromagnetic Fields, ETH Zurich, Zürich Switzerland**

Research Associate in Photodetector Technology

- Research on colloidal quantum dot-based photodetectors and plasmonic metasurfaces

2017 – 2018 **Institute for Electronics, ETH Zurich, Zürich, Switzerland**

Research Assistant

- Research on eutectic gallium-indium alloys combined with copper laminates for stretchable electronics applications.

Education

2016 – 2019 **Master of Science, ETH Zurich**

Specializations: Electrical Engineering and Information Technology

Thesis: “Metamaterials and Colloidal Quantum Dots Photodetector”

2011 – 2016 **Bachelor of Science, TU Wien**

Specializations: Electrical Engineering and Information Technology

Thesis: “Current Distribution in Gallium Nitride High Power Light Emitting Diodes”

List of Symbols

Teaching

2019 – 2020	Lecturer, “Python for Engineers”, <i>ETH Zurich</i>
2020 – 2021	Lecturer, “Comsol Design Tool”, <i>ETH Zurich</i>
2021 – 2023	Lecturer, “Optics and Spectroscopy Lab”, <i>ETH Zurich</i>
2023 – 2024	Lecturer, “Comsol Design Tool”, <i>ETH Zurich</i>

ETH Zürich Series in Electromagnetic Fields, Vol. 33
Edited by Prof. J. Leuthold

ETH Zürich
Institute of Electromagnetic Fields (IEF)
Switzerland

The mid-wave infrared spectral range is critical for various technologies and scientific research. Many applications operating in this range rely on highly sensitive photodetectors. This leads to an increased demand for low-cost and high-performing detectors. However, achieving both high performance and cost-effectiveness remains a significant challenge. This doctoral thesis investigates the potential of low-cost absorber materials and innovative performance enhancement schemes to address these challenges.

The low-cost absorber materials used throughout this thesis are colloidal quantum dots. While these materials offer the potential to reduce costs, they often exhibit limited performance. To address low responsivities, a gain enhancing heterostructure combining sintered lead selenide and lead sulfide colloidal quantum dots was combined with a resonant metamaterial. This combination resulted in a up to 20-fold increase of the responsivity. Furthermore, a metamaterial optimization process was applied to a mercury telluride colloidal quantum dot-based photodetector. This optimization process led to a significant increase in responsivity, while simultaneously reducing noise, resulting in a 345-fold improvement in detectivity.

This dissertation presents a pathway for significantly improving both the performance and cost-effectiveness of mid-wave infrared photodetectors through the co-integration of colloidal quantum dots and optimized metamaterial designs.

About the Author

Raphael Schwanninger was born in Austria, in 1991. He received his B.Sc. degree (2016) from the Vienna University of Technology (TU Wien), Vienna, Austria. His M.Sc. degree in electrical engineering and information technology (2019) was received from the ETH Zurich, Zurich, Switzerland. He joined the research group of Prof. Juerg Leuthold in 2019 and received a Dr. sc. degree from the ETH Zurich in 2024. His research interests include photonics, plasmonics, colloidal quantum dots and optoelectronic devices.

ISBN: 978-3-907363-75-1

